Distribution Agreement

In presenting this thesis or dissertation as a partial fulfillment of the requirements for an advanced degree from Emory University, I hereby grant to Emory University and its agents the non-exclusive license to archive, make accessible, and display my thesis or dissertation in whole or in part in all forms of media, now or hereafter known, including display on the world wide web. I understand that I may select some access restrictions as part of the online submission of this thesis or dissertation. I retain all ownership rights to the copyright of the thesis or dissertation. I also retain the right to use in future works (such as articles or books) all or part of this thesis or dissertation.

Signature:

_____ _____

Chentao Li Date

Manipulating Optical Nonlinearities in Nanophotonic Systems via Plasmons and High-index Resonators

By

Chentao Li
Doctor of Philosophy

Physics

Hayk Harutyunyan, Ph.D.
Advisor

Sergei Urazhdin, Ph.D.
Committee Member

Ajit Srivastava, Ph.D.
Committee Member

Justin Burton, Ph.D.
Committee Member

Wenshan Cai, Ph.D.
Committee Member

Accepted:

Kimberly Jacob Arriola, Ph.D.
Dean of the James T. Laney School of Graduate Studies

Date

Manipulating Optical Nonlinearities in Nanophotonic Systems via Plasmons and High-index Resonators

By

Chentao Li
B.S., Nanjing University, China, 2016

Advisor: Hayk Harutyunyan, Ph.D.

An abstract of
A dissertation submitted to the Faculty of the
James T. Laney School of Graduate Studies of Emory University
in partial fulfillment of the requirements for the degree of
Doctor of Philosophy
in Physics
2022

Abstract

Manipulating Optical Nonlinearities in Nanophotonic Systems via Plasmons and High-index Resonators
By Chentao Li

Nanophotonic platforms allow light concentration and confinement at the subwavelength scales. This property is especially beneficial for the enhancement of nonlinear optical processes that are typically very weak in the bulk materials. Within this broad framework of nonlinear nanophotonics my research focuses on two main thrusts. The first research focus of my dissertation uses plasmonic nanostructures to manipulate and enhance the nonlinear optical effects in hybrid low-dimensional nanoscale systems. Introducing plasmonic nanostructures strongly confines the local electric field distribution and thus remarkably enhances the interaction strength between photons and adjacent materials. The nonlinear optical properties of these systems can be dramatically modified on a nanoscale benefiting from this subwavelength confinement of electromagnetic energy. The second thrust of my research focuses on using high-index dielectric resonators to enhance the light- matter interaction at the nanoscale. Lower optical loss and CMOS-compatibility make these dielectric resonators attractive new platforms for nanophotonics and nonlinear optics. The reported efficiency of nonlinear processes is orders of magnitude larger compared with plasmonic resonances.

In Chapter 1, an introduction of the background in nano-optics, nonlinear optics and ultrafast optics is given for reference.

In Chapter 2, the second harmonic generation (SHG) in the plasmon-WSe_2 strong-coupling system is discussed. We report the first experimental observation of Rabi splitting in the pump frequency dependence of the second-harmonic signal in such systems and this splitting phenomenon can be explained by a coupled-oscillator model with second-order nonlinearities. Rigorous numerical simulations utilizing a nonperturbative nonlinear hydrodynamic model of conduction electrons support this interpretation and reproduce experimental results. This is a typical example to use plasmonic nanostructures in manipulating nonlinear optical effects in strong light-matter interaction systems.

In Chapter 3, an invertible nonlinearity of ITO thin films is investigated. ITO thin films are unique high-index materials which possess resonance modes in the epsilon-near-zero (ENZ) region and recently emerge as new platforms for enhancing the optical nonlinearity. We report a systematic theoretical and experimental study of the origin of ITO thin film nonlinearities contributed by the intraband transition in a non-parabolic conduction band and the interband transition via near infrared (NIR) and ultra-violet (UV) excitations. A new mechanism is found that the non-parobolicity of the band structure, which brings a larger effective mass in the intraband transition, and the Fermi energy, which determines the free carrier density, are two competing forces that jointly contribute to an invertible nonlinearity of ITOs in the NIR region. This corresponds to the second thrust of my dissertation, in which high-index resonators are implemented in enhancing nonlinear optical effects.

Manipulating Optical Nonlinearities in Nanophotonic Systems via Plasmons and High-index Resonators

By

Chentao Li
B.S., Nanjing University, China, 2016

Advisor: Hayk Harutyunyan, Ph.D.

A dissertation submitted to the Faculty of the
James T. Laney School of Graduate Studies of Emory University
in partial fulfillment of the requirements for the degree of
Doctor of Philosophy
in Physics
2022

Acknowledgments

I would like to express my appreciation to all the people who help me with my PhD career. Without you, it is impossible for me to get to this point.

First of all, I want to thank my advisor Prof. Hayk Harutyunyan who helped me all the time through my whole PhD study. We've been working together for more than five years and it is you who led me into the field of nanophotonics, trained me from an innocent green-hand to a real experimentalist and a young physicist. You've always been professional, intelligent, creative, patient and responsible. I've learned so much from you, not only in physics but also the enthusiasm of active thinking, rigorous studying and continuous hardworking. I believe that all my accomplishment and success in my research study and future career would be just vanity without the efforts and support you provided.

Next, I would also like to extend my gratitude to all my committee members, collaborators, colleague and friends. Prof. Sergei Urazhdin, Prof. Ajit Srivastava, Prof. Justin Burton and Prof. Wenshan Cai, your advice and support makes me always on the right path of pursuing the PhD degree. Your great experience and kindness is of significant importance in helping me understand the general physics principle that is not specific to my study field. Dr. Robert Lemasters, Dr. Ryan Freeman, Dr. Feng Wang and Dr. Manoj Manjare, you spent so much time teaching me on using those complicated equipment in the lab. Thank you for being so generous and selfless. Prof. Xin Lu, Prof. Maxim Sukharev and Prof. Matthew Pelton, thank you for contributing so much to our collaboration project. It was my first publication in my life and you cannot imagine how delightful I felt when the paper got accepted. I could never make it alone without your great effort. Xiaotong, Guanxiong, Muliang and so many friends in Emory and Georgia Tech, it was really nice to meet you all. Each discussion between us is a baptism on my brain. I can feel your unparalleled passion for life and science, which inspires me to face any difficulty with courage and

confidence.

Finally, I want to give my deepest thanks to my family. My mom, although you are far away in China and we haven't seen each other for almost three years, you always stand behind me and give me your silent but warmest support, as what you've been doing for the past twenty-eight years, from my birth to childhood to where I am right now, a PhD of Physics you are always proud of. "You raise me up, so I can stand on mountains." I couldn't get anywhere without the love, care and nurturing from you. Wenting, my wife and my most valuable treasure I got during my PhD career, you are the moonlight that shines on my gloomy and boring life. I feel like I'm the luckiest person in the whole world for meeting you, marrying you, having your love and constant support. Thank you for all the late nights and early mornings, and for keeping me sane with your wisdom and insight. Thank you for being my nurse, my proofreader and my sounding board of soul. We've overcome so much obstacles and enjoyed so much fun. We will continue our life story together for the rest thousands of years.

Contents

List of Figures

List of Tables

Chapter 1

Introduction

1.1 Nano-optics

In the history of science, understanding of optics ushered a new era for invigilating the nature. Optical instruments, such as microscopes and telescopes, enable the observation of fascinating phenomena that are not directly detectable by human eyes. As we move to smaller scales with the deeper investigation of natural things and a higher demand of integration of man-made materials, such as electronic circuits, however, the traditional optical methodology becomes more limited. New physics needs to be exploited for the future technological applications. More specifically, the increasing trend towards nano-science and nano-technology makes it a necessity to study optics and light-matter interaction on nanoscale, which forms the basis of nano-optics.

Nano-optics studies optical phenomena on nanoscale and optical properties of nanostructures. One central goal of nano-optics is to extend the use of optical techniques to length scales beyond the diffraction limit. Far-field microscopy is not suitable for nanoscale imaging due to this resolution limitation ($> 200nm$). Therefore, a local probe for optical near-fields is necessary to develop some new approaches, for ex-

ample, the photon scanning probing microscopy[1], nonlinear optical microscopy[2, 3] and metal-tip based enhanced field microscopy[4]. Another important aspect of nano-optics emerges with the modern technology of fabricating nanostructures, such as nanoparticles for sensor devices[5], single molecules for biophysical fluorescence and integrated photonic circuits in optical networks. All of these nanophotonic structures[6] are created to provide unique light-matter interaction properties and nano-optics aims to establish a basic understanding of them.[7]

1.1.1 Optical Near-fields

In far-field optics, after a light wave passes through a sub-wavelength-sized aperture on a plate, it is converted into a diverging spherical wave. Such divergence is called diffraction, an intrinsic characteristic of waves. Diffraction puts a limit on the range of wavevectors that can reach the far field during the propagation of the wave, and any wavevector laying outside this range turns into the optical near field. As the consequence of this loss of optical momentum in the far field, any image produced by the aperture is always a blur, which is the diffraction pattern. For example, a circular aperture has a divergence angle of λ/a, where λ and a are the wavelength of the incident light and the aperture radius, respectively. The spot size of the blurred image in the far-field, namely the central bright region of the diffraction pattern, is the Airy disk:

$$\varnothing_{Airy} = 1.22 * \frac{\lambda}{NA} \tag{1.1}$$

where $\varnothing_{Airy}$ is the diameter of the Airy disk, NA is the numerical aperture. Airy disk defines the smallest point to which a beam of light can be focused. As focused Airy patterns from different object details approach one another, they begin to overlap. When the overlapping patterns create enough constructive interference to reduce contrast, they eventually become indistinguishable from each other. This also holds

true for imaging under an optical microscope, and the smallest size resolvable with an optical microscope is called the diffraction limit. It can be inferred from Eq. 1.1 that this resolution depends on the wavelength of the incident light. Consequently, it is impossible to image subwavelength features with conventional far-field microscopes.

The use of optical near fields has been proposed to transcend the diffraction limit. As optical near fields retain all the information of wavevectors irradiating the aperture, the diffraction is no longer a limitation on the resolution of the imaging system. The spatial resolution of the optical near-field light depends on the size of the aperture instead of the wavelength. Therefore, given the size of the aperture much smaller than the wavelength, the resolution of the optical near-field image can be significantly increased from the far-field images. These optical near fields have been applied to realize diffraction-free, high-resolution optical microscopy, such as the photon scanning probing microscopy, nonlinear optical microscopy and metal-tip based enhanced field microscopy. It should be noted that evanescent waves, which describe the imaginary component of the wave vector k, also occur in the subwavelength dimension due to a rapid exponential decay instead of propagating. However, the generation of evanescent waves highly depends on the spatial distribution of the incident light, thus evanescent waves are still categorized into diffraction limited waves.[8]

Uncertainty principle can be used to understand the property of optical near fields:

$$\Delta k \Delta x \geq 1 \tag{1.2}$$

where Δk is the uncertainty of the wave vector and Δx is the uncertainty of the position. For near-fields of nanoscale apertures or particles, the spatial position can be accurately defined, indicating a wide distribution of the wave vector. Thus, the optical near field is free of diffraction, and as a result, optical science and technology beyond the diffraction limit can be realized by using optical near fields.

Classical electromagnetic theory, like Maxwell's equations can explain the mechanisms of optical near-fields generation. Analytical methods such as Green's function, multipole expansion, and numerical calculations such as the finite-difference time domain (FDTD) method and the finite element methods (FEM), have been developed to describe the distribution of optical near-fields based on the electromagnetic theory.

1.1.2 Nanoscale Confinement of Matter

Optical near-fields are generated based on nanoscale matter platforms, such as quantum dots (QD), nanoparticles and photonic crystals. This nanoscale confinement of matter is also a central topic of nano-optics.

Quantum dots are semiconductor particles with a few nanometers in size. Due to the highly confined structure, electrons in QDs are tightly confined in a similar way as in the well-known quantum mechanical 'particle in a well' problem, where electrons are trapped in the potential energy barriers. Therefore, QDs possess discrete electronic states. When QDs are illuminated by light, the electrons in lower energy states will be excited to higher energy states if the photon energy is larger than the bandgap. Then the spontaneous emission allows the excited electrons drop back into the ground state by emitting photons. This process is called the photoluminescence (PL). Different sizes of QDs give different energy gaps and different PL wavelengths. QDs have advantages of high quantum efficiency, long life-time do not photobleach and are widely applicable in fluorescence markers, bio-labels[9] and nano-lasers[10], etc.

Metallic materials can also be fabricated into nanoparticles. Unlike semiconductors where electrons are bound to atoms, metallic materials have electrons with long mean free paths. Therefore, when metallic nanoparticles are irradiated by light, the conduction electrons will oscillate coherently with the oscillating incoming electric fields. When this collective oscillation of electrons is in resonance with the inci-

dent light frequency, the localized surface plasmon modes will be generated. These plasmon modes greatly enhance the electric field near the nanoparticle surfaces and have a maximum optical absorption at the plasmon frequency. Moreover, due to the large surface/volume ratio of nanoparticles, the plasmon frequency can be actively controlled by changing the size and the geometry shape, for example, the aspect ratio[11]. Metallic nanoparticles have various applications in bio-labels, automotive coatings, sunscreen lotions, sensing, etc.[12, 13, 14]

More and more artificial nanostrucutres, such as photonic crystals, nanocomposites and metasurfaces, have recently been created and studied, as shown in Fig. 1.1.[15, 16, 17] They all significantly modify the interaction between light and matter at the subwavelength scale by creating optical near-fields that are free of diffraction. The size-dependent property of far-field optical signals, such as scattering and absorption, makes them attractive for nanophotonic applications. This dissertation will focus on these material platforms and investigate their influence on nonlinear optical signals.

1.1.3 Nanofabrication

The development of nano-optics heavily relies on the development of modern nanofabrication technology, which refers to the manufacturing process of nano-materials discussed above. Generally speaking, nanofabrication methods are categorized into three main parts: lithography, thin film deposition and etching.

Lithography is extremely important in designing nanopatterns on substrates, especially the photolithography and electron beam lithography (EBL). The basic steps of EBL with positive-tone resists to fabricate nanostructures is shown in Fig. 1.2.[18] A resist layer is first deposited on the substrate with spin-coating followed by the thermal treatment, baking for instance, to remove the solvent residue. Next, the resist layer is exposed to the electron beam, which breaks the chemical bonds in desired areas of the resist layer. After developing in chemical solutions, these areas are left

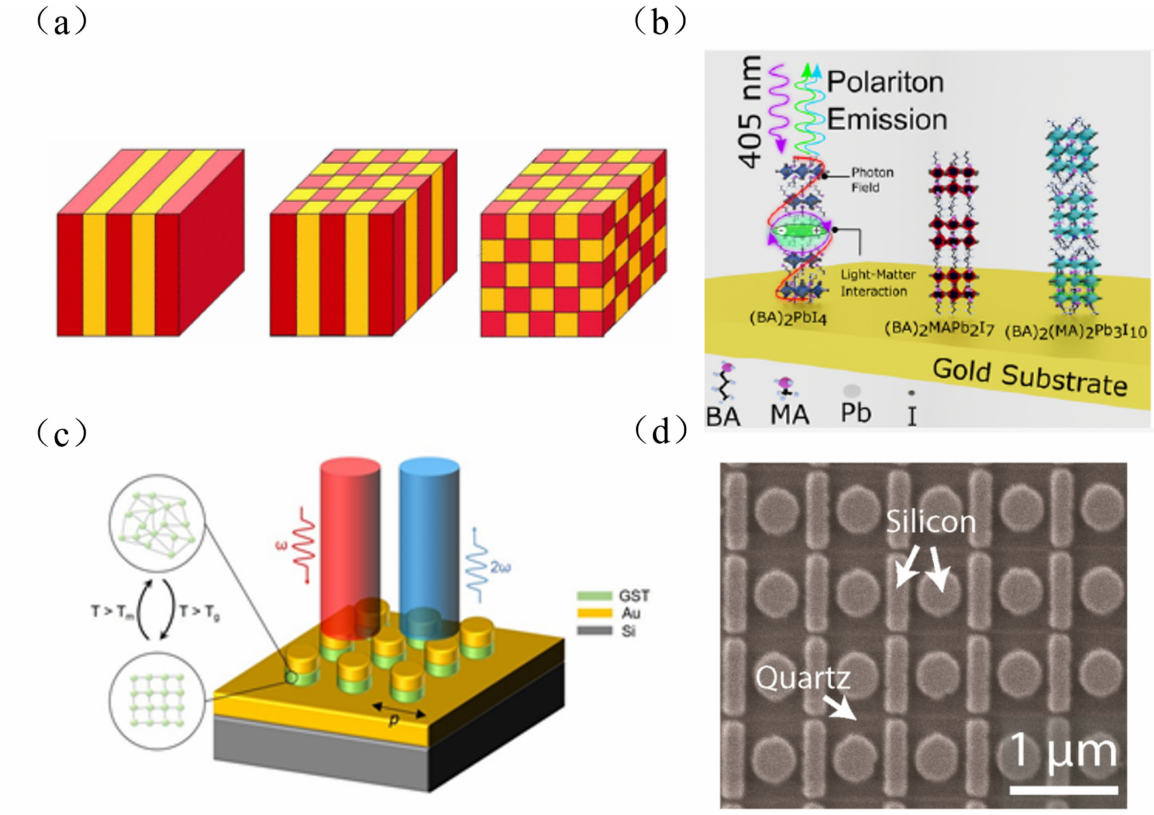

Figure 1.1: (a) Schematic of photonic crystals. Periodic modulation of refractive indices are represented by alternately arranged yellow and red regions. From left to right: 1D photonic crystal, 2D photonic crystal, 3D photonic crystal. (b) Schematic of RP1 flakes ((BA)2PbI4), a type of hybrid organic/inorganic perovskites, on a Au substrate showing photoluminescence from the exciton-polariton formation. A similar phenomenon was also observed in the higher-order systems RP2 ((BA)2MAPb2I7) and RP3 ((BA)2(MA)2Pb3I10). This is an example of nanocomposites that drastically change the light-matter interaction. (c) Schematic of the gold-GST-gold metasurface composed of an array of gold (35nm thick) /GST (25 nm thick) nanodisks on an gold reflector (100 nm thick) and a silicon substrate. The diameter of the nanodisk is selected as 120 nm and the period of the metasurface is marked as p. (d) An SEM image of the silicon metasurface fabricated on the quartz substrate. Panel (b) is reprinted (adapted) with permission from Ref. 16. Copyright 2021 American Chemical Society. Panel (d) is reprinted (adapted) with permission from Ref. 17. Copyright 2015 American Chemical Society.

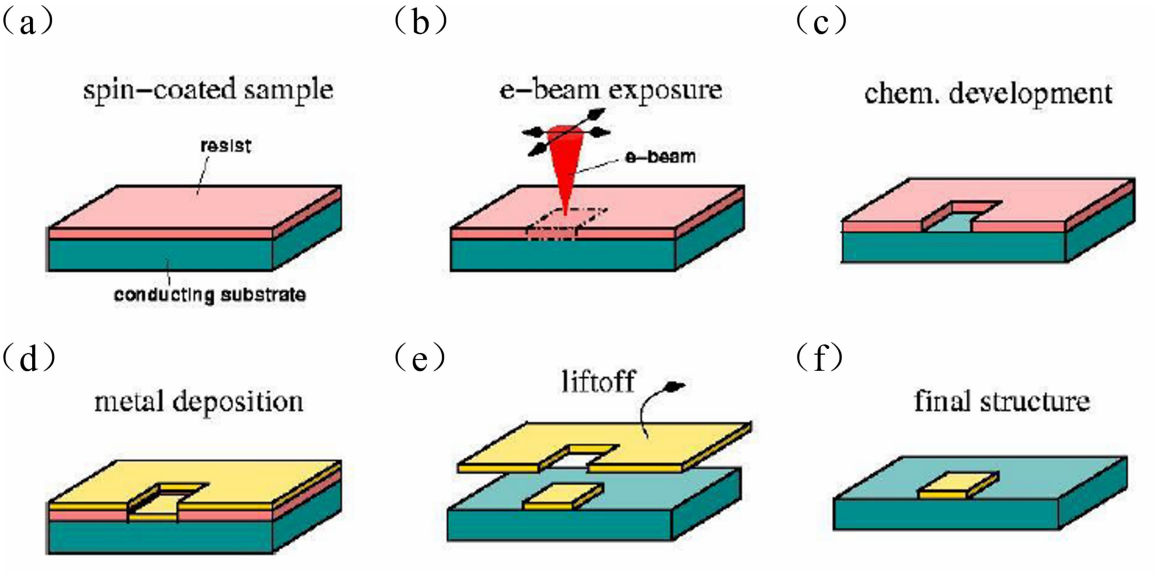

Figure 1.2: Steps of EBL with positive-tone resists to fabricate nanostructures: (a) A resist layer is deposited on a conducting substrate with spin-coating. (b) The resist layer is exposed to the electron beam, which breaks the chemical bonds in desired areas of the resist layer. (c) After developing in chemical solutions, these areas are left blank and mark up the pattern of the nanostructure. (d) Thin films of metal materials are deposited on the resist mask. (e) The resist layer is lifted off in chemical solutions along with the thin film on top. (f) The designed nanostructure is left on the substrate.

blank and mark up the pattern of the nanostructure. Then thin films of metal or dielectric materials are deposited on the resist mask. Finally, the resist layer is lifted off in chemical solutions along with the thin film on top, leaving developed areas the designed nanostructure.

As mentioned above, the thin film deposition is a key step in nanofabrication. Modern nanotechnology allows the accurate thickness control of thin films with the precision of ¡1 nm. Generally, two main deposition methods are adopted: the chemical vapor deposition (CVD) and the physical vapor deposition (PVD).[19, 20] CVD introduces reactant gases in the chamber and chemical reactions occur on wafer surfaces leading to the deposition of a solid film. Without involving chemical reactions, PVD creates vapors of constituent materials inside the chamber, and condensation occurs on wafer surfaces to deposit solid films. Comparing with PVD, CVD allows a

higher growth rate, can grow epitaxial films and has more conformal step coverage. However, it also has disadvantages of too high process temperatures, toxic gasses and more impurities. Other methods, including coating with a liquid that becomes solid upon heating, electro-deposition and thermal oxidation, are increasingly gaining importance in nanofabrication. Choosing which deposition method to use is based on specific requirements of thin film properties. These properties of thin films, including the roughness, stress, stoichiometry, impurity level, etc., depend on complicated parameters used during the deposition process, thus raise wide research interest among laboratories and industry R&D. In this dissertation, the roughness of thin films is determined by the scanning electron microscope (SEM) and the thickness can be read from the atomic force microscope (AFM).

Etching is another critical process in nanofabrication, in which thin layers are removed from the surface of the wafer during manufacturing while some parts protected by the etching-resist mask are left.[21] Categorized by the etchant, there are two fundamental types of etching, namely the wet etching and the dry etching. In wet etching, the substrate is immersed in a bath of liquid-phase etchants. In dry etching, if chemical mechanism dominates, plasma is introduced to carry chemical radicals that could selectively format volatile compounds on the surface of the substrate to remove the deposited solid materials. If physical mechanism dominates, ions which are accelerated by an electrical field would hit the surface with high kinetic energy and bring out materials.

1.2 Nonlinear Optics

Nonlinear optics is the study of light-matter interactions which significantly modify the optical properties of the material system. The term "nonlinear" means that the response of the matter to an applied electric field is nonlinearly dependent on the

strength of the optical field. This response of matter to an external field can be quantified by the matter's polarization:

$$\vec{P(t)} = \sum_i q_i \vec{x_{q_i}}(t) = Nq\vec{x_q}(t) \tag{1.3}$$

where N is the density of charged particle, q_i is the charge of each particle and $\vec{x_q}(t)$ is the displacement of the particle. The polarization represents that charged particles in the material move collectively in response to the applied electric field. According to the inhomogeneous wave equation:

$$\frac{\partial^2 E}{\partial z^2} - \frac{1}{{c_0}^2}\frac{\partial^2 E}{\partial t^2} = \mu_0 \frac{\partial^2 P}{\partial t^2} \tag{1.4}$$

the polarization P acts as the source of the emitted light from the medium. Sine waves of all frequencies are solutions to the homogeneous wave equation. However, the inhomogeneous term only allows the frequency at specific values determined by the polarization. If the medium is linear:

$$\vec{P(t)} = \epsilon_0 \chi^{(1)} \vec{E(t)} \tag{1.5}$$

where $\chi^{(1)}$ is the linear susceptibility and ϵ_0 is the permittivity of free space, then the light propagates through the material without changing the frequency. Nevertheless, in nonlinear optics, the polarization is a general function of the electric field $P(E)$ instead of the linear expression and can be described by the power series:

$$\vec{P(t)} = \epsilon_0[\chi^{(1)}\vec{E(t)} + \chi^{(2)}\vec{E(t)}^2 + \chi^{(3)}\vec{E(t)}^3 + \dots] \tag{1.6}$$

where $\chi^{(2)}$ and $\chi^{(3)}$ are known as the second- and third-order nonlinear optical susceptibilities, respectively. Therefore, other frequencies would occur besides the frequency

of the original optical field. A typical example of nonlinear interaction is the second harmonic generation (SHG), where the emission is generated at the second-harmonic frequency.

Nonlinear optical processes are abundant in nature and some schematics are shown in Fig. 1.3.[22] Second-order nonlinearity which involves $\chi^{(2)}$ include SHG, sum and difference frequency generation, two photon absorption, optical parametric generation (OPG), etc. Third-order processes with a non-negligible $\chi^{(3)}$ include third harmonic generation (THG), four wave mixing (FWM), optical Kerr effects, etc. However, nonlinear optical processes are usually weak due to the small magnitude of high-order susceptibilities and typically can only be generated by lasers that are sufficiently intense. One of the most important theme of this dissertation is to enhance these nonlinear interactions with nanophotonic platforms, which could greatly enhance the optical near-fields to make up for the normally small high-order susceptibilities.

1.2.1 Nonlinear Susceptibility

Nonlinear susceptibility describes the nonlinear electronic responses of charged particles (atoms, electrons, etc.) to the applied optical fields. Both classical and quantum mechanical models are developed to calculate the nonlinear susceptibility. Classical models are based on the Lorentz model and extend the harmonic oscillator description of atoms to anharmonic oscillators. Quantum mechanical models start from the first principle and are more precise in a sense that completed resonance nature of the nonlinear susceptibility are considered while classical models only allow one resonance frequency.

To describe the motion of electrons in a noncentrosymmetric media, the classical model of nonlinear susceptibility adds a quadratic correction term to the Lorentz model[23]:

$$\ddot{\vec{x}} + 2\gamma\dot{\vec{x}} + {\omega_0}^2\vec{x} + a\vec{x}^2 = -\lambda e\vec{E}(t)/m \tag{1.7}$$

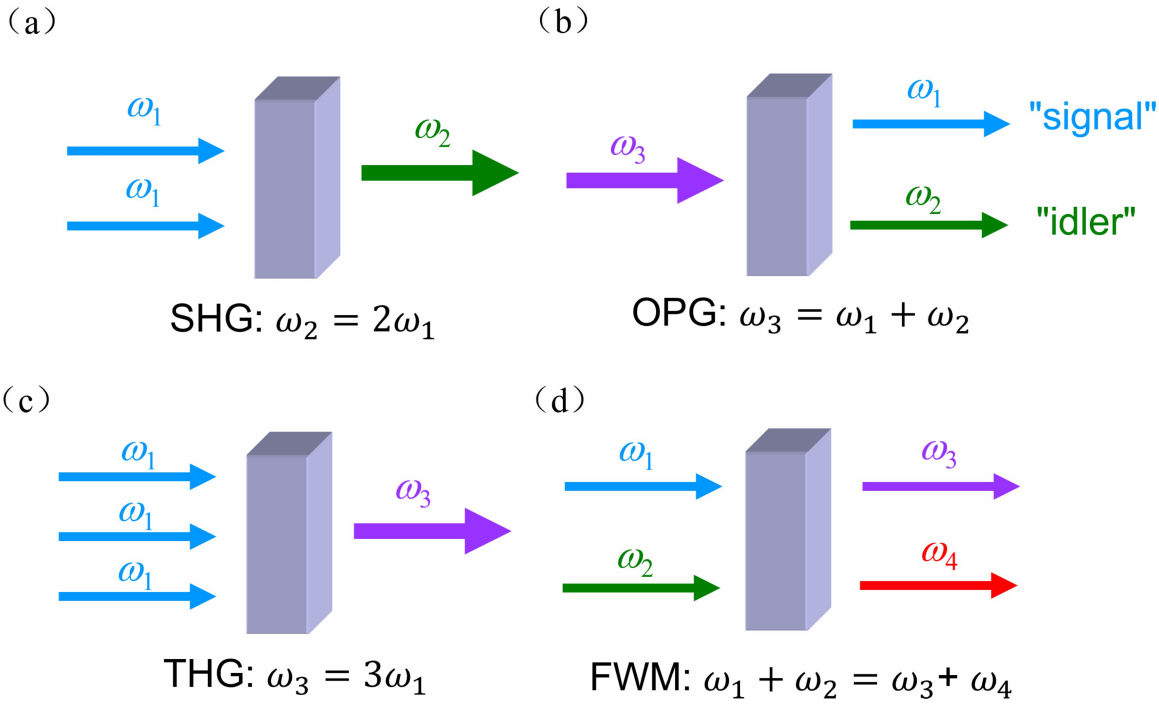

Figure 1.3: Schematic of some nonlinear optical processes. (a) SHG (b) OPG (c) THG (d) FWM. ω_1, ω_2, ω_3 and ω_4 are various photon energies. The conservation of energy in each nonlinear process is rigorously obeyed, as revealed in the formula under each picture.

where γ represents the damping term, a is the characterization of the nonlinearity and λ is a parameter that ranges continuously between zero and one for the convenience of perturbation expansion. The applied optical field can be written as:

$$\vec{E}(t) = E_1 e^{-i\omega_1 t} + E_2 e^{-i\omega_2 t} + c.c. \tag{1.8}$$

where E_1 and E_2 represent the electric field of two incoming light in nonlinear interactions, and ω_1 and ω_2 are the photon energy, respectively. The solution of Eq. 1.7 takes the form of the power series expansion in the strength λ of the perturbation:

$$\vec{x} = \lambda \vec{x}^{(1)} + \lambda^2 \vec{x}^{(2)} + \dots \tag{1.9}$$

Plug Eq. 1.9 into Eq. 1.7 and split Eq. 1.7 according to different orders of λ. Then $\vec{x}^{(1)}$ can be derived from the conventional Lorentz model. $\vec{x}^{(2)}$ denotes the second-order movement. In SHG where two ω_1 photons are interacted, $\vec{x}^{(2)}(2\omega_1)$ can be solved as:

$$\vec{x}^{(2)}(t) = \frac{-a(e/m)^2 {E_1}^2}{D(2\omega_1)D^2(\omega_1)} e^{-2i\omega_1 t} \tag{1.10}$$

where the complex denominator function is:

$$D(\omega_j) = \omega_0^2 - \omega_j^2 - 2i\omega_j\gamma \tag{1.11}$$

Comparing the definition of the polarization in Eq. 1.3 and the definition of the nonlinear susceptibility $\chi^{(2)}$ in Eq. 1.6, it is straightforward to derive $\chi^{(2)}(2\omega_1, \omega_1, \omega_1)$ in SHG in terms of the linear susceptibility:

$$\chi^{(2)}(2\omega_1, \omega_1, \omega_1) = \frac{\epsilon_0^2 ma}{N^2 e^3} \chi^{(1)}(2\omega_1)[\chi^{(1)}(\omega_1)]^2 \tag{1.12}$$

The above analysis can readily be extended to general second-order nonlinear

processes and other higher-order effects by assuming higher order correction terms in Eq. 1.7. It should be noted that in a centrosymmetric media, if $\vec{E}(t)$ is reversed to $-\vec{E}(t)$, then $\vec{P}(t)$ will also be reversed to $-\vec{P}(t)$ accordingly. Substitute $\vec{E}(t)$ with $-\vec{E}(t)$ on the right side of Eq. 1.6 and compare the result with the expression of $-\vec{P}(t)$, all even-order susceptibilities are vanished. Therefore, materials with huge asymmetry are widely used in detecting second-order nonlinearity. While bulk materials with inversion symmetry in the crystalline structure are more investigated in third-order nonlinearity. Modifying the surface structure or introducing phase transition to break the symmetry are necessary when the second-order nonlinearity is needed.

In quantum theory of the nonlinear susceptibility, the Hamiltonian is written as:[23]

$$\hat{H} = \hat{H}_0 + \lambda \hat{V(t)} \tag{1.13}$$

where $\hat{H}_0$ is the Hamiltonian of free atoms and $\hat{V(t)}$ is the coupling between electric dipole moments and the electric field:

$$\hat{V(t)} = -\hat{\mu} \cdot \vec{E(t)} \tag{1.14}$$

The solution of the Schrodinger's equation $\phi(r,t)$ is expanded to power series in λ similarly as in classical oscillator models:

$$\psi(r,t) = \psi^{(0)}(r,t) + \lambda\psi^{(1)}(r,t) + \lambda^2\psi^{(2)}(r,t) + \dots \tag{1.15}$$

Here $\psi^{(0)}(r,t)$ is the wave function of the atom on the ground state g:

$$\psi^{(0)}(r,t) = u_g(r)e^{-iE_g t/\hbar} \tag{1.16}$$

and all high-order contributions of the wave function can be expressed as the super-

position of all eigen-energy states:

$$\psi^{(N)}(r,t) = \sum_l a_l^{(N)}(t) u_l(r) e^{-i\omega_l t} \tag{1.17}$$

where $a_l^{(N)}(t)$ gives the probability amplitude of state l, $u_l(r)$ represents the spatially varying part and ω_l is the eigen-energy of each state. By substituting Eq. 1.15, 1.17 into the Schrodinger's equation and assuming that the optical field has multiple frequency components

$$\vec{E}(t) = \sum_p E(\omega_p) e^{-i\omega_p t} \tag{1.18}$$

the high-order wave function can be derived, which determines the expectation value of the electric dipole moment

$$< \vec{p} >=< \psi|\hat{\mu}|\psi > \tag{1.19}$$

and therefore the nonlinear susceptibility. The second-order susceptibility, for example, is written as

$$\chi^{(2)}_{ijk}(\omega_\sigma, \omega_q, \omega_p) = \frac{N}{\epsilon_0 \hbar^2} P_F \sum_{mn} \frac{\mu^i_{gn} \mu^j_{nm} \mu^k_{mg}}{(\omega_{ng} - \omega_\sigma)(\omega_{mg} - \omega_p)} \tag{1.20}$$

where P_F represents the full permutation operator and ω_{mg}, ω_{ng} defines the energy gap between two states. $\mu_{gn}, \mu_{nm}, \mu_{mg}$ are known as the transition dipole moments. This quantum-mechanical model relates nonlinear susceptibilities to transitions between intrinsic eigen-energy states of atoms, which can be clearly demonstrated in energy-level diagrams, as shown in Fig. 1.4.[23] It can be a useful tool in interpreting nonlinear behaviors in strong light-matter interactions.

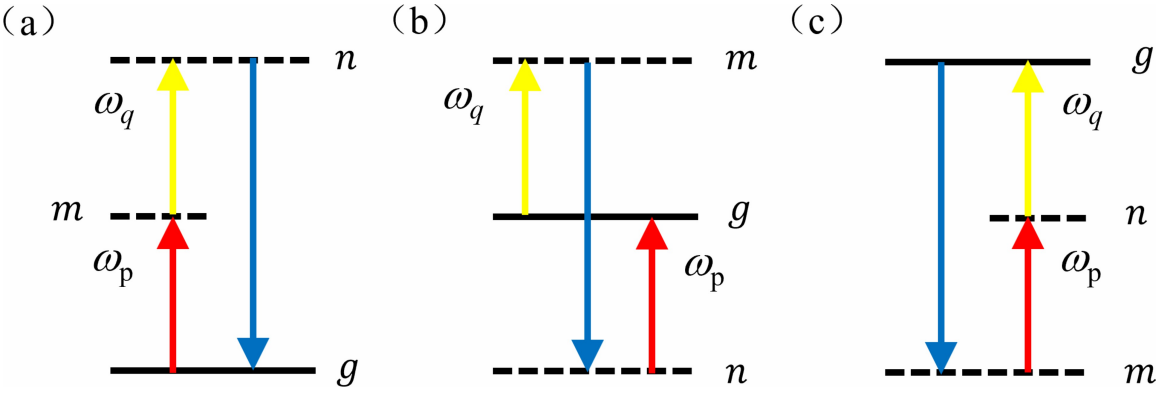

Figure 1.4: Resonance structure of the terms in Eq. 1.20 which relates the second-order nonlinear susceptibility to the transitons between energy levels. Considering the intrinsic permutation symmetry, three transition modes are unique: (a) highly resonant transition (b) partially resonant transition with ω_q in resonance with the transition from the ground level to level m (c) antiresonant transiton.

1.2.2 Second Harmonic Generation

After determining the nonlinear susceptibility, the electric field and the intensity of nonlinear signals can be calculated from the inhomogeneous wave equation Eq. 1.4.[23] As an example, the process of SHG will be considered. Assuming the total electric field inside the nonlinear medium is

$$\vec{E}(z,t) = \vec{E_1}(z,t) + \vec{E_2}(z,t) \tag{1.21}$$

where each component is represented by a slowly varying amplitude $A_j(z)$.

$$\vec{E_j}(z,t) = A_j(z)e^{i(k_j z - \omega_j t)} \tag{1.22}$$

By substituting Eq. 1.21, 1.21 into Eq. 1.4, we obtain the propagation of the amplitude

$$\frac{dA_1}{dz} = \frac{i\omega_1^2 \chi^{(2)}}{k_1 c^2} A_2 A_1^* e^{-i\Delta k z} \tag{1.23}$$

and

$$\frac{dA_2}{dz} = \frac{i\omega_2^2\chi^{(2)}}{k_2c^2}A_1^2e^{-i\Delta kz} \tag{1.24}$$

where $\Delta k = 2k_1 - k_2$. For an undepleted-pump approximation where A_1 is a constant, the spatial dependence of the second-harmonic field amplitude can be readily solved.

It should be noted that if $\Delta k = 0$, this amplitude will increase linearly with the propagation length, which is called phase matching.[24] Phase matching is essentially the conservation of the momentum and can be realized by precisely modulating the incoming light angle, polarization and the refractive index of the medium. Under the phase matching condition, the nonlinear material becomes the gain medium which produces lasing effect when the propagation length is made sufficiently long in a cavity design.

As discussed above, second harmonic signals can only be generated from noncentrosymmetric materials. However, the surface of bulk materials naturally breaks the inversion symmetric which enables SHG. Moreover, this surface contribution of SHG becomes more significant in nanostructures with a large surface/volume ratio. The subwavelength sizes of nanostructures make the wave equation invalid and the large field enhancement brought by the light confinement at nanoscale makes it inaccurate to derive the field distribution using the perturbation theory. Therefore, new theories are needed to describe the nonlinear SHG signals for nanophotonic systems.[25, 26] The hydrodynamic model of SHG signals from the plasmonic nanorods will be introduced in Chapter2.

1.2.3 Optical Kerr Effect

Finally, the optical Kerr effect is briefly introduced as an example of the third-order nonlinear process. Suppose the optical field is of the form

$$\vec{E(t)} = E(\omega)e^{-i\omega t} + c.c. \tag{1.25}$$

the third-order term in Eq. 1.6 contributes a nonlinear polarization that influences the propagation of the original beam at frequency ω

$$P^{NL}(\omega) = 3\epsilon_0\chi^{(3)}|E(\omega)|^2E(\omega) \tag{1.26}$$

An effective susceptibility is introduced to reflect this intensity-dependent modulation of the original susceptibility

$$\chi_{eff} = \chi^{(1)} + 3\chi^{(3)}|E(\omega)|^2 \tag{1.27}$$

and the refractive index is described by

$$n = n_0 + 2n_2|E(\omega)|^2 \tag{1.28}$$

where n_0 is the linear susceptibility and n_2 is proportional to the third-order susceptibility

$$n_2 = \frac{3\chi^{(3)}}{4n_0} \tag{1.29}$$

This intensity-dependent refractive index is also named optical Kerr effect by analogy with the electro-optic Kerr effect where the refractive index of the material is changed by the applied static electric field.[27]

Optical Kerr effect results in many exotic nonlinear processes, including self-focusing[28], optical phase conjugation[29] and two-beam coupling[30]. It is widely applied in designing the ultrafast laser system. Another interesting phenomenon is that when n_0 approaches zero, this modulation of the refractive index becomes infinitely large, which gives rise to the unique nonlinear property of some near-zero-index (NZI) materials.[31]

1.3 Ultrafast Optics

Nonlinear interactions are much weaker compared to linear optical processes, which normally requires the sufficiently intense pump light, such as lasers. A straightforward method to increase the laser intensity without additional external power supply is to produce pulsed lasers instead of continuous waves. By reshaping the laser pulse and decreasing the pulse duration, the peak power of the laser would significantly increase while keeping the same average power. Recent investigation in compressing the pulse duration has been developed rapidly and allows the creation of ultrafast pulses as short as 60 attoseconds.[32] Modern technology of chirped pulse amplification[33] allows the power of these ultrashort pulses to be peta-watts.

Moreover, in nanophotonic systems, the light-matter interactions mostly occur on ultrafast time scales due to the limited length scale that is comparable to the mean free path of electrons (10 nm). Measuring the ultrafast dynamics of these processes would have a profound effect on our understanding of nonlinear optics. For example, PL signals usually occur on nanosecond scale, and the competing non-radiative relaxation can be much faster. Semiconductor processes of technological interest, such as hot electron dissipation and recombination, normally happen on picosecond and femtosecond time scale. The detection of these ultrafast dynamics brings forward the requirement of ultrafast spectroscopy study.[34]

1.3.1 Ultrafast Laser

The model of a laser is a gain medium that amplifies the energy of light through pumping. The laser beam will lase every time it completes a round trip between the cavity and the intensity is amplified by the gain medium. The cavity wall, which can be an output mirror, does not have 100 percent reflection, thus allows the leakage of some power of the laser pulse when hit by the laser travelling inside the cavity.

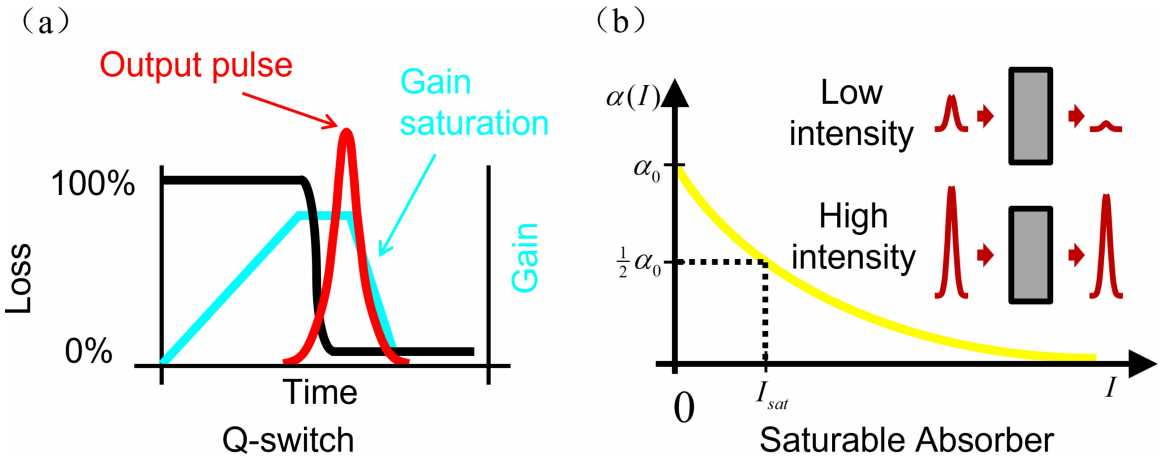

Figure 1.5: Schematics of (a) Q-switch, in which the laser loss is changed from around 100% to zero and the pulse is allowed to lase. The gain increases to the saturation level when the pulse comes out, then returns to zero. (b) saturable absorber, in which the laser absorption decreases with the laser intensity. As the consequence, high-intensity pulses can pass the absorber and low-intensity ones are mostly rejected.

Therefore, the output of any laser is a train of pulses and a continuous wave laser just has a pulse length longer than the round-trip time.

Solid-state laser media are able to yield microsecond to millisecond pulses. However, this pulse duration is limited by the excited-state lifetimes of the gain material, which is typically in the microsecond range. To obtain even shorter pulses, the mode-locking is necessary. Some widely used mode-locking methods are depicted in Fig. 1.5.[34] As shown in Fig. 1.5(a), Q-switch creates nanosecond pulses by changing the laser loss abruptly from around 100% to zero and allowing the laser to lase. This can be achieved with a Pockels cell, which is made of a polarizer and an electro-optical crystal. The crystal acts as a quarter-wave plate when a voltage is applied. It will be switched to a zero-wave plate with zero voltage and the beam polarization will be changed to pass the polarizer.

Another mode-locking method, as shown in Fig. 1.5(b), is the saturable absorber, which only absorbs the low-intensity light and allows the high-intensity part to pass. As the result, the pulse duration becomes shorter with only the vertex of the peak left. A nonlinear crystal, such as a Ti:Sapphire, behaves as a self-saturable abosrber

due to optical Kerr effect. A high-intensity laser experiences a larger modulation of the refractive index and has better overlap with the crystal while a low-intensity one becomes out-of-focus. This mode-locking technique is called Kerr lens.[35] It is passive, which is independent on the external voltage switch speed and thus enables pulses in the picosecond and femtosecond scale.

1.3.2 Pump-probe experiments

After obtaining the ultrafast pulses, ultrafast spectroscopy can be built to investigate the ultrafast dynamics in light-matter interactions. The setup is based on the mechanism of pump-probe, in which a pump beam excites the nonlinear interactions in materials and a probe beam dynamically records the change of optical properties, such as the absorption and the transmission, induced by these interactions. The pump and probe beams are from the same laser source, while the probe beam travels through an additional delay line and arrives on the material surface sometime after the pump beam. Therefore, by precisely tuning the delay length and the delay time, the total relaxation process of any nonlinear signals can be retrieved and depicted in the kinetic spectra. This method has the advantage of a high time resolution, which makes it possible to study femtosecond relaxation processes that are inevitable in nonlinear optics. The pump beam usually has a single wavelength, which can be tuned by the optical parametric amplifer (OPA). The probe beam can either be monochromatic or be the broadband supercontinuum generated from a nonlinear crystal. A schematic of the pump-probe experimental setup is shown in Fig. 1.6.

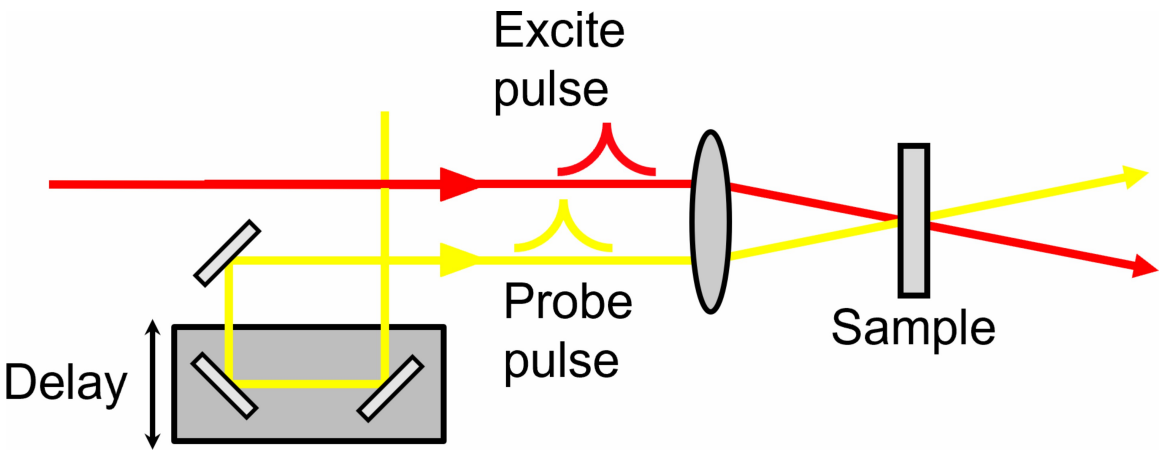

Figure 1.6: Schematic of the pump-probe setup. The pump pulse and the probe pulse are focused on the same spot of the sample. The probe pulse is reflected by several mirrors and travels for an additional distance that is controlled by the delay line. Therefore, the probe pulse arrives after the pump pulse and can detect the ultrafast dynamics of the pump-induced nonlinear processes.

Chapter 2

Second Harmonic Generation from a Single Plasmonic Nanorod Strongly Coupled to a WSe_2 Monolayer

2.1 Cavity QED

Spontaneous emission describes the process where an emitter in the excited state decays into the ground state and meanwhile emits a photon with photon energy equal to the energy difference between these two states. As discussed in the quantum-mechanical model of nonlinear susceptibilities (Chapter 1.2.1), this type of transition is responsible for nearly all light emission and light-matter interactions. However, when the emitter is at the high-energy state, there is no apparent reason for it to decay into the ground state unless it interacts with an external 'field'.[36] This 'field' turns out to be the quantized vacuum field, which can only be described by quantum

electrodynamics (QED).[37] The spontaneous emission rate in the vacuum is

$$\Gamma_0 = \frac{\omega_0^3 \mu_{12}^2}{3\phi\epsilon_0 \hbar c^3} \tag{2.1}$$

where $\hbar\omega_0$ is the energy difference between the ground and excited states and μ_{12} is the transition dipole moment. When the emitter is not in free space, this emission rate will be modified to

$$\Gamma_g = \frac{2\phi\mu_{12}^2 E_0^2}{\hbar^2}\rho(\omega_0) \tag{2.2}$$

where E_0 is the electric field generated by a single photon at the position of the emitter and $\rho(\omega_0)$ is the electromagnetic local density of states (LDOS). It can be inferred that the spontaneous emission rate will be modified by the applied optical field, or in other words, by any change of the electromagnetic environment coupled to the emitter. Depending on the strength of this light-emitter coupling, two different regimes are realized, namely the weak coupling regime and the strong coupling regime.

2.1.1 Weak Coupling

In the weak coupling regime, the excited emitter undergoes an exponential decay at a modified rate Γ_g. For example, when the emitter is placed inside an optical cavity, the LDOS is modified by the cavity mode that coupled to the emitter, which results in the change of the emission rate. This is called the Purcell effect and the ratio between the modified decay rate and the free space emission rate is the Purcell factor

$$F_P = \frac{\Gamma_g}{\Gamma_0} = \frac{3Q\lambda^3}{4\phi^2 V_0} \tag{2.3}$$

where λ is the emission wavelength, Q is the quality factor of the cavity mode and V_0 is the mode volume. In most cases, Purcell effect brings an enhancement of the emission rate. For example, in the first proposal of Purcell in 1946[38], the nuclear

magnetic transition rate was proved to be increased by placing atoms inside a cavity. Recent efforts have been focused on enhancing Raman scattering from molecules that are in vicinity of plasmonic metal nanostructures.[39] Photonic crystals are also widely investigated to modify emission of quantum wells.[40] However, Purcell effect does not necessarily accelerate the emission rate. For some plasmonic cavities, due to the lossy mode featured by the broad line width, the emission rate would even be reduced. This can be interpreted from Eq. 2.3 which shows that the Purcell effect is proportional to Q/V_0. A larger quality factor and a smaller mode volume could bring a larger enhancement of the emission rate, and vice versa. Therefore, the lossy nature of plasmonic cavity modes are overcome by designing resonators with dark modes or by coupling to plasmonic-dielectric hybrid systems to enhance the Purcell factor.[41, 42]

2.1.2 Strong Coupling

In the strong coupling regime, coherent energy exchange between the emitter and the cavity mode occurs. This energy exchange rate, Ω, is faster than any decay process in the coupling system. Therefore, the photon and the emitter no longer possess separate energy states. Instead, they form hybridized states which are called polaritons.[43, 44, 45] The difference between the weak coupling and the strong coupling regime is shown in Fig. 2.1.[46] In Fig. 2.1(a), the inversion versus time for a weak coupling system is still an exponential decay. While in Fig. 2.1(b), the rapid energy exchange rate between the emitter and the cavity results in multiple rounds of energy exchange before the system is fully decayed into the ground level. Therefore, an oscillation occurs within the lifetime of the inversion decay, which is the Rabi oscillation. Rabi oscillation is a key characteristic of the strong coupling.

To correctly describe the physics of a strong coupling system, a classical two-oscillator model is developed (see section 2.2.3). This model assumes that all emit-

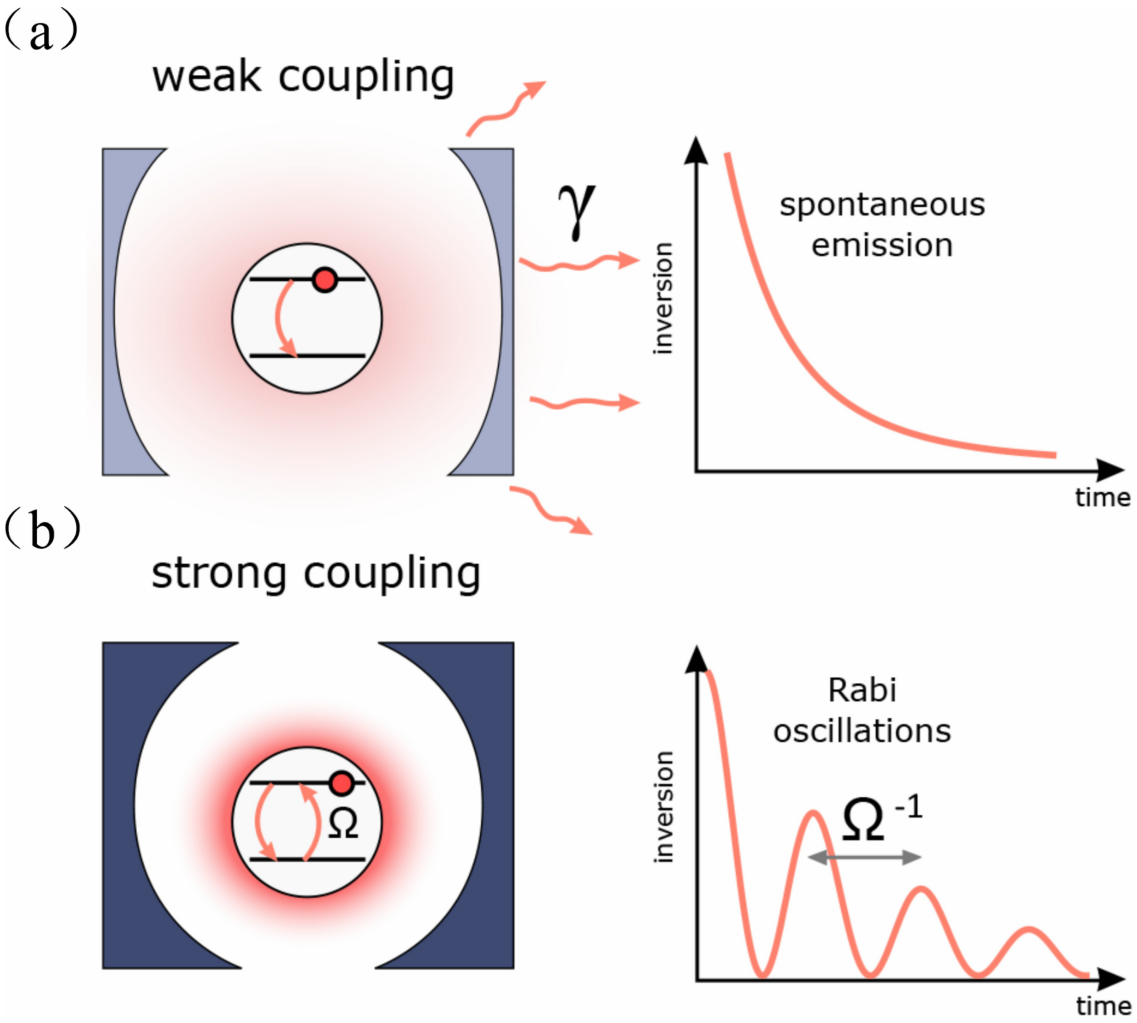

Figure 2.1: Schematic illustration of weak and strong coupling between an optical cavity and a two-level emitter. (a) Weak coupling results in spontaneous decay of the emitter at a rate γ accompanied by emission of a photon. (b) Strong coupling results in Rabi oscillations of the emitter population inversion at a rate Ω. Reprinted (adapted) with permission from Ref. 46. Copyright 2018 American Chemical Society.

ters have a collective resonance mode, which is valid in most cases. While a detailed quantum theory which treats each emitter separately is needed to describe multiple resonance frequencies and multi-photon interactions. A Jaynes-Cummings (JC) model[47] is first proposed with the Hamiltonian in the form

$$\hat{H} = \hbar\omega_0\hat{\sigma}^\dagger\hat{\sigma} + \hbar\omega\hat{a}^\dagger\hat{a} + \hbar g(\hat{\sigma}\hat{a}^\dagger + \hat{\sigma}^\dagger\hat{a}) \tag{2.4}$$

where ω_0 is the emission frequency, $\hat{\sigma}^\dagger$ and $\hat{\sigma}$ are raising and lowering operator of the emitter, ω is the cavity mode frequency and $\hat{a}^\dagger$ and $\hat{a}$ are photon creation and annihilation operators. The coupling strength g is related to the transition dipole moment μ_{12} and the vacuum field E_0

$$g = -\frac{\mu_{12}E_0}{\hbar} \tag{2.5}$$

Assuming $|1>$ and $|2>$ are the ground and excited states of the emitter and $|n>_c$ is the cavity Fock state where n denotes the number of photons that occupy the cavity mode, the eigenstates of a free system omitting the coupling term are

$$|i, n>= |i> \otimes |n>_c, i = 1, 2 \tag{2.6}$$

Then the eigenstates of the coupled Hamiltonian in Eq. 2.4 assuming $\omega_0 = \omega$ are

$$|n+1, \pm>= \frac{|1, n+1> \pm |2, n>}{\sqrt{2}}, n \geq 0 \tag{2.7}$$

which represent the upper polariton and lower polariton states. The corresponding eigenenergies are given by

$$E_n^\pm = n\hbar\omega_0 \pm g\sqrt{n} \tag{2.8}$$

It is clearly demonstrated that the coupling opens up the energy gap between upper

polaritons and lower polaritons. This energy gap

$$\Omega = 2g\sqrt{n} \tag{2.9}$$

is referred to as the Rabi splitting. In the absence of the coupling strength, the eigenstates of the system are the direct product of $|1>$, $|2>$ and the cavity Fock state $|n>$. When g is small, the coupling term is perturbative and the Rabi splitting is easily blurred out by decay and dephasing in the system. When g is large enough, the incoherent processes no longer kill the polaritonic states and the system enters the strong coupling regime. To describe the crossover between two coupling scenarios, it is necessary to introduce losses. Assuming the phenomenological cavity and emitter amplitude decay rates are $\gamma_c av$ and $\gamma_e m$, the non-Hermitian lossy Hamiltonian becomes[48]

$$H_{loss} = \begin{pmatrix} \omega_0 - i\gamma_{em} & g \\ g & \omega - i\gamma_{cav} \end{pmatrix} \tag{2.10}$$

Diagonalization of this Hamiltonian gives two eigenenergies

$$E_{\pm} = \frac{\omega + \omega_0}{2} - \frac{i}{2}(\gamma_{em} + \gamma_{cav}) \pm \sqrt{g^2 + \frac{1}{4}(\delta - i(\gamma_{em} - \gamma_{cav}))^2} \tag{2.11}$$

where $\delta = \omega - \omega_0$ represents the detuning. In the resonant case, the Rabi splitting becomes

$$\Omega = \sqrt{4g^2 - (\gamma_{em} - \gamma_{cav})^2} \tag{2.12}$$

It can be inferred that the coupling strength g has to be larger than $|\gamma_{em} - \gamma_{cav}|/2$ to enable a real-valued Rabi splitting.[45, 49] More rigorously, the Rabi splitting must exceed the polariton line widths to guarantee that two polaritonic states are

resolvable[50, 51], which means

$$\Omega > \gamma_{em} + \gamma_{cav} \tag{2.13}$$

However, the criteria of strong coupling is more commonly considered to be[45, 52]

$$g > \frac{1}{4}(\gamma_{em} + \gamma_{cav}) \tag{2.14}$$

which means at least one complete Rabi oscillation occurs during the decay lifetime.

Employing a single emitter is often not sufficient enough to get an observable Rabi splitting and further studies would focus on the coupling between the cavity and an ensemble of emitters. Assuming N emitters couple to the same cavity mode, the JC Hamiltonian now is modified to the Tavis-Cummings (TC) Hamiltonian[53]

$$H_{TC} = \sum_j \hbar\omega_0 \hat{\sigma}_j^\dagger \hat{\sigma}_j + \ \hbar\omega \hat{a}^\dagger \hat{a} + \sum_j \hbar g_j (\hat{\sigma}_j \hat{a}^\dagger + \hat{\sigma}_j^\dagger \hat{a}) \tag{2.15}$$

Although the eigenstates are substantially different from JC Hamiltonian, some representative states remain similar. For example, the ground state

$$|G> = |1, \cdots, 1> \otimes |0>_c \tag{2.16}$$

would not be affected by the interaction. For N identical emitters, the two polaritonic states have become two bright dressed states

$$|1, \pm> = \frac{|1, \ldots, 1> |1>_c \pm \frac{1}{\sqrt{N}} \sum_j \hat{\sigma}_j^\dagger |1, \ldots, 1> |0>_c}{\sqrt{2}} \tag{2.17}$$

with two corresponding energies

$$E_\pm = \hbar\omega_0 \pm g\sqrt{N} \tag{2.18}$$

In weak excitations which means far below saturation of all two-level systems, these identical emitters behave in quite a similar way like a giant harmonic oscillator giving rise to a Rabi splitting $g\sqrt{N}$. Consequently, the factor $\sqrt{N}$ has greatly enlarged the Rabi splitting, making it more accessible to realize observation. In addition to two bright states, (N-1) dark states are generated that are orthogonal to $|1, \pm >$ states

$$|D >= \frac{1}{\sqrt{2}} \left(\hat{\sigma}_1^\dagger - \hat{\sigma}_j^\dagger \right) |G >, j > 1 \tag{2.19}$$

These states are 'dark' because the transition dipole moment between the ground state and any of these states is zero, that is, they cannot be populated by an external pump.

Strong coupling has enabled abundant novel phenomena, such as control of the optical Stark effect[54], polariton lasing[55], polariton condensation[56] and control of chemical reactivity.[57, 58] Recently more research has been conducted in plasma-induced resonance energy transfer[59], quantum correlations from polaritons[60] and polaron-polariton interactions.[61] Larger coupling strength has also been investigated and realized which opens a new era of ultra-strong coupling (USC) and deep-strong coupling (DSC).[62] Besides these fundamental phenomena, the strongly coupled systems also have the potential to enable applications in optoelectronic devices, optical sensors, and quantum computing.[63, 64, 65, 66, 67, 68]

2.2 Plasmon-exciton Strong Coupling

To reach the strong coupling regime, according to Eq. 2.3, it is required to confine light either in a small mode volume V_0 or in a low loss cavity (high Q). However, these two requirements are contradictory, as a tighter confinement usually means a higher loss of energy. Therefore, the direction of the study in strong coupling systems is to optimize this trade-off to some extent. Early experiments typically used

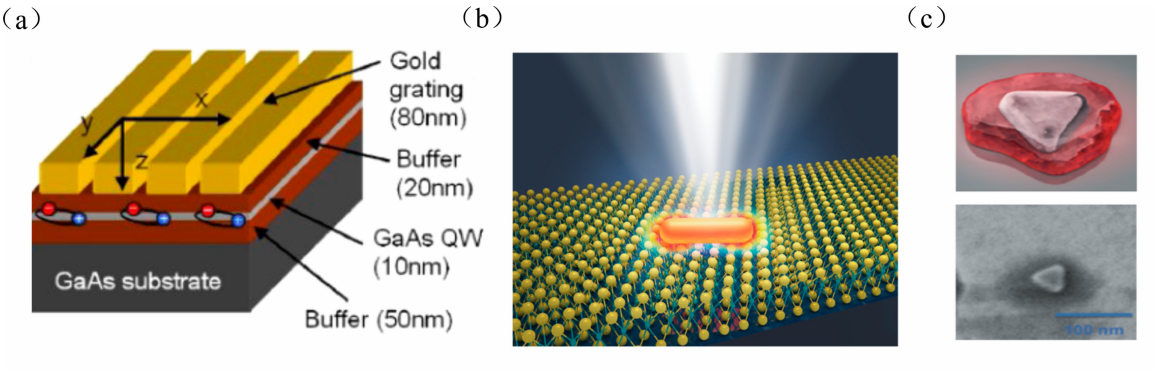

Figure 2.2: Overview of various platforms that exhibit strong coupling (a) GaAs quantum wells coupled to gold a nanogroove array. (b) an individual gold nanorod coupled to the monolayer WS_2. (c) A silver nanoprism strongly coupled to J-aggregates. Panel (a) is reprinted (adapted) with permission from Ref. 89. Copyright 2008 American Physical Society. Panel (b) is reprinted (adapted) with permission from Ref. 82. Copyright 2017 American Chemical Society. Panel (c) is reprinted (adapted) with permission from Ref. 77. Copyright 2017 American Chemical Society.

high-quality-factor dielectric cavities such as Fabry-Perot resonators[69, 70], photonic crystals[71], whispering-gallery-mode resonators[72] and distributed-Bragg-reflector cavities[73] with relatively large mode volumes restricted by the diffraction limit of light. By contrast, metal plasmonic nanocavities such as single nanospheres[74], nanorods[75] (NR) and nanocomposites are not subject to the diffraction limit and provide deep subwavelength interaction volumes.

Several material platforms have been used for strong coupling to plasmonic nanocavities, including quantum dots and molecular excitons.[70, 76, 77, 78, 79, 80, 81] Recent progress in the fabrication and characterization of transition metal dichalcogenides (TMDs) has enabled several demonstrations of strong coupling between plasmons and excitons in these TMDs.[74, 82, 83, 84, 85, 86, 87, 88] In this dissertation, a particular strong coupling system consisting of a single gold nanorod and a monolayer of WSe_2, a type of TMD material, will be utilized. Several other typical platforms that could realize strong coupling are summarized in Fig. 2.2.[89, 82, 77]

2.2.1 Plasmonics

Plasmons are widely used as optical cavities to reach the strong coupling regime. One choice involves the use of propagating surface plasmons, which localize the field on the scale of skin depth and significantly reduce the mode volume.[90, 91, 92] Recently, metallic nanostructures which support localized surface plasmons emerge as new choices for optical cavities in pursuit of even smaller mode volumes.[74, 75, 93] The intense near fields in the vicinity of the nanostrucutres provide high photonic density of states that significantly enhance the coupling strength.

To understand how plasmonic nanocavities are involved in the strong coupling, it is of great importance to first give an introduction to the basic principles of plasmons, which represent the density fluctuation of free electrons under the excitation of light. Plasmons can be generated in bulk, surfaces and nanoparticles in the sub-wavelength scale. In bulk materials, the free electrons can be described by the Drude model and the plasma frequency is

$$\omega_p = \sqrt{\frac{Ne^2}{m\epsilon_0}} \tag{2.20}$$

Plasmon could also occur on the surface, for example, the metal-dielectric interface, with the plasmon frequency controlled by the incident light wave vector $k(\omega)$. By solving Maxwell's equations with boundary conditions, the dispersion relation can be derived

$$k_x = \frac{\omega}{c}(\frac{\epsilon_m \epsilon_d}{\epsilon_m + \epsilon_d})^{1/2} \tag{2.21}$$

where k_x is the wave vector along the surface, ϵ_m and ϵ_d are permittivity of the metal and the dielectric layer, respectively. However, the surface plasmon cannot be directly coupled by light coming from the dielectric layer because of the momentum mismatch. Several types of additional configurations are needed to generate surface plasmons, among which the Kretschmann configuration, the Otto configuration and the gratings are most frequently adopted, as shown in Fig.2.3.[94]

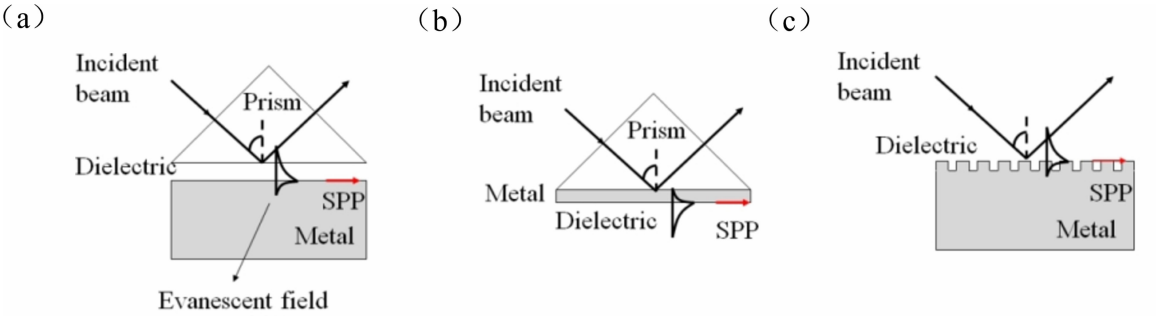

Figure 2.3: Configurations for generating the surface plasmon resonance: (a) Otto configuration (b) Kretschmann configuration (c) diffraction grating

Surface plasmons can also be generated in metalic nanoparticles, while the sub-wavelength scale of these nanostructures limits the propagation of surface waves, which results in the localized surface plasmon resonances. As mentioned in Section 1.1.2, the frequency of these localized plasmon resonances depends on the sizes and geometric shapes of nanoparticles. For example, the resonance frequency of the nanosphere is analytically described by Mie scattering theory which expands the electric field in a spherical multipole basis. The scattering cross section with the dipole approximation is

$$C_{scat} = \frac{8\phi\epsilon_d^2\omega^4 r^6}{3c^4}|\frac{\epsilon_p(\omega)-\epsilon_d}{\epsilon_p(\omega)+2\epsilon_d}|^2 \tag{2.22}$$

where r is the sphere radius and ϵ_p is the permittivity of the particle. Considering a lossless medium ϵ_m, the scattering cross section is maximized when

$$Re(\epsilon_p(\omega)) = -2\epsilon_m \tag{2.23}$$

which corresponds to the resonance frequency of the plasmon.

2.2.2 TMD materials

TMD materials, benefiting from several advantages, are commonly used in strong coupling systems. First of all, as shown in Fig.2.4(a)(b)[95, 96], the monolayer WSe_2

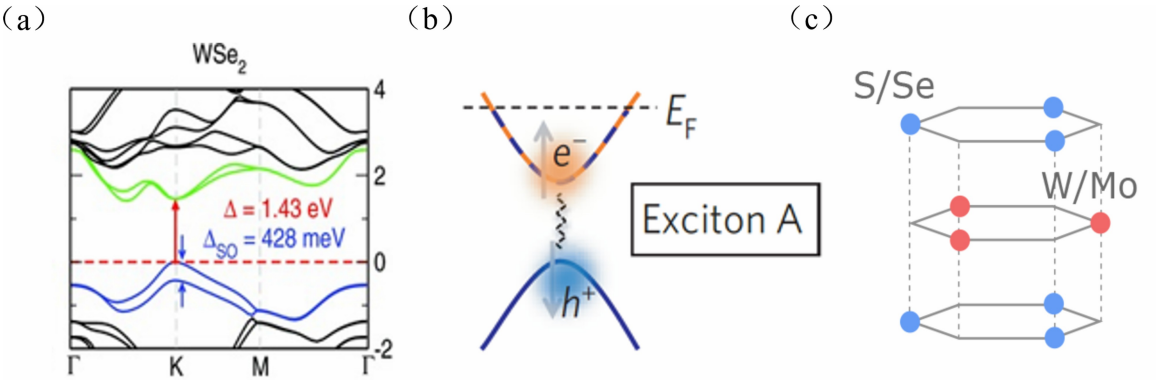

Figure 2.4: (a) The band structure of a monolayer WSe_2. (b) Schematic of an A-exciton at the K point of the monolayer WSe_2. (c) The Crystalline structure of 2D TMD materials. Panel (a) is reprinted (adapted) with permission from Ref. 95. Copyright 2014 John Wiley and Sons. Panel (b) is reprinted (adapted) with permission from Ref. 96. Copyright 2013 Springer Nature. Panel (c) is reprinted (adapted) with permission from Ref. 46. Copyright 2018 American Chemical Society.

shows a direct band gap which supports exciton mode that can act as emitter. The binding energy of these excitons is large enough to support room temperature PL emission.[97] Second, the two-dimensional geometry of these materials results in large in-plane dipole moments in the interaction area, significantly increasing coupling with the cavity mode. Finally, the crystalline structure of monolayer TMD materials, as depicted in Fig.2.4(c)[46], breaks the centrosymmetry and potentially gives rise to a large SHG signal.

2.2.3 Nonlinearity of Plasmon-exciton Strong Coupling

So far, studies of strong coupling systems have been limited to their linear optical response. However, their nonlinear optical response has the potential to provide new routes for the development of nanoscale optoelectronic devices. For example, the nonlinearities may enable efficient entangled photon generation, compact wave mixing, and phenomena essential for optical quantum technologies and nanophotonic platforms. Additionally, the nonlinear signals can be potentially used to learn about the properties of underlying electronic states of the system, for example, by probing

the symmetries of polaritonic wave functions.

Nonlinear signal generation in the strong coupling regime has been studied using various platforms, as shown in Fig.2.5. For example, previous studies have focused on SHG from excitons coupled to $GaAs$ microcavities[98, 99], and THG enhancement has been observed from polymethine dye-microcavity coupled systems.[100] Furthermore, SHG enhancement from WS_2-Ag nanocavity systems has been reported in the weak coupling regime.[101] Finally, a splitting of pump-dependent SHG spectral peaks due to the formation of polaritonic states was observed for J-aggregates embedded in Fabry-Perot cavities.[70] However, to our knowledge, no work has previously studied nonlinear signal generation from plasmon-exciton polaritons in a single nanocavity.

We first start with a classical theoretical description of strong coupling with the two-oscillator model. Then we show that this two-oscillator model can be extended to study nonlinearity of strong coupling systems by adding the nonlinear coupling term. Finally, we experimentally demonstrate SHG from single gold nanorods coupled to a monolayer of WSe_2. The pump-frequency-dependent nonlinear signal shows a distinct spectral splitting, which agrees with the prediction from finite difference time domain (FDTD) simulations and the nonlinear two-oscillator model.[93]

2.2.4 Nonlinear Two-oscillator Model

The linear two-oscillator model treats the dipole moment of the plasmon $\mu_p l$ and the exciton[102, 103, 52] $\mu_e x$ as a pair of coupled harmonic oscillators

$$\ddot{\mu}_{pl} + \gamma_{pl}\dot{\mu}_{pl} + \omega_{pl}^2\mu_{pl} = F_o + g\left(\omega_{pl}d_{pl}/d_{ex}\right)\mu_{em} \tag{2.24}$$

$$\ddot{\mu}_{ex} + \gamma_{ex}\dot{\mu}_{ex} + \omega_{ex}^2\mu_{ex} = g\left(\omega_{ex}d_{ex}/d_{pl}\right)\mu_{pl} \tag{2.25}$$

where $\gamma_p l$ is the line width of the plasmon, $\omega_p l$ is the resonance frequency of the plasmon and $d_p l$ is the polarizability of the plasmon. $\gamma_e x$, $\omega_e x$ and $d_e x$ are the

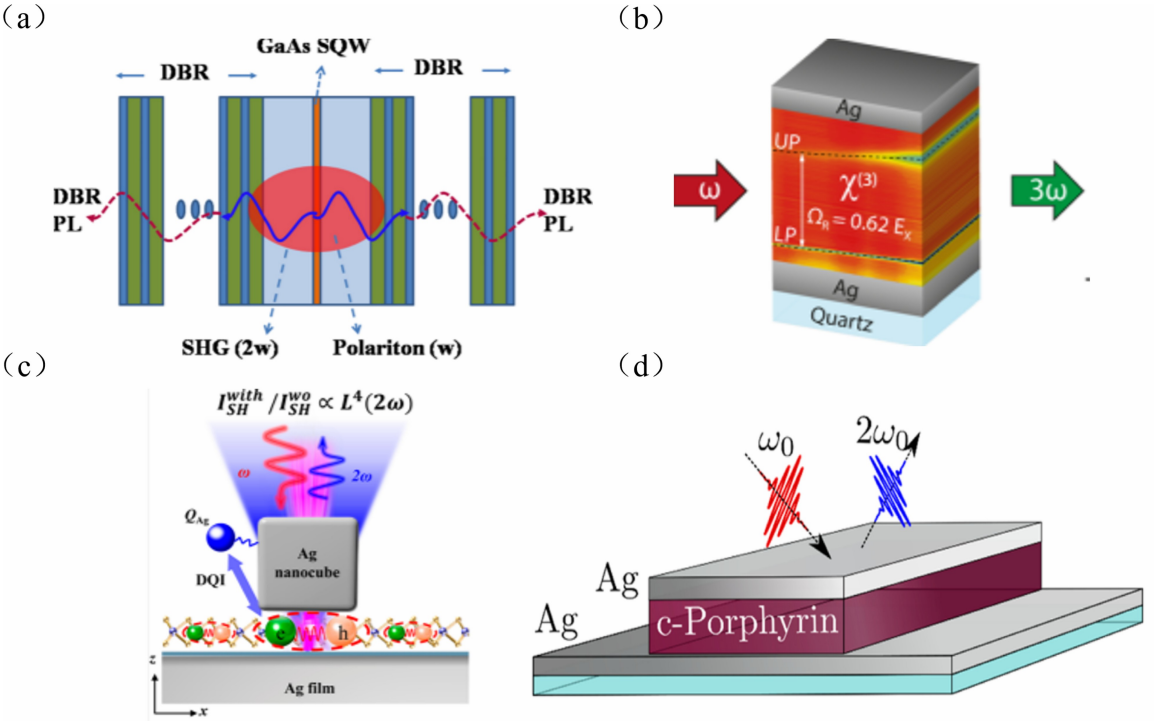

Figure 2.5: Nonlinear optics in strong coupling systems. (a) A GaAs single quantum well (SQW) is strongly coupled to a microcavity. The cavity mirrors are diffraction Bragg reflectors (DBR). Experimental observations of SHG from polaritons in the system exhibit a 2 order higher efficiency than those from the usual method. (b) A strong third-order nonlinearity is given by the polaritonic mode from a nonlinear polymethine dye embedded within a high-Q silver microcavity. (c) The enhanced SHG from a monolayer WS_2 coupled to a plasmonic nanocavity is experimentally and theoretically investigated. The nanocavity is comprised of monodispersed Ag nanocubes separated from an Ag film by a spacer Al_2O_3. (d) Organic nanofiber crystals are hybridized with the optical modes of silver microcavities in the strong coupling regime. The wavelength dependence of the SHG efficiency displays two intense peaks corresponding to the polaritonic modes. Panel (a) is reprinted (adapted) with permission from Ref. 99. Copyright 2018 American Chemical Society. Panel (b) is reprinted (adapted) with permission from Ref. 100. Copyright 2018 American Chemical Society. Panel (c) is reprinted (adapted) with permission from Ref. 101. Copyright 2020 American Chemical Society. Panel (d) is reprinted (adapted) with permission from Ref. 70. Copyright 2016 American Chemical Society.

corresponding terms for the exciton. The external optical field is assumed to produce a driving force F_o on only the plasmon, because it polarizability is much greater than that of the exciton with more free electrons. The larger polarizability of the plasmon also means that only its dipole contributes to the scattering cross section $\sigma_s cat$

$$\sigma_{scat} \propto \left|\omega^2 \mu_{pl}^{(1)}\right|^2 \tag{2.26}$$

with the steady-state solution for the dipole given by

$$\mu_{pl} = \frac{F_o\left(\omega_{ex}^2 - \omega^2 - i\omega\gamma_{ex}\right)}{\left(\omega_{ex}^2 - \omega^2 - i\omega\gamma_{ex}\right)\left(\omega_{pl}^2 - \omega^2 - i\omega\gamma_{pl}\right) - \omega_{ex}\omega_{pl}g^2} \tag{2.27}$$

The nonlinear two-oscillator model adds nonlinear terms to Eq. 2.24 and Eq. 2.25. Assuming the nonlinear term is quadratic, then Eq. 2.24 and Eq. 2.25 become[104]

$$\ddot{\mu}_{pl} + \gamma_{pl}\dot{\mu}_{pl} + \omega_{pl}^2\mu_{pl} + a\mu_{pl}^2 = F_o + g\left(\omega_{pl}d_{pl}/d_{ex}\right)\mu_{ex} \tag{2.28}$$

$$\ddot{\mu}_{ex} + \gamma_{ex}\dot{\mu}_{ex} + \omega_{ex}^2\mu_{ex} + b\mu_{ex}^2 = g\left(\omega_{ex}d_{ex}/d_{pl}\right)\mu_{pl} \tag{2.29}$$

where a and b are proportional to the second-order nonlinear susceptibility of the plasmon and the exciton, respectively. These coupled nonlinear equations can be solved in the perturbation limit[23]

$$\mu_{pl} = \mu_{pl}^{(1)}e^{i\omega t} + \mu_{pl}^{(2)}e^{2i\omega t} + \ldots \tag{2.30}$$

$$\mu_{ex} = \mu_{ex}^{(1)}e^{i\omega t} + \mu_{ex}^{(2)}e^{2i\omega t} + \ldots \tag{2.31}$$

The linear terms $\mu_{pl}^{(1)}$ and $\mu_{ex}^{(1)}$ are the same as the solutions to the linear equations Eq. 2.24 and Eq. 2.25, whereas the second-order terms are given by

$$\mu_{pl}^{(2)} = \frac{aF_o^2(\omega_{ex}^2 - \omega^2 - i\omega\gamma_{ex})^2}{(\omega_{pl}^2 - 4\omega^2 - i\omega\gamma_{pl})[(\omega_{ex}^2 - \omega^2 - i\omega\gamma_{ex})(\omega_{pl}^2 - \omega^2 - i\omega\gamma_{pl}) - \omega_{ex}\omega_{pl}g^2]^2} \quad (2.32)$$

and

$$\mu_{ex}^{(2)} = \frac{bF_o^2(\frac{g\omega_{ex}d_ex}{d_pl})^2}{(\omega_{ex}^2 - 4\omega^2 - i\omega\gamma_{ex})[(\omega_{ex}^2 - \omega^2 - i\omega\gamma_{ex})(\omega_{pl}^2 - \omega^2 - i\omega\gamma_{pl}) - \omega_{ex}\omega_{pl}g^2]^2} \quad (2.33)$$

The second-order (hyper-Rayleigh) scattering cross section is given by

$$\sigma_{SHG} \propto \left|\omega^2\mu_{pl}^{(2)}\right|^2 + \left|\omega^2\mu_{ex}^{(2)}\right|^2 \quad (2.34)$$

For the same reason that we neglect linear scattering from the exciton, we neglect the second term in Eq. 2.34 due to the much larger polarizability of the plasmon.

2.3 Experiments

Experiments are carried out to demonstrate SHG from single nanorods strongly coupled to a monolayer of WSe_2. The schematic of the coupled system is shown in Fig. 2.6. The gold nanorods are designed to support longitudinal plasmonic resonances around 1.66 eV (750 nm), matching the A-exciton transition of the monolayer WSe_2.[105] Excitation of these plasmon modes gives rise to confined in-plane electric fields at the surface of the WSe_2 flake, enabling coupling to excitons in the TMD. The details of all methods used in experiments are introduced below.

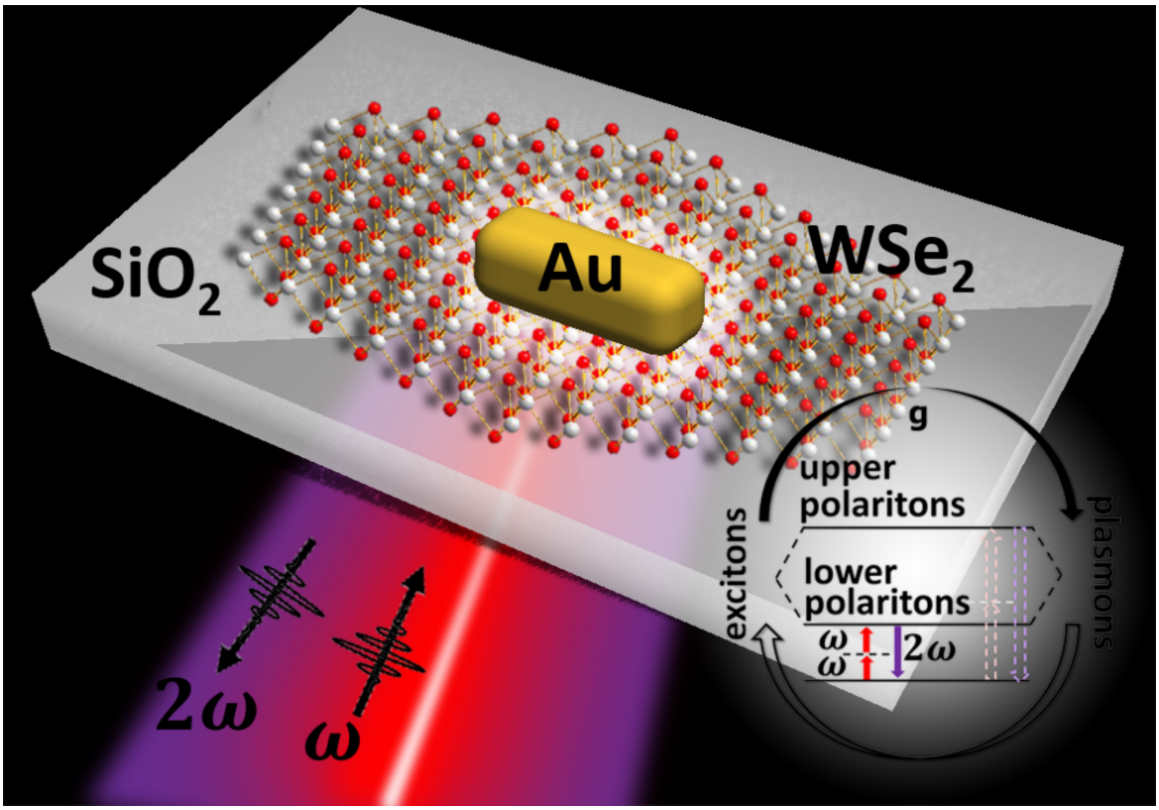

Figure 2.6: Schematic of the experimental setup. An isolated gold nanorod is strongly coupled to a monolayer of WSe_2 on a glass substrate. The second-harmonic signal at frequency 2ω, excited by a fundamental beam at frequency ω, is collected in the epi-illumination configuration. Reprinted (adapted) with permission from Ref. 93. Copyright 2020 American Chemical Society.

2.3.1 Sample Fabrication

Atomically thin layers of WSe_2 are mechanically exfoliated to a PDMS tape and then transferred to glass coverslips. Before transfer, the coverslips are ultrasonically cleaned in soap, deionized water, acetone and IPA for 20 minutes in each solvent and then dried using nitrogen. This method ensures the single crystalline structure of each WSe_2 flake.

To add gold nanorods on top of the flake, we adopt the drop casting method described in the previous literature.[75] An aqueous solution of colloidal gold nanorods with a diameter of 40 nm and an average length of 112 nm (Nanopartz Inc.) is 20-fold diluted with deionized water and sonicated to reduce aggregation. It should be noted that the lengths of nanorods in the solution are distributed around the average length, so that the plasmon resonances of different individual rods will have different detunings relative to the exciton transition frequency in WSe_2. One microliter of the diluted nanorod solution is then drop-cast onto the substrate with the WSe_2 flake and washed off with deionized water after 1 min. These casting parameters result in around 30 NRs on each several-micron-sized WSe_2 flake. The nanorods are functionalized as synthesized with a CTAB layer, which acts as a spacer between gold nanorods and the WSe_2 flake to avoid charge transfer.

2.3.2 Optical Characterization

A 633 nm HeNe laser is used for PL measurements on monolayer WSe_2 flakes. A 50x objective, the numerical aperture (NA) of which is 0.5, is used to focus the excitation beam on the sample and to collect PL signals in the epi-illumination configuration. PL maps are obtained by raster scan of the sample using an XY piezo stage and collecting the PL signals with an avalanche photodiode (APD). An Andor spectrometer equipped with a silicon charge coupled device (CCD) is used to measure the PL spectrum. The optical path of PL measurements is shown in Fig. 2.7. The scanning maps

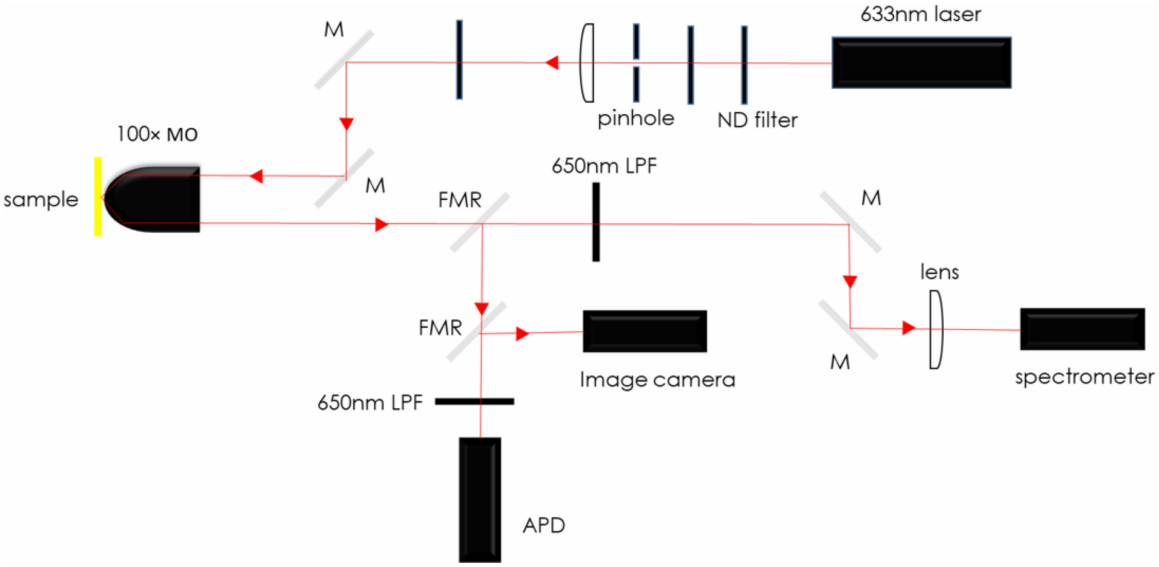

Figure 2.7: The setup schematic of PL measurements. ND filter: neutral density filter; M: mirror; MO: microscope objective; FMR: flip-mirror reflector; LPF: long pass filter; APD: avalanche photodiode.

of several monolayer flakes and the corresponding PL spectra are shown in Fig. 2.8.

Dark-field scattering spectra are measured by focusing broadband light from a halogen lamp on the sample using a dark-field condenser lens. A 50× objective (NA = 0.5) is used to collect the scattered light while omitting the transmitted light. The optical path of dark-field scattering measurements is shown in Fig. 2.9.

SHG measurements are conducted to investigate nonlinear optical properties from these strong coupling systems. A Chameleon Ultra II Ti:sapphire femtosecond laser with a repetition rate of 80 MHz is used as the excitation source. A 60× oil immersion objective (NA=1.4) is used to confocally focus the excitation beam and collect the SHG signals. The schematic of the optical setup used to measure SHG is shown in Fig. 2.10. To avoid the influence of higher-order plasmonic modes, a paraxial beam with a diameter of 2 mm at the objective-lens back focal plane is used, ensuring near normal incidence of the excitation laser beam. Nonlinear spectroscopy is performed by continuously tuning the pump from 700 to 800 nm (3.1 to 3.6 eV) and recording the SHG spectrum for every excitation wavelength. To remove the broadband emis-

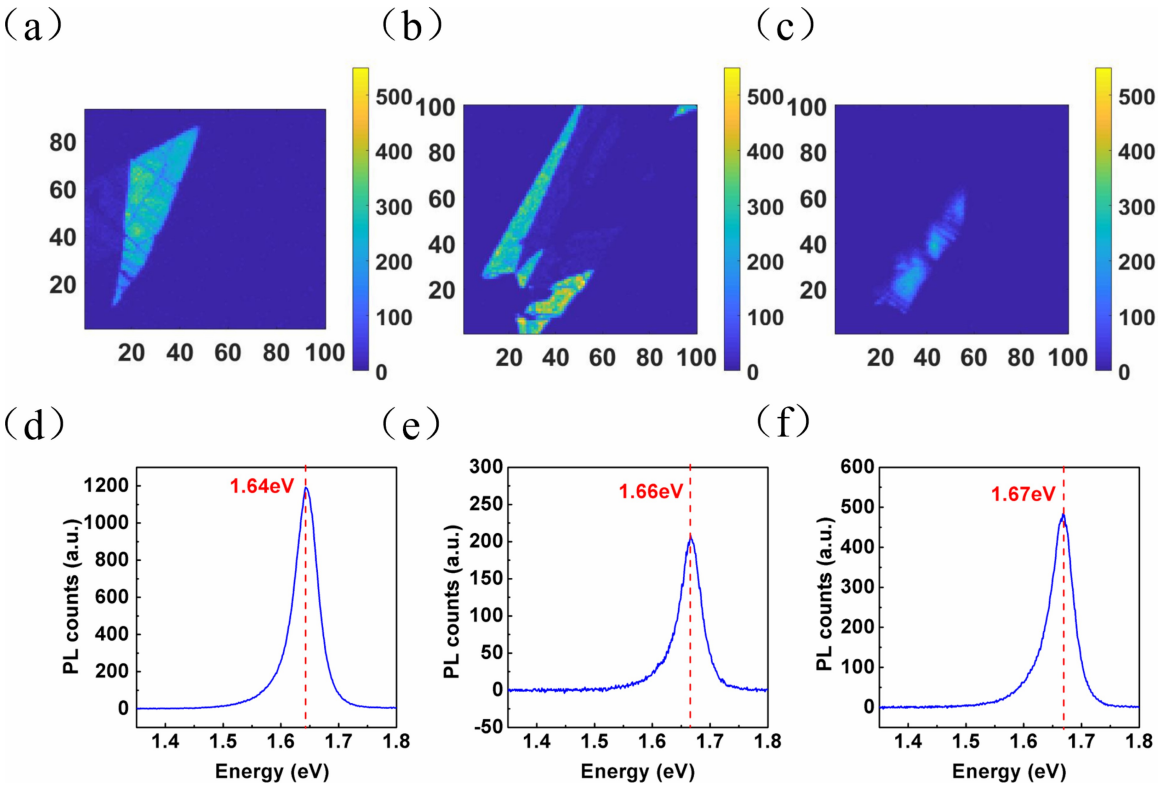

Figure 2.8: (a)-(c): PL scanning maps of several WSe_2 monolayer. Each image shows an area of $100\mu m \times 100\mu m$. (d)-(e): PL spectra of several WSe_2 monolayers. The peaks correspond to the A-exciton luminescence from WSe_2 and vary from 1.64 eV to 1.67 eV. Reprinted (adapted) with permission from Ref. 93. Copyright 2020 American Chemical Society.

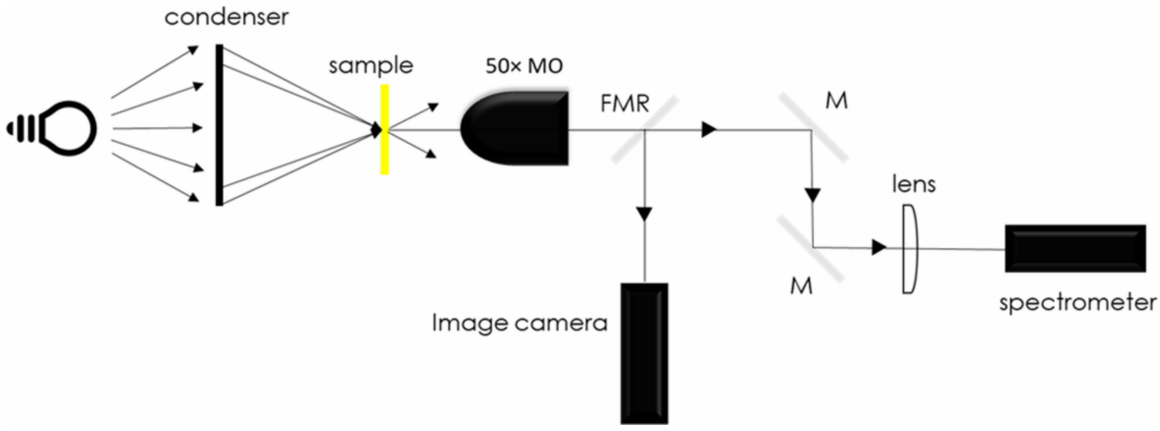

Figure 2.9: The setup schematic of dark-field scattering measurements. M: mirror; MO: microscope objective; FMR: flip-mirror reflector.

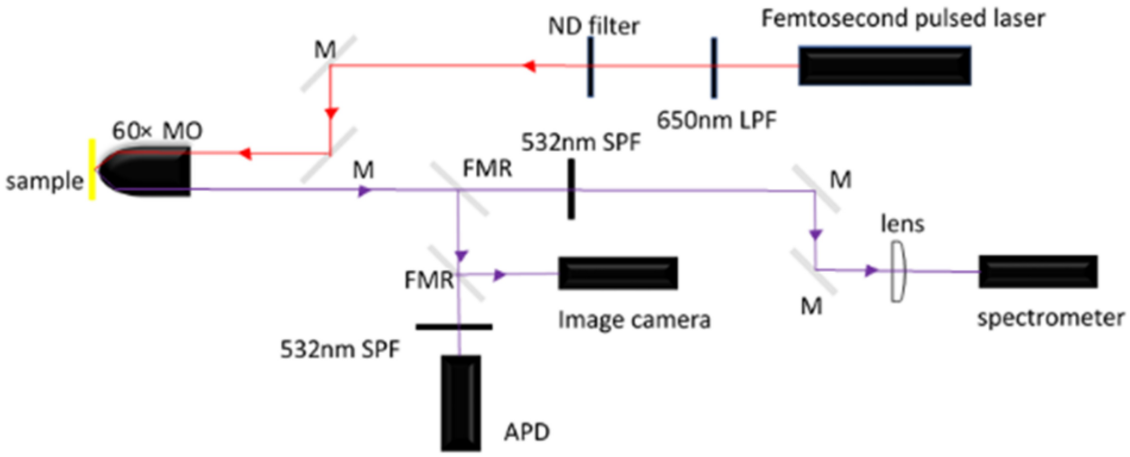

Figure 2.10: The setup schematic of SHG measurements. ND filter: neutral density filter; M: mirror; MO: microscope objective; FMR: flip-mirror reflector; LPF: long pass filter; APD: avalanche photodiode; SPF: short pass filter.

sion due to two-photon photoluminescence (TPPL)[106, 107], the raw SHG spectrum at each pump wavelength is fitted with a second order polynomial background and a sharp Gaussian peak, as shown in Fig. 2.11. The area under the Gaussian peak is taken to be the intensity of the SHG signal. The quadratic dependence of the SHG signal on the excitation power is verified experimentally. As illustrated in Fig. 2.12, the slope of the power-law fit is 2.03 ± 0.10, in agreement with the expected slope of 2 for SHG. To measure polarization-dependent SHG signals, we use a Berek compensator to rotate the linear polarization of the excitation beam while integrating the polarization of the emitted signal.

2.4 FDTD simulation

In collaboration with Prof. Maxim Sukharev[93], FDTD simulations are performed on both linear optical responses and SHG. The spatio-temporal dynamics of electromagnetic radiation are calculated using Maxwell's equations

$$\varepsilon_0 \frac{\partial \vec{E}}{\partial t} = \frac{1}{\mu_0} \nabla \times \vec{B} - \frac{\partial \vec{P}}{\partial t} \tag{2.35}$$

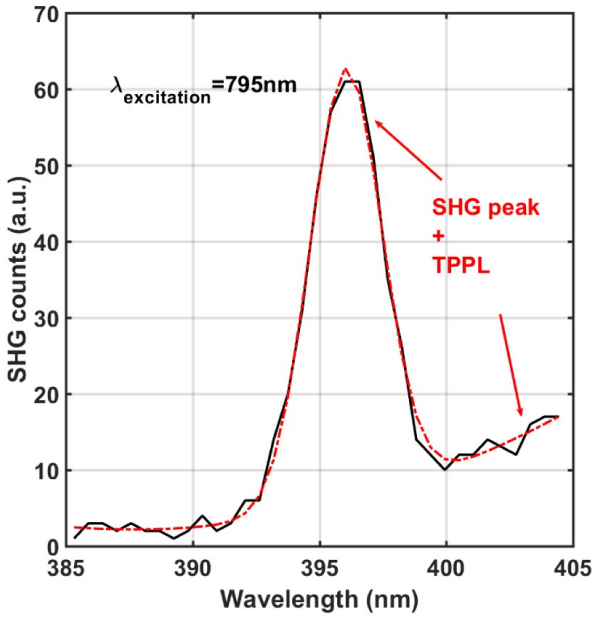

Figure 2.11: The black solid curve shows the raw second-harmonic signal from one nanorod-WSe_2 coupled system. The excitation wavelength is 795nm and the time-averaged excitation power is around 250 μW. The red dashed curve is a fit to a Gaussian peak representing the second-harmonic signal plus a quadratic background representing TPPL. The area under the Gaussian peak is taken to be the intensity of the second harmonic signal. Reprinted (adapted) with permission from Ref. 93. Copyright 2020 American Chemical Society.

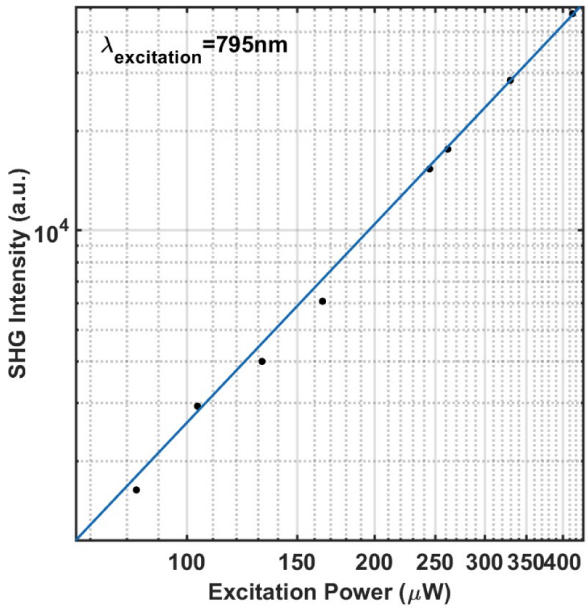

Figure 2.12: Excitation-power dependence of the second-harmonic intensity from gold nanorods coupled to a WSe_2 monolayer, and a power-law fit. The slope of the fit is 2.03 ± 0.10, in agreement with the expected slope of 2 for SHG. The excitation wavelength is 795 nm. The excitation power is measured immediately after the objective without the sample. Reprinted (adapted) with permission from Ref. 93. Copyright 2020 American Chemical Society.

$$\frac{\partial \vec{B}}{\partial t} = -\nabla \times \vec{E} \tag{2.36}$$

where the macroscopic polarization, $\vec{P}$, is evaluated using the nonlinear hydrodynamic model for the conduction electrons. This model is based on integration of equations for the electron velocity field, $\vec{u}$, and the electron number density, n_e

$$\frac{\partial \vec{u}}{\partial t} + (\vec{u} \cdot \nabla)\,\vec{u} + \gamma_e \vec{u} = \frac{e}{m_e^*}\left(\vec{E} + \vec{u} \times \vec{B}\right) \tag{2.37}$$

$$\frac{\partial n_e}{\partial t} + \nabla\,(n_e \vec{u}) = 0 \tag{2.38}$$

Here, m_e^* is the effective conduction electron mass and γ_e is a phenomenological decay constant. The current density, defined as

$$\vec{J} = \frac{\partial \vec{P}}{\partial t} = e n_e \vec{u} \tag{2.39}$$

couples Eq. 2.35, Eq. 2.36, Eq. 2.37 and Eq. 2.38. It is convenient to derive an equation for the polarization combining Eq. 2.37, Eq. 2.38 and Eq. 2.39[108]

$$\frac{\partial^2 \vec{P}}{\partial t^2} + \gamma_e \frac{\partial \vec{P}}{\partial t} = \frac{e}{m_e^*}(n_0 e \vec{E} + \frac{\partial \vec{P}}{\partial t} \times \vec{B} - \vec{E}(\nabla \cdot \vec{P})) - \frac{1}{n_0 e}((\nabla \cdot \frac{\partial \vec{P}}{\partial t})\frac{\partial \vec{P}}{\partial t} + (\frac{\partial \vec{P}}{\partial t} \cdot \nabla)\frac{\partial \vec{P}}{\partial t}) \tag{2.40}$$

The following parameters are used for gold: equilibrium number density $n_0 = 5.9 \times 1028 m^{-3}$, plasma frequency $\omega_p = 7.039eV$, and decay constant $\gamma_e = 0.181eV$. Eq. 2.40 reduces to the conventional Drude model for weak electric fields. The nonlinear terms seen on the right-hand side correspond to (1) the magnetic Lorentz force, (2) the quadrupole term coming from the continuity equation, and (3) the convection term. We note that each of these three terms contribute differently to SHG. The most significant contribution is obtained due to the convection term, especially at the boundaries

of plasmonic systems, while the term due to magnetic field is usually an order of magnitude smaller. Eq. 2.35, Eq. 2.36 and Eq. 2.40 are solved by numerical propagation in space and time using home-built FDTD codes. The electric and magnetic field components are computed at different positions on the Yee lattice. The components of the macroscopic polarization are calculated at the same spatial positions as the corresponding components of the electric field.

It is important to note that, in time-domain simulations of harmonic generation processes, one needs to propagate the equations of motion for a considerable amount of time to achieve numerical convergence of the power spectrum. We found that power spectra converge after a simulation time 500 fs if the system is driven by a 250 fs laser pulse with a peak amplitude of $2 \times 10^{-2} V/nm$. The angular distributions of the second harmonic signal are highly dependent on the duration of the pump pulse, converging only for pulses longer than 200 fs. Furthermore, the pump peak amplitude is chosen to ensure simulations are in the perturbative regime; i.e., the second-harmonic signal scales quadratically with the pump intensity.

The entire computational domain is divided into a number of sub-domains, each carried by a single processor. We implement send/receive operations using message passing interface (MPI) subroutines on all six faces of each sub-domain. This parallelization methodology, known as a three-dimensional domain decomposition, renders the codes highly scalable.[109] Numerical convergence is achieved for a spatial resolution of 1 nm with a time step of 1.7 as. All simulations are performed on the AFRL/DSRC HPC clusters Mustang and Onyx using 1584 processors. Typical execution times of our codes vary between 20 and 30 minutes for linear simulations and 70 and 90 minutes to obtain SHG results.

To incorporate the optical response of the WSe_2 monolayer into our numerical scheme, we adopt the Lorentz model with a frequency-independent second-order nonlinear susceptibility $\chi^{(2)}$. The value of $\chi^{(2)}$ is taken to be an adjustable parameter,

with typical values varying between 1 pm/V and 100 pm/V.[110] The numerical method that takes into account both linear dispersion and phenomenological nonlinear susceptibilities of different orders is adapted from Ref. 111.

The critical part in modeling of the experimental data is to ensure that the linear dispersion of WSe_2 is properly accounted for. It is well known that the environment influences the electronic structure of TMD materials rather significantly, which in turn may have a significant effect on their dielectric functions. When analyzing various dielectric functions for WSe_2 available in the literature, we used our experimental measurements as the main tool to identify the model most suitable for our work.

2.5 Results and Discussion

2.5.1 Linear Optical Characterization Results

Fig. 2.13(a) shows examples of dark-field scattering spectra from an isolated gold nanorod and from individual nanorods coupled to WSe_2 monolayers. The scattering spectra of the coupled systems show two peaks for various detunings, as expected for the strong-coupling regime. The SEM image of drop-casted nanorods is shown in Fig. 2.14(a). It should be noted that not all bright spots in dark field images, as shown in Fig. 2.14(b), are single nanorods. Dark-field scattering spectra are measured on hundreds of candidate single nanorods coupled to WSe_2 to exclude signals due to dimers, clusters, and dust. First, one can look at the dark-field-scattering images, and exclude spots that have apparent sizes larger than the diffraction limit, or whose scattering intensity is significantly higher than that obtained from single nanoparticles. In addition, one can look at the dark-field-scattering spectra, and exclude spectra that are very broad or that contain more than two peaks. Besides the scattering spectra shown in Fig. 2.13(a), several additional spectra of single nanorods and coupled systems are shown in Fig. 2.15.

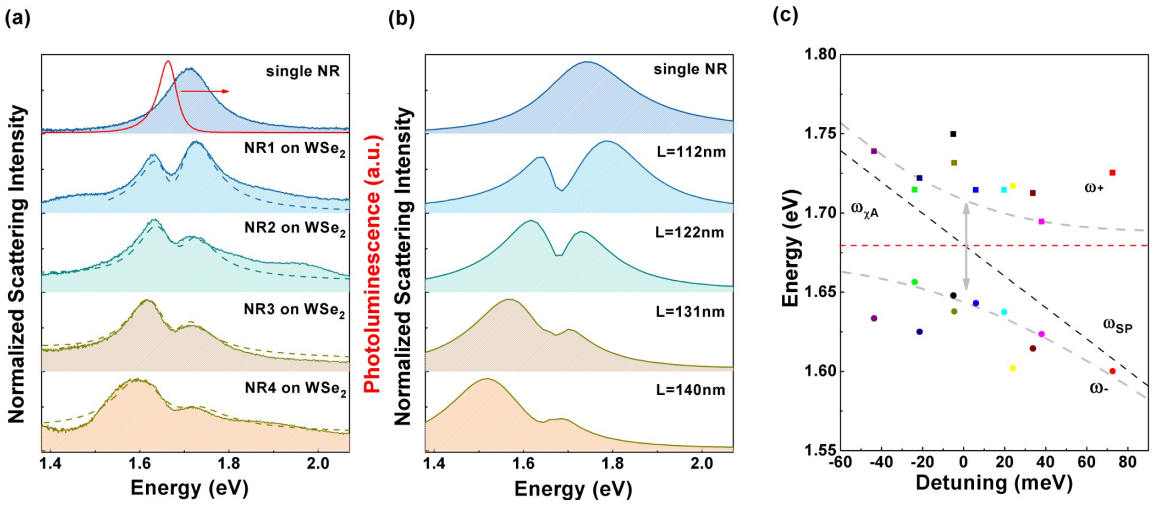

Figure 2.13: (a) Measured PL spectrum of a monolayer of WSe_2 (red, top panel), and measured dark-field-scattering spectra of an isolated gold nanorod (top panel) and of single nanorods coupled to the same WSe_2 monolayer (bottom panels). Dashed lines are fits using the linear two-oscillator model. (b) Calculated dark-field scattering spectra of an isolated gold nanorod (top panel, length is 112 nm and diameter is 40 nm) and of nanorods with different lengths coupled to a WSe_2 monolayer (bottom panels). (c) Frequencies of upper polaritons (solid squares) and lower polaritons (solid circles) extracted from fits to experimental data. Points with the same colors correspond to frequencies from the same scattering spectra. Gray lines are fitting results using the two-oscillator model, showing the anti-crossing behavior characteristic of strong coupling. Reprinted (adapted) with permission from Ref. 93. Copyright 2020 American Chemical Society.

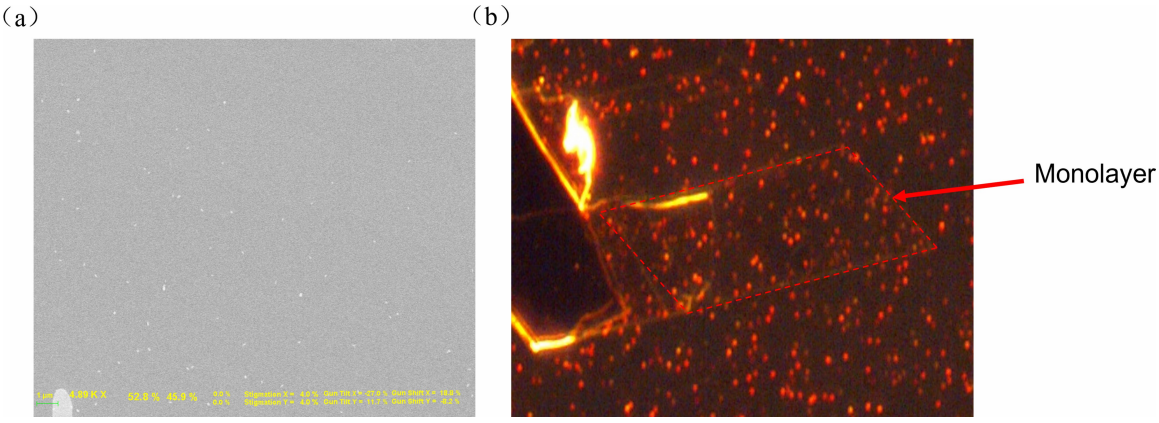

Figure 2.14: (a) A SEM image of drop-casted nanorods on glass substrates. (b) A dark field image of gold nanorods dispersed on the WSe_2 flake. The red dashed lines remark the monolayer area.

The TMD monolayers are identified by raster scanning the sample and detecting the PL signal in a confocal configuration at room temperature. The PL intensity is highly sensitive to the number of TMD layers, and only monolayers feature a direct bandgap and strong emission[105, 112, 113]; an example of PL from a WSe_2 monolayer is shown in Fig. 2.13(a). A pronounced peak around 1.66 eV is clearly observed, corresponding to emission from A excitons.

To unambiguously attribute the scattering spectral peaks to exciton-plasmon polaritons, Au nanorods of different lengths, and thus different longitudinal plasmon frequencies, are investigated numerically. FDTD simulations of the coupled systems' scattering spectra give results very similar to the experimental data, as illustrated in Fig. 2.13(b). Fig. 2.16 compares linear spectra calculated using experimental parameters for WSe_2 from Ref. 114. and from Ref. 87. The scattering intensity obtained using the dielectric function of WSe_2 from Ref. 114 exhibits noticeable splitting reaching 133 meV for a 112nm-long nanorod. Interestingly, the collective exciton mode is also observed for 122 nm and 131 nm nanorods as a third narrow spike at 1.74 eV. The physical nature of the third mode has been extensively discussed in the literature both theoretically and experimentally.[115, 116, 117] In our experiments, however, this feature has not been observed. By comparison, simulations based on the single Lorentz oscillator model with phenomenological parameters from Ref. 87 result in a Rabi splitting of 150 meV. Calculated widths of each polaritonic state closely match those seen in our experiments. Additionally, we performed fitting of the coupled oscillator model with experimental data and found that the closest match between simulations and experiments was obtained using parameters from Ref. 87. We therefore use these parameters for all the calculations results in Fig. 2.13(b).

The linear scattering spectra can also be fit to the linear two-oscillator model. Dashed curves in Fig. 2.13(a) shows sample fits of the experimental data to Eq. 2.26 and Eq. 2.27. In these fits, γ_{pl} and ω_{pl} are constrained to be within the range measured

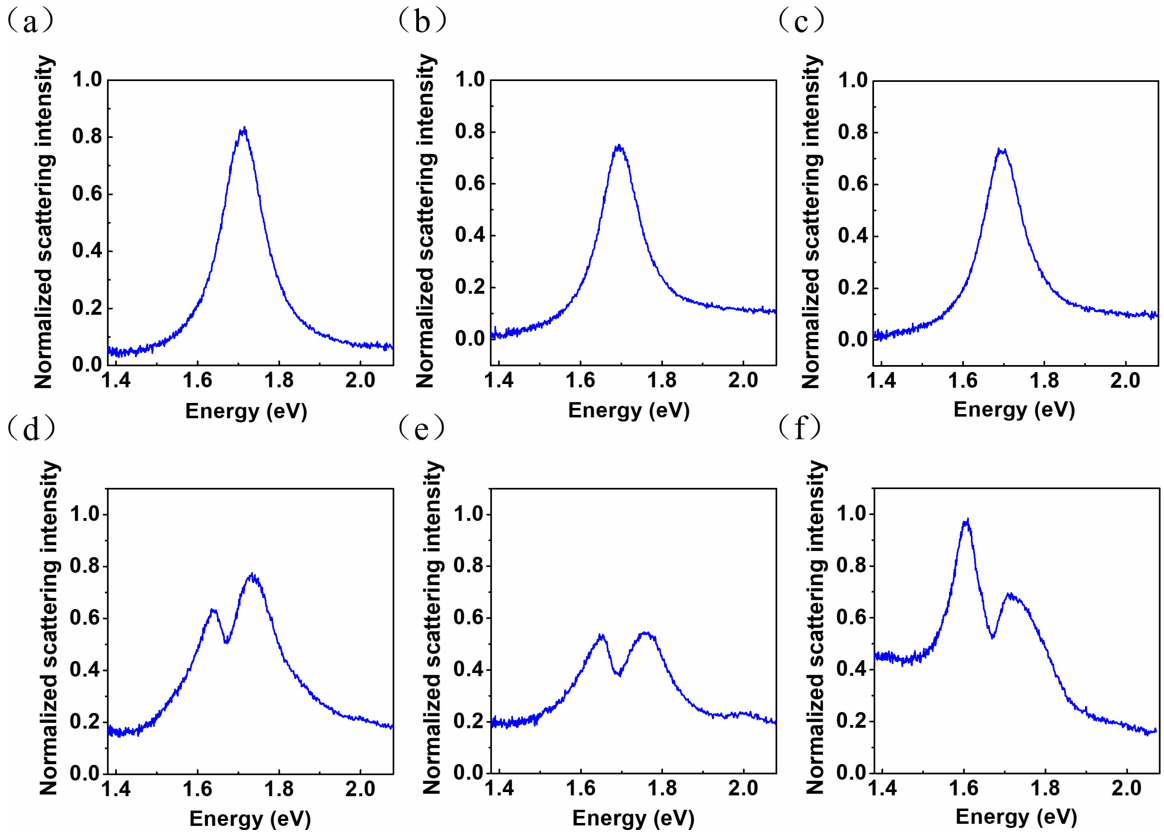

Figure 2.15: (a)-(c) Dark-field scattering spectra for single nanorods. (d)-(f) Dark-field scattering spectra for several nanorods coupled to a WSe_2 monolayer. Reprinted (adapted) with permission from Ref. 93. Copyright 2020 American Chemical Society.

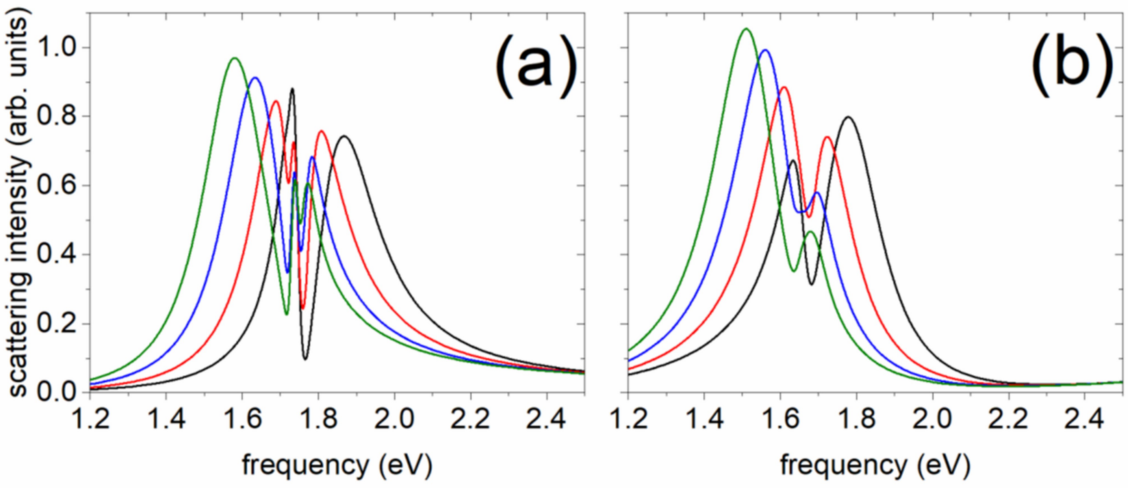

Figure 2.16: Scattering intensity as a function of the incident photon energy calculated for gold nanorods on top of a WSe_2 monolayer. The lengths of the rods are 112 nm (black), 122 nm (red), 131 nm (blue), and 140 nm (green). The diameter of all nanorods is 40 nm and the distance between the nanorods and WSe_2 is 5 nm. The system is excited by a pulse polarized along the nanorod's long axis. Panel (a) shows results using the dielectric function for WSe_2 from Ref. 114. Panel (b) shows results approximating the dielectric function of WSe_2 as a single Lorentz oscillator with parameters from Ref. 87. Reprinted (adapted) with permission from Ref. 93. Copyright 2020 American Chemical Society.

for scattering from gold nanorods uncoupled to WSe_2, and γ_{ex} and ω_{ex} are constrained to be near the values obtained from the PL spectrum of the bare WSe_2 layer; the only free parameters in the fits are thus the coupling strength g and an arbitrary overall scaling factor. From the fitted parameters, the real frequencies of the coupled plasmon-exciton modes can be calculated according to[47]

$$\omega_{\pm} = \frac{1}{2}\left(\omega_{pl} + \omega_{ex}\right) \pm \sqrt{g^2 + \frac{1}{4}\left(\omega_{pl} - \omega_{ex}\right)^2} \tag{2.41}$$

In Fig. 2.13(c), we plot $\omega_{\pm}$ as functions of the detuning $\delta = \omega_{ex} - \omega_{pl}$, demonstrating the characteristic anti-crossing behavior. From this plot, we obtain an average coupling strength $g = 80 \pm 13meV$. Comparing to the fitted ranges of plasmon line width $\gamma_{pl} = 105 - 150meV$ and the exciton line width $\gamma_{ex} \approx 70meV$, we can see that the coupled plasmon-WSe_2 system meets the strong-coupling criterion in Eq. 2.14.

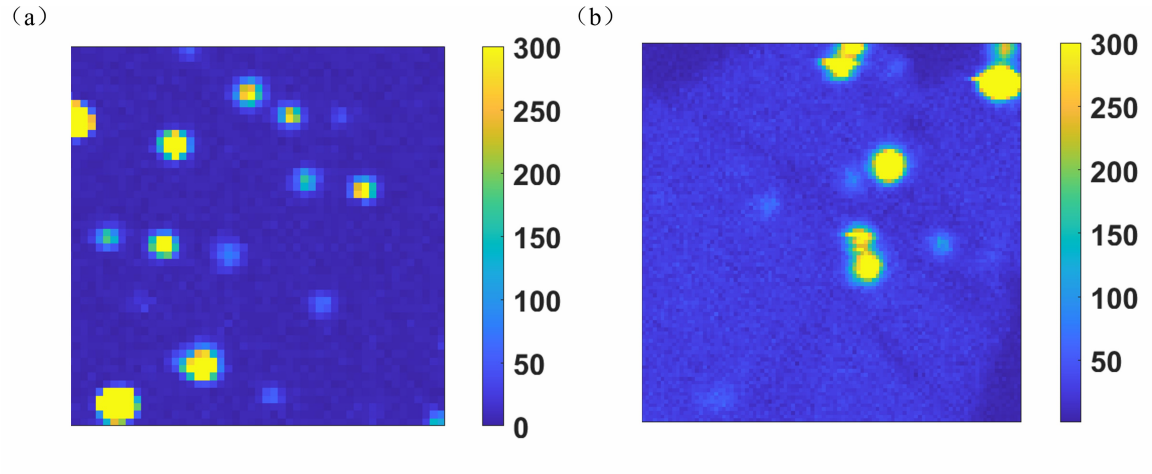

Figure 2.17: SHG scanning maps of (a) uncoupled gold nanorods and (b) nanorods coupled to a monolayer WSe_2. Each image shows an area of $10\mu m \times 10\mu m$. The pump laser wavelength is 750 nm.

2.5.2 SHG Characterization Results

We now turn our attention to the nonlinear properties of the sample by performing SHG measurements in a confocal configuration. We first do raster scanning over the sample with a pump laser at 750 nm and collect the SHG signals (with TPPL accompanied) in the APD. The maps of uncoupled gold nanorods and coupled systems are shown in Fig. 2.17(a) and Fig. 2.17(b), respectively. After determining the positions of nanorods, The spectral dependence of the integrated SHG signal as a function of excitation wavelength is measured for a single nanorod, as shown in Fig. 2.18(a), and two representative coupled systems, as shown in Fig. 2.18(b). The SHG spectrum of the single nanorod shows a clear peak which corresponds to the plasmonic mode. While the SHG spectra for the strong coupling systems exhibit two distinct peaks, which match well with the positions of the peaks in the linear scattering spectra (Fig. 2.18(a), shaded areas). This indicates that the emitted second harmonic has its origins in the coupled system, rather than in either the gold nanorod or the WSe_2 separately.

The experimental SHG signals are fit with the nonlinear two-oscillator model.

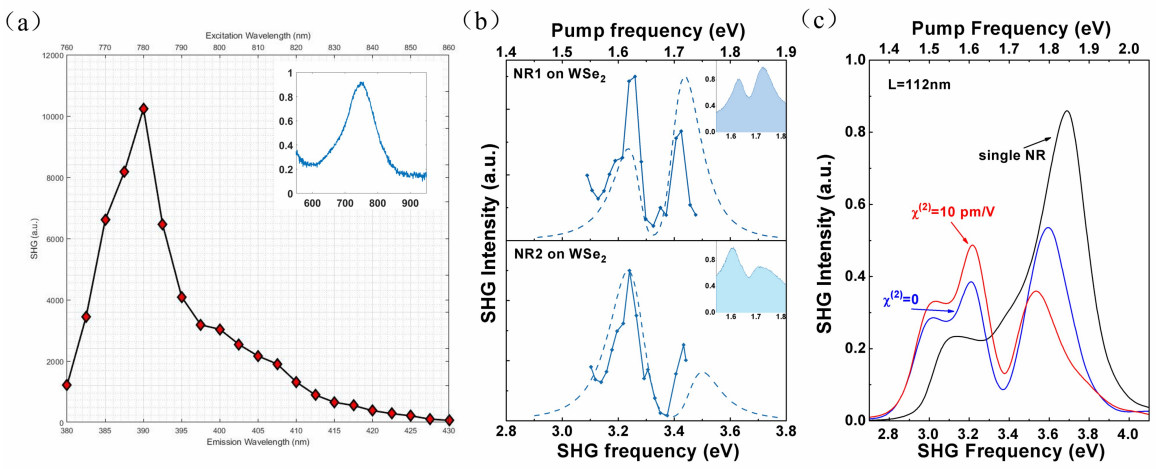

Figure 2.18: (a) SHG signals measured on a single gold nanorod. The corresponding linear scattering spectrum is shown in the inset. (b) Second-harmonic signals measured at different pump frequencies for single gold nanorods on a WSe_2 monolayer (solid lines). The corresponding linear scattering spectra are shown in the insets. Dashed lines show fitting results using the nonlinear two-oscillator model. (c) Calculated second-harmonic spectra for a single nanorod (length is 112 nm, black) and the nanorod-WSe_2 coupled system using $\chi^{(2)} = 0$ (blue) and $\chi^{(2)} = 10pm/V$ (red) for WSe_2. Panel (b) and (c) are reprinted (adapted) with permission from Ref. 93. Copyright 2020 American Chemical Society.

All the parameters in the fit to a given SHG sepctrum are constrained by the fit to the corresponding linear spectrum, and the only free parameter is an arbitrary overall scaling factor. In practice, we account for possible calibration errors in the measurement of the SHG spectrum by including an offset and scaling factor for the frequency axis in the fit.

Fit results are shown in Fig. 2.18(a). The coupled-nonlinear oscillator model shows good qualitative agreement with the measured SHG spectra. Quantitative differences are most likely due to errors in measuring SHG intensity at the edge of the spectral range of the detector used experimentally. To confirm the validity of this simple physical picture, we also compare experimental SHG spectra to those obtained by numerically solving the nonperturbative fully vectoral hydrodynamic model coupled to Maxwell's equations.[104] Calculation results are shown in Fig. 2.18(b) and clearly reproduce the observed spectral splitting. We also use these simulations to compare

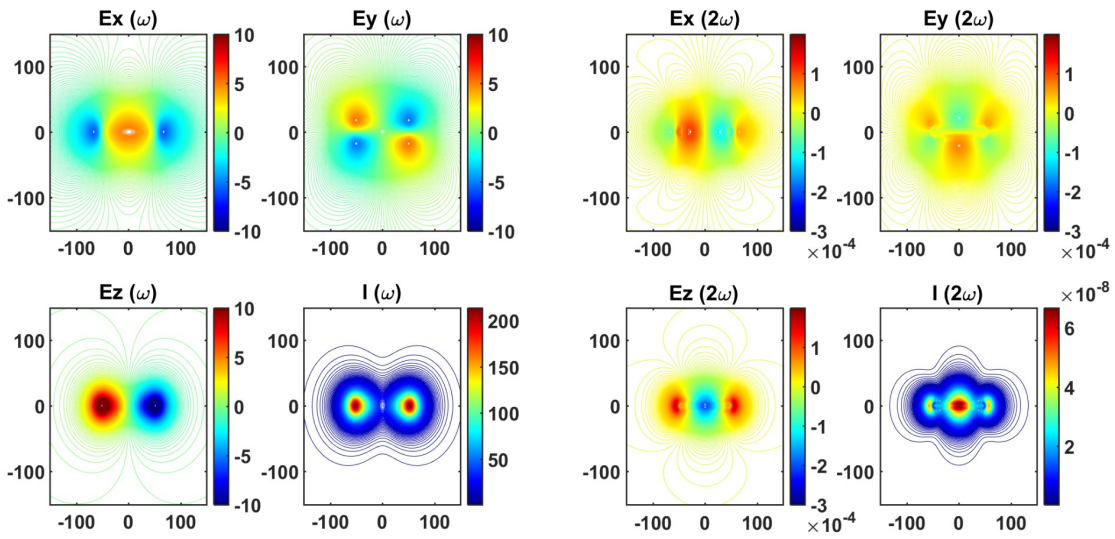

Figure 2.19: Local second-harmonic and fundamental field distributions and intensity distributions for the coupled nanorod-WSe2 system. Headings on each panel indicate either a particular component of the electric field, $E_{x,y,z}$, and the intensity, I. The x direction is along the long-axis of the nanorod, and the z direction is normal to the substrate. The left four panels show the local field (in the units of enhancement) calculated at the longitudinal SPP frequency (1.83 eV), normalized by the magnitude of the incident field (or similarly for intensity). The right four panels show the electric field components evaluated at the second harmonic and normalized to the peak amplitude of the pump. All fields are calculated 10 nm above the surface of the nanorod. The nanorod's length is 112 nm and the incident field is polarized along the x direction. Reprinted (adapted) with permission from Ref. 93. Copyright 2020 American Chemical Society.

SHG from the coupled system when we include a realistic nonlinear coefficient for the WSe_2 monolayer, and when we neglect the nonlinearity of this material. The differences in the SHG excitation spectra are small, demonstrating that the SHG arises primarily from the surface nonlinearity of the gold nanoparticle, and justifying our neglect of the second term in Eq. 2.34. Moreover, the splitting in the SHG spectrum is unaffected by the source of the nonlinearity, showing that the emitted second harmonic arises from the polaritons and not from the plasmons or excitons separately.

Including the second-order nonlinearity of WSe_2 in the simulations noticeably

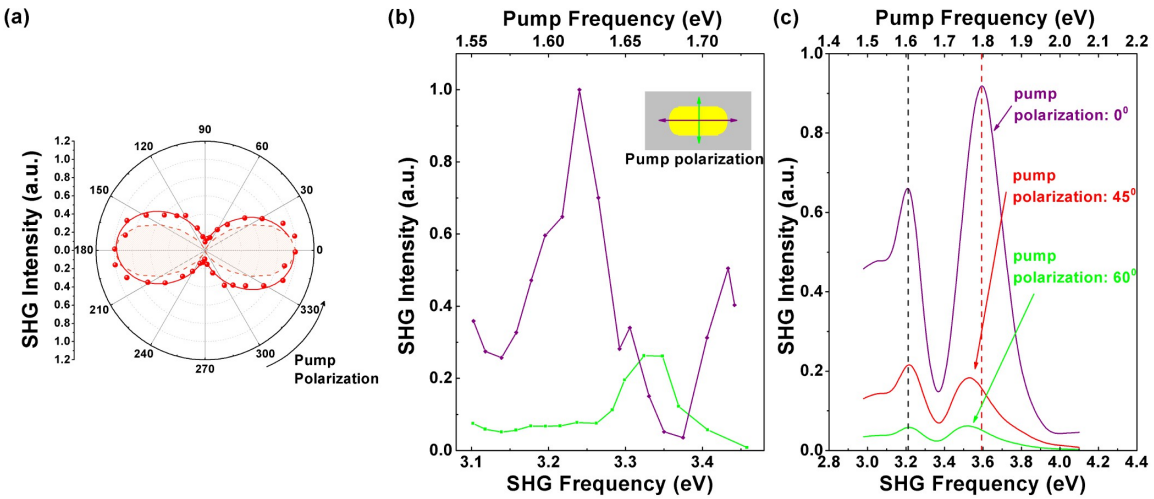

Figure 2.20: (a) Measured pump-polarization-dependent second-harmonic radiation pattern from the nanorod-WSe_2 coupled system (red dots) and a dipolar emission fit (solid red line). The numerical calculation results under the same condition are also shown (orange dashed line and filled area). (b) Measured second-harmonic spectra for the nanorod-WSe_2 system when pumping longitudinally (violet) and transversely (green) relative to the long axis of the nanorod. (c) Calculated second-harmonic spectra of a nanorod (length is 112 nm) strongly coupled to WSe_2 when pumping with different polarization angles relative to the long axis of the nanorod. Reprinted (adapted) with permission from Ref. 93. Copyright 2020 American Chemical Society.

reduces the separation between the peaks in the SHG spectrum. This is in agreement with the nonlinear two-oscillator model, which predicts a smaller splitting in the SHG spectrum due to the exciton dipole (Eq. 2.33) than in the SHG spectrum due to the plasmon dipole (Eq. 2.32). Since the total spectrum is a weighted sum of the exciton and plasmon spectra, increasing the fraction of SHG emitted by the exciton will reduce the overall peak separation. All of the calculated SHG spectra show an additional broad peak near 1.6 eV. Part of this peak can also be seen in the experimental spectra, near the edge of the experimentally accessible frequency range. This peak is attributed to local field enhancement at the tips of the rod. The field distribution maps of this strong coupling system is shown in Fig. 2.19.

Finally, we discuss the polarization dependence of the SHG spectra. The experimentally measured radiation pattern for a representative strongly coupled system is shown in Fig. 2.20 along with results of the corresponding numerical calculation.

A dipolar SHG emission pattern is observed, corresponding to the longitudinal plasmonic mode radiation.[118] The fact that the dipolar emission pattern arises from the longitudinal plasmon can be seen from the following argument. The horizontal component of the second order macroscopic polarization can be written as

$$P_x^{(2)}(2\omega) \sim \chi_{xxx}^{(2)} cos^2(\theta) + \chi_{xyy}^{(2)} sin^2(\theta) \tag{2.42}$$

where χ_{ijk}^2 is the second order susceptibility tensor and θ is the in-plane polarization of the pump. It is clear from Fig. 2.20(a) that the SHG signal has a dominant horizontal component, indicating that $\chi_{xxx}^{(2)} >> \chi_{yyy}^{(2)}$.

In Fig. 2.20(b), we show SHG spectra recorded for longitudinal and transverse polarization of the pump beam. It can be clearly seen that a longitudinally polarized pump excites the polaritonic states due to coupling between the longitudinal plasmon and the WSe_2 excitons. Meanwhile, the transverse pump produces a signal only at the exciton peak, the intensity of which is 4 times smaller than that of the polariton peaks. Similar trends are seen for the numerical simulations, as shown in Fig. 2.20(c). Specifically, maximum splitting in the SHG excitation spectrum is seen when the pump polarization is aligned along the long axis of the nanorod. Rotating away from this orientation decreases the splitting in the SHG spectrum; the upper polariton peak is more affected than the lower polariton peak, because the nonzero detuning between the plasmon and exciton means that the two polariton branches have unequal plasmonic character.

2.5.3 More Discussion on SHG

Fig. 2.21 shows normalized power spectra calculated for a single nanorod pumped on and off its longitudinal plasmon resonance. We note that, due to computational constraints, we limit the size of WSe_2 to a two-dimensional sheet with dimensions

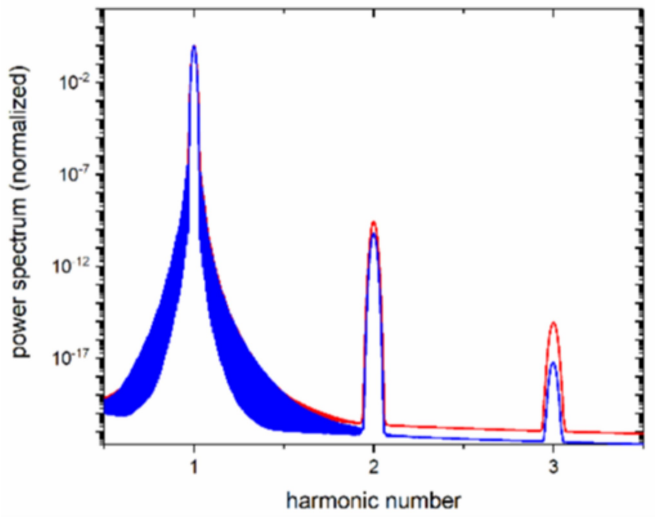

Figure 2.21: Normalized power spectrum as a function of harmonic number calculated for a single 112-nm-long gold nanorod pumped at its longitudinal plasmon resonance (1.83 eV, red) and off the plasmon resonance (2.00 eV, blue). The pump is polarized along the nanorod's long axis and is 250 fs long. Total propagation time of the calculations is 500 fs. Reprinted (adapted) with permission from Ref. 93. Copyright 2020 American Chemical Society.

500 nm by 500 nm. By comparison, in actual experiments, the dimensions of WSe_2 flakes are orders of magnitude greater than those of a single nanorod. Simulations carried out for slightly larger or smaller dimensions result in nearly identical data in the linear regime. However, nonlinear simulations are sensitive to the size of WSe_2.

To illustrate this, Fig. 2.22 shows the calculated SHG signal as a function of pump frequency for a stand-alone WSe_2 monolayer, for a stand-along gold nanorod, and for a WSe_2 monolayer coupled to a gold nanorod. The SHG spectrum from the WSe_2 monolayer alone has a peak near 1.7 eV, which results from direct-band-gap exciton. Additionally, the signal gradually increases with decreasing pump frequency. We ran several tests varying the size of WSe_2 to examine how it may affect SHG. The smaller the size of WSe_2 was, the steeper the low-frequency SHG response we obtained. The knee structure of the SHG signal for a single nanorod seen near 1.6 eV (dot-dashed line in Fig. 2.22) is attributed to the contribution of the local field enhancement at the tips of the rod. With the nanorod strongly coupled to a finite WSe_2 flake, the

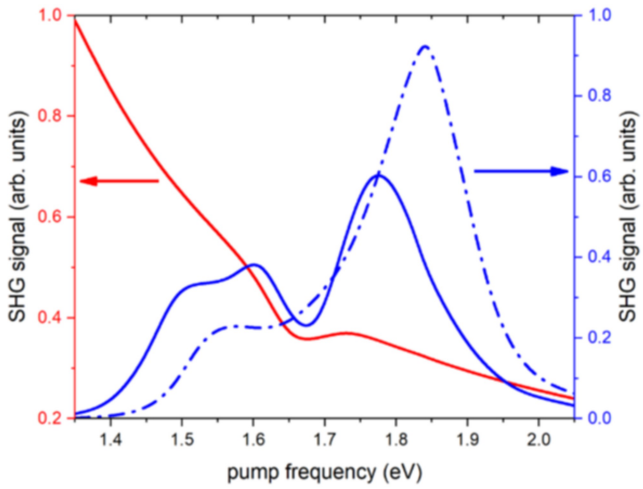

Figure 2.22: Second-harmonic signal as a function of the pump frequency. The red line (left vertical axis) shows the signal calculated for a stand-alone monolayer of WSe_2. The dot-dashed blue line (right vertical axis) shows signal for an isolated 112-nm-long nanorod. The solid blue line (right vertical axis) shows signal for the nanorod coupled to the WSe_2 monolayer. The nonlinear second-order susceptibility for WSe_2 is taken to be $10pm/V$. Reprinted (adapted) with permission from Ref. 93. Copyright 2020 American Chemical Society.

knee in the SHG response is pushed to lower pump frequencies.

Fig. 2.23 shows additional SHG spectra measured on individual gold nanorods coupled to WSe_2 monolayers. From these data it can be inferred that detuning between the plasmon exciton and the WSe_2 exciton shifts the maxima of the SHG excitation spectra. The frequencies of the second harmonic peaks can be estimated by equating the denominator of Eq. 2.32 to 0 and neglecting all damping terms, giving

$$\omega_{\pm} = \sqrt{\frac{1}{2}\left({\omega_{pl}}^2 + {\omega_{ex}}^2\right) \pm \sqrt{g^2\omega_{ex}\omega_{pl} + \frac{1}{4}\left({\omega_{pl}}^2 - {\omega_{ex}}^2\right)^2}} \tag{2.43}$$

It should be noted that by equating the denominator of Eq. 2.27 to 0 and omitting all damping terms, we get the same equation. This means that, in the absence of damping, the maxima of linear and nonlinear spectra are at the same frequencies, and thus have the same dependence on detuning.

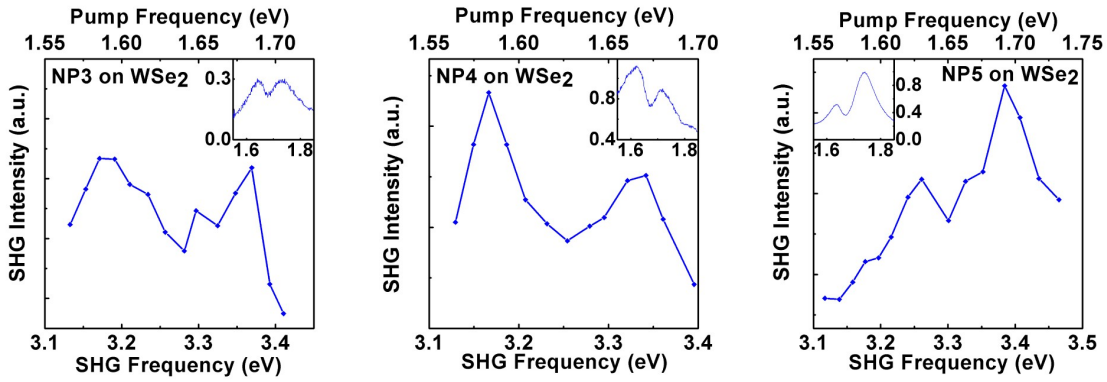

Figure 2.23: Pump-dependent second-harmonic spectra for several individual gold nanorods strongly coupled to a monolayer of WSe_2. The insets show the corresponding dark-field scattering spectra. Reprinted (adapted) with permission from Ref. 93. Copyright 2020 American Chemical Society.

2.5.4 More Discussion on THG

As seen from Fig. 2.21, the pump also leads to significant THG. Although we did not study THG experimentally, it is worth exploring numerically. Fig. 2.24 shows THG results calculated for a stand-alone nanorod and for a nanorod coupled to linear WSe_2 (i.e., we did not include the third order susceptibility of WSe_2 in our simulations). The results demonstrate that, even though WSe_2 is modeled as a linear Lorentz oscillator, THG is significantly altered due to strong coupling with the longitudinal plasmon of the nanorod. We note that third harmonics of the upper and lower polaritonic states are clearly visible. Interestingly, the maximum in the third-harmonic signal due to both polaritons is blue shifted with respect to the linear frequencies, with the blue shift of the upper polariton being greater than that of the lower polariton.

2.6 Conclusions

In conclusion, we report the experimental observation of Rabi splitting in the pump-frequency-dependent SHG signals from a strongly coupled system consisting of a

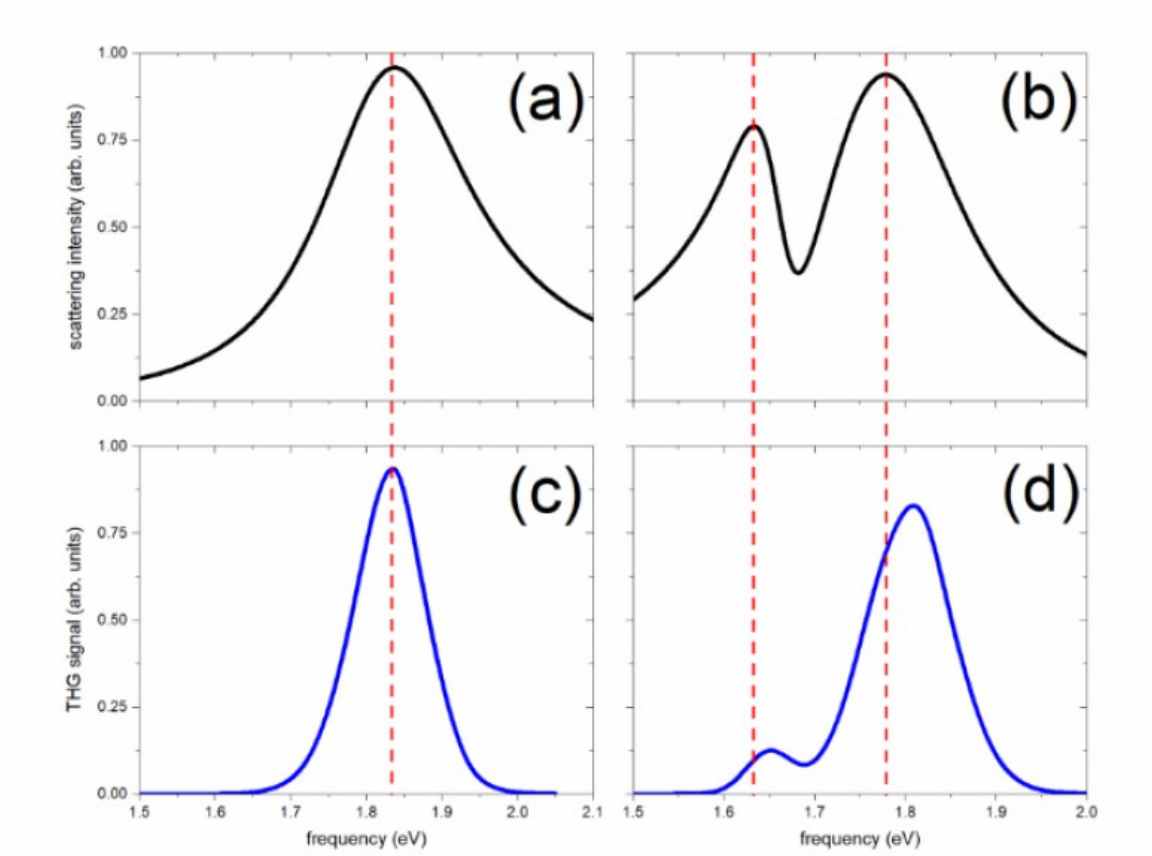

Figure 2.24: Panels (a) and (b) show linear scattering intensity as a function of frequency calculated for a single 112-nm-long nanorod (a) and for the nanorod on top of WSe_2 (b). Panels (c) and (d) show corresponding third-harmonic signals as functions of the pump frequency. Vertical red dashed lines indicate frequencies of the plasmon mode ((a) and (c)) and lower and upper polaritons ((b) and (d)). Reprinted (adapted) with permission from Ref. 93. Copyright 2020 American Chemical Society.

gold nanorod and a monolayer of WSe_2. As described by FDTD simulations based on the nonperturbative hydrodynamic-Maxwell model, these polaritons reshape the SHG response of the system by creating local field enhancement at the polariton frequencies. The theory and simulations can be described using a simple, analytical model of two coupled nonlinear classical oscillators. Future work will be dedicated to extending the studies to nonlinear-optical effects beyond SHG, such as wave mixing, nonlinear polariton-polariton interactions and nonlinear extinction, and to plasmonic and excitonic systems with more complex symmetry properties. This in turn will pave the way for devices such as integrated entangled photon sources, room temperature quantum repeaters, and wave mixing elements.

Chapter 3

Invertible Nonlinearities of ITO Thin Films

3.1 ENZ Materials

The pursuit of achieving the large optical nonlinearity with a moderate optical field has been a long-time goal in the study of light-matter interactions. At the bottom of many approaches that could significantly enhance this nonlinearity, a key guiding ideology is seeking materials whose refractive index can be drastically modified by the optical pump.[31, 119] Among all such materials, epsilon-near-zero (ENZ) materials have attracted much attention due to their intriguing optical properties, such as diverging velocities[120, 121], wavelength expansion[122] and the large field enhancement.[123, 124, 125] ENZ materials have been shown to produce a host of fascinating and sometimes mind-bending optical effects, such as photon tunnelling[126], super-coupling[127] and control of emission.[128] More recent experiments have revealed the great potential of ENZ materials in nonlinear applications.[129] An intuitive calculation shows that the change of refractive index can be expressed as $dn = d\epsilon/2\sqrt{\epsilon}$, which becomes significant given a near-zero permittivity.

The ENZ condition, or more general near-zero-index (NZI) condition, has been realized in many material platforms. Homogeneous materials include metals[130, 131], doped semiconductors[132, 123] and phononic materials.[133, 134] Many structured materials, such as metamaterials[135], waveguides near the cut-off frequency[121], resonant cavities[136] and photonic crystals[137], are also proved to be eligible for the ENZ condition. Transparent conductive oxides (TCO) have emerged as new platforms for studying ENZ related phenomena, especially for enhancing optical nonlinearities.[132, 138, 139, 140]

In this section, some featured properties of ENZ materials will be introduced. Then some material platforms for realizing the ENZ condition will be briefly mentioned, with the emphasis being put on TCO thin films.

3.1.1 Properties of ENZ Materials

Diverging velocities are a central feature of ENZ materials. Considering the propagation of a plane wave in an ENZ material, the phase velocity is

$$v_p(\omega) = \frac{\omega}{k} = \frac{c}{\sqrt{\epsilon(\omega)}} \tag{3.1}$$

which tends to diverge if $\epsilon(\omega)$ goes to zero at a certain wavelength. On the other hand, the group velocity is

$$v_g(\omega) = \frac{d\omega}{dk} = \frac{c\sqrt{\epsilon(\omega)}}{\epsilon(\omega) + \frac{\omega}{2}\frac{d\epsilon(\omega)}{d\omega}} \tag{3.2}$$

which tends to zero, because the slope of the permittivity is finite. The diverging velocities produce nearly uniform phase across the ENZ material. As a consequence, as shown in Fig. 3.1(a), the wavefront of the transmitted light is defined by the shape of the exit facet.[120] The diverging velocities have been explored across a wide range of optical applications, including sensors[141], cloaking and transformation optical

devices[142, 143], near-perfect optical absorbers[144], optical memories[145], systems with enhanced quantum interactions[120] and nonlinear interactions[132, 123].

Substantial wavelength expansion is a natural consequence of the diverging phase velocities. The wavelength in ENZ materials is

$$\lambda_{ENZ} = \lambda_0/n \tag{3.3}$$

which increases drastically when n approaches zero. Fig. 3.1(b) shows the interference pattern with a diverging beat length that was observed in a corrugated waveguide under the ENZ condition.[122] This phenomenon indicates an almost uniform phase over a large propagating distance, which is potentially useful in achieving phase-matching-free nonlinear optical devices[146], super-coupling[127] and antenna resonance pinning.[147, 148]

Another feature that occurs in ENZ materials is the great field enhancement due to the Maxwell's boundary condition

$$\epsilon_1 E_1^{\perp} = \epsilon_2 E_2^{\perp} \tag{3.4}$$

where ϵ_1, ϵ_2 are the permittivity of the ENZ material and its neighbouring layer, $E_1^{\perp}$ and $E_2^{\perp}$ are the corresponding normal components of the electric field across the boundary. This results in the enhancement of $E_1^{\perp}$ by a factor of ϵ_2/ϵ_1. Because $\epsilon_1 \to 0$, the electric field is effectively confined inside the ENZ layer. Fig. 3.1(c) shows an example of the sharply increased field intensity in a layer of ENZ material cadmium oxides (CdO) that wrapped the silicon waveguide.[149] The field enhancement is widely utilized in strongly coupled systems to enable extreme nonlinear optics.

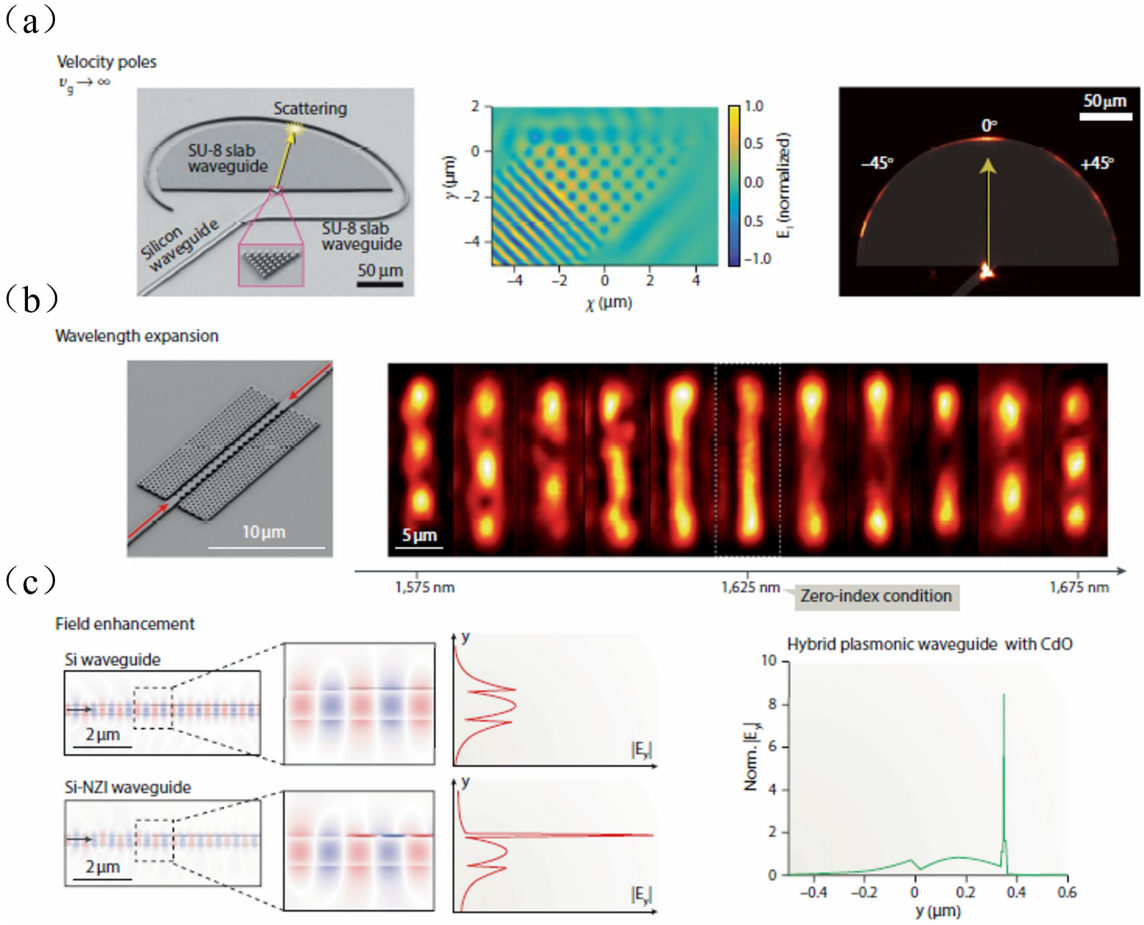

Figure 3.1: Characteristic properties of ENZ materials. (a) SEM image (left) of an on-chip ENZ prism placed at the end of a silicon waveguide with an SU-8 slab guiding region and a circular scattering element. The phase velocity of the excitation light tends to infinity and a nearly uniform phase is achieved within the prism, as shown by the simulated interference pattern (center), which results in emission leaving in the direction normal to the interface instead of at an arbitrary angle (right). (b) The wavelength expands in a corrugated waveguide (left) under the ENZ condition. The beat length of the interference pattern (right) extends greatly as the excitation wavelength approaches the ENZ region. (c) Field enhancement of the normal component of the electric field in near- zero-index (NZI) materials. For a wave propagating in a silicon waveguide, when a NZI layer is placed on top of the waveguide, a strong field confinement is observed. Reprinted (adapted) with permission from Ref. 31. Copyright 2019 Springer Nature.

3.1.2 TCO thin films

Transparent conductive oxides (TCOs), a subset of ENZ materials, have emerged as new platforms for enhancing optical nonlinearities.[132, 138, 139, 140] Typical examples that have already been widely investigated include Al doped zinc oxides (AZO)[132, 150], CdOs[151, 152] and Indium tin oxides (ITOs).[153, 154] These materials support ENZ resonances in the NIR range and are compatible with the existing complementary metal-oxide semiconductor (CMOS) technologies[155, 156], thus promise great applications in integrated telecom industries.[157] Moreover, the stability of these materials is better than traditional metals[158] and highly-doped semiconductors[159] that show near-zero ϵ in their bulk plasma wavelengths, and therefore can endure a larger optical pump field to get larger nonlinearities without reaching the damage threshold. A rich design space for photon manipulation in these materials also allows different strategies being employed to further enhance the nonlinearity, including patterned structures[160, 161], combining with plasmonic materials[153, 162, 163, 127] and bringing in waveguide modes.[164]

It should be noted that bulk TCOs also support propagating surface plasmon modes due to the Drude dispersion in the ENZ region. This mode is called the Berreman mode[165, 141] and is different from the ENZ mode that is localized in thin films. The dispersion relations of these two modes are shown in Fig. 3.2.[129] Like other confined modes, the ENZ mode is only accessible with an extrinsic coupling mechanism and the mode frequency is nearly unchanged with the coupled wave vector of the incident light.

3.2 Nonlinear Optical Effects

Nonlinear optical effects in ENZ materials have gained wide interest in recent studies. Some featured results are listed in Fig. 3.3. One of the most fundamental nonlin-

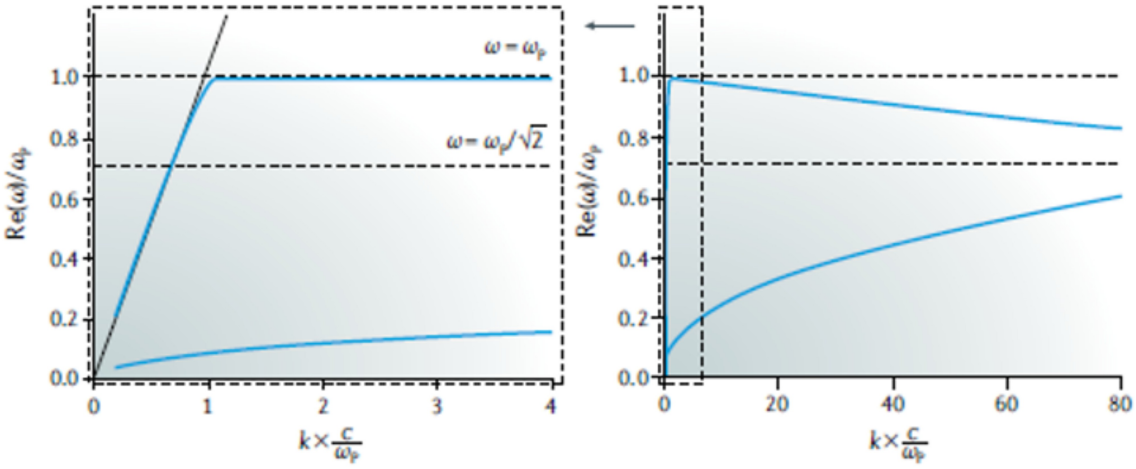

Figure 3.2: Dispersion relations of the ENZ mode, which exists in thin TCO films, and the Berreman mode, which is similar to the surface plasmon mode due to the Drude dispersion (right). The ENZ mode with a nearly flat dispersion (left) appears at $\omega = \omega_p$. Reprinted (adapted) with permission from Ref. 129. Copyright 2019 Springer Nature.

ear processes is the SHG. Benefited from the field enhancement and the wavelength expansion that frees from the phase-matching-condition, a peak in the SHG efficiency is consistently observed in the ENZ region of ITO thin layers, as shown in Fig. 3.3(a).[166] Additionally, phase conjugation (PC) is also allowed in ENZ layers, which implies the time-reversal of the wavefront. The observation of PC and thus a negative refraction in AZO films near its ENZ wavelength is shown in Fig. 3.3(b).[150]

The optical Kerr effect, which indicates the intensity-dependent refractive index, is another widely studied nonlinear effect in ENZ materials. Recent studies have demonstrated the possibility of utilizing transient transmittance (reflectance) spectroscopy to dynamically understand this large nonlinearity.[167, 125, 153, 140, 150] Impressively, a change of refractive index dn in the unity order is observed in the transient experiments conducted on a ITO thin film[168], as revealed in Fig. 3.3(c).[123] Among all possible transient dynamics, two ultrafast processes that normally happen in sub-picosecond scales grab much attention. One is the intraband transition which usually happens with sub-bandgap pump photon energies and another is the inter-

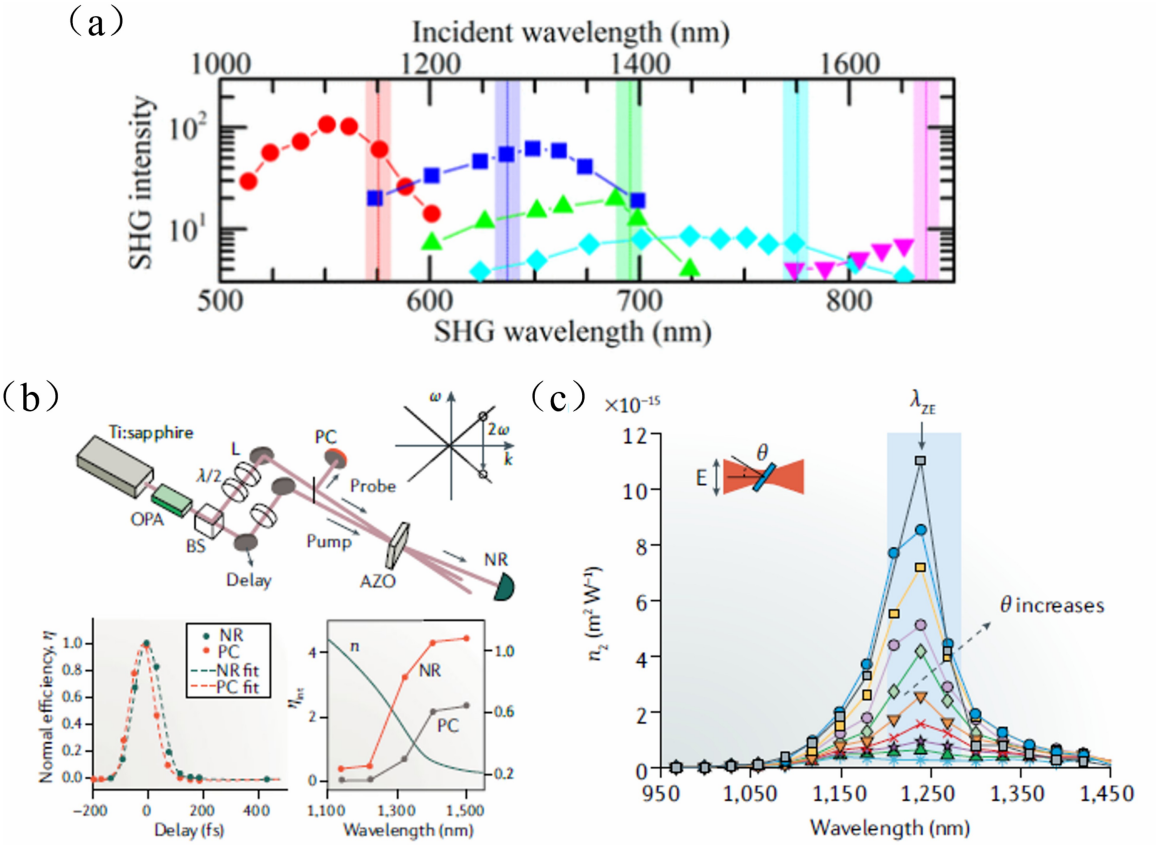

Figure 3.3: Nonlinear optical processes in ENZ materials. (a) SHG from ITO thin layers with various ENZ wavelengths. A peak in the SHG intensity is consistently observed. (b) Observation of phase conjugation (PC) and negative refraction (NR) in an AZO thick film near its ENZ wavelength. A peak in the PC and NR beams occurs in the temporal spectra (bottom left). The efficiency, η, of PC and NR generation coincides with the real index of the film, demonstrating the effect of the ENZ condition (bottom right). (c) Nonlinear refractive index, n_2, of the ITO thin film is enhanced in the ENZ region. Stronger nonlinear response is observed with the increasing incident angle θ. Panel (a) is reprinted (adapted) with permission from Ref. 166. Copyright 2015 Amerian Chemical Society. Panel (b) is reprinted (adapted) with permission from Ref. 31. Copyright 2019 Springer Nature. Panel (c) is reprinted (adapted) with permission from Ref. 129. Copyright 2019 Springer Nature.

band transition pumped with high energy photons such as UV lights. To understand the origin of the nonlinearity observed in these ultrafast experiments necessitates effective modelling of these two processes.[153, 123, 154] For the interband transition, the carrier generation followed by trap-assisted recombination can fully describe the origin of the nonlinearity.[125] For the intraband transition, an optical Kerr effect model proposed in Ref. 140 and Ref. 169, where the plasma frequency ω_p or the refractive index n is linearly dependent on the pump intensity, enables reasonable quantitative description of the nonlinearity. Specifically, the two-temperature model reveals that the rise of the electron temperature due to the laser excitation generates temperature-dependent complex index[123, 153, 125]. This approach uses fitting parameters, such as the electron-phonon coupling strength G determined from the measured time-resolved index change $\Delta n(t)$. Alternatively, a deterministic (fitting parameter free) physical model attributes the nonlinearity to the non-parabolic conduction band structure, which greatly modifies the electron effective mass for the excited hot electron population[170, 152, 171, 161]. However, to our knowledge, no unified approach exists to date and all studies model these mechanisms as separate processes when explaining the origin of the nonlinearity, while their joint contributions and simultaneous interactions remain unexplored. Specifically, for instance, the influence of the non-parabolicity on the interband transition has never been investigated.

3.3 Intraband Transition and Interband Transition Model

An interband transiton model is developed[172] based on the intraband transition model described in Ref. 161. We report a new mechanism where the nonlinearity of ITO thin films is inverted driven by the competition between the intraband and

interband transitions that happen simultaneously under UV excitation. Our theoretical calculation predicts that by varying the non-parobolicity and the Fermi level, the shift of ENZ resonances would occur in opposite spectral directions. This optical switching of ENZ resonances gives rise to transient transmittance signals that follow totally different spectral shapes.

First, the band structure $E(k)$ of ITO thin films is written with the following formula which takes into account the non-parabolicity[173, 174]

$$\frac{k^2\hbar^2}{2m} = E(k) + \frac{E^2}{E_g} \tag{3.5}$$

where m is the effective mass of the conduction band and $1/E_g$ denotes the non-parabolicity. The plasma frequency ω_p is derived from the collisionless Boltzmann equation as[161]

$$\omega_p(\mu,T)^2 = \frac{e^2}{3m\pi^2}\int_0^\infty dE\left(\frac{2m}{\hbar^2}\left(E+\frac{E^2}{E_g}\right)\right)^{\frac{3}{2}}\left(1+\frac{2E}{E_g}\right)^{-1}(-\frac{\partial f_0\left(\mu,T\right)}{\partial E}) \tag{3.6}$$

where μ is the chemical potential, T is the electron temperature and $f_0(\mu,T)$ represents the Fermi-Dirac distribution. For the intraband transition, the free carrier density $n(\mu,T)$ is a constant and the electron energy density $U(\mu,T)$ is equal to the room-temperature energy density $U(\mu,300K)$ plus the absorbed pump photon energy density dU

$$n(\mu,T) = \frac{1}{\pi^2}\int_0^\infty dE\left(\frac{2m}{\hbar^2}\left(E+\frac{E^2}{E_g}\right)\right)^{\frac{1}{2}}\frac{m}{\hbar^2}\left(1+\frac{2E}{E_g}\right)f_0\left(\mu,T\right) \tag{3.7}$$

$$U\left(\mu,300K\right) = \frac{1}{\pi^2}\int_0^\infty dE\left(\frac{2m}{\hbar^2}\left(E+\frac{E^2}{E_g}\right)\right)^{\frac{1}{2}}E\frac{m}{\hbar^2}\left(1+\frac{2E}{E_g}\right)f_0\left(\mu,T\right) \tag{3.8}$$

dU is estimated as the absorbed pump photon energy divided by the total volume of

material illuminated by the pump

$$dU = \frac{FA\cos\theta}{\phi r^2 h} \tag{3.9}$$

where F is the energy per pulse, A is the absorption, θ is the incident angle, r is the pump beam radius and h is the thickness of the film. Therefore, once the band structure parameters m, E_g and the Drude parameters ω_p, γ_p are known, the nonlinearity caused by the intraband transition is fully determined.

For interband transition, however, the free carrier density is no longer a constant. Instead, $n(\mu, T)$ is equal to the room-temperature carrier concentration $n(\mu, 300K)$ plus the density of absorbed photons dn

$$n\left(\mu, 300K\right) + dn = \frac{1}{\pi^2}\int_0^\infty dE \left(\frac{2m}{\hbar^2}\left(E + \frac{E^2}{E_g}\right)\right)^{\frac{1}{2}} \frac{m}{\hbar^2}\left(1 + \frac{2E}{E_g}\right) f_0\left(\mu, T\right) \tag{3.10}$$

dn is given by

$$dn = \frac{FA\cos\theta}{\phi r^2 h E_{photon}} \tag{3.11}$$

where E_{photon} is the pump photon energy.

3.4 Experiments

By utilizing annealing in fabricating ITO thin films with tunable ENZ wavelengths, and adopting a broadband probe beam in transient transmittance spectroscopy, The theoretical predictions are validated by femtosecond (fs) pump-probe measurements, where the spectrally invertible nonlinearity is demonstrated. The non-parabolicity of the band structure, contributing to a larger effective mass in the intraband transition, and the Fermi energy, which determines the free carrier density, are shown to be two competing factors that jointly contribute to the invertible nonlinearity of ITO thin films. Our work reveals the relationship between the large optical nonlinearity and

Table 3.1: Parameters used in sputtering ITO thin films

λ_{ENZ} (nm)	Anneal Temperature (^oC)	Anneal Time (min)
1220	450	60
1400	600	60
1500	300	60

the intrinsic dispersion relationships of the ITO films in the ENZ region, which may guide the development of TCO photonic materials. The ultrafast all-optical active control demonstrated here may be of interested for applications including all-optical modulators, integrated telecom circuits and other nonlinear photonic devices.

3.4.1 Sample Fabrication

The 20 nm thick ITO thin films are deposited by radio-frequency (RF) magnetron sputtering on glass substrates at room temperature. The magnetron sputtering is performed in vacuum at the pressure of 2×10^{-6} Torr, with an Ar gas flow of 12 sccm. It is followed by a post-deposition annealing process in nitrogen atmosphere to red-shift the ENZ wavelengths of ITO films to the NIR regime.[130, 175] The annealing temperatures are shown in Table 3.1. Additional tunability of the ENZ wavelength is achieved by cutting off the nitrogen gas flow during the annealing process, which increases the oxygen concentration in the atmosphere.

3.4.2 Optical Characterization

In the linear optical characterization, the oblique transmittance spectra is measured in an epi-illumination configuration, where the halogen lamp is obliquely incident on the sample at various angles. The transmitted light is collected with a 10x objective (NA=0.25). Transient transmittance experiments are performed by optically pumping the ITO thin films with a single wavelength pulsed laser and probing the transmitted signals with a broadband white light continuum. The pump laser is gen-

erated by guiding a Coherent Astrella Ti:Sapphire laser centered at 800 nm through the optical parametric amplifer (OPA). The pulse length is approximately 150 fs and the repetition frequency is 1kHz. The broadband probe beam is generated from a Ti:Sapphire crystal and the spectral range goes from 800 nm to 1600 nm. The probe beam is obliquely incident at 45 degree and the pump beam is deviated with a small angle. The probe beam is p-polarized to support out-of-plane electric field components and the pump beam is s-polarized to avoid extra nonlinearity caused by two-beam coupling effects.

3.5 Results and Discussion

3.5.1 Linear Characterization Results

Fig. 3.4 shows the linear optical properties of 23nm thick ITO film on a glass cover slip (PGO inc).[172] The oblique-angle transmittance measurements reveal a resonance peak around 1240 nm which corresponds to the ENZ wavelength of ITO. The amplitude of the peak increases with at larger incident angles, while normal incidence does not reveal any ENZ peak. According to Maxwell's boundary condition in Eq. 3.4, given a small permittivity in proximity to the ENZ region, the field normal to the ITO film would be enhanced with larger incident angles producing larger normal components of the field and hence stronger field enhancement. To obtain the permittivity of the ITO thin film, a Drude model is adopted

$$\epsilon(\omega) = \epsilon_r + i\epsilon_i = \epsilon_\infty - \frac{\omega_p^2}{\omega_2 + i\gamma\omega} \tag{3.12}$$

where ϵ_∞ is the background permittivity, γ is the charge carrier collision rate and ω_p is the plasma frequency defined in Eq. 2.20. The transmittance is calculated by transfer matrix method with the fitted Drude parameters ω_p and γ. The transfer

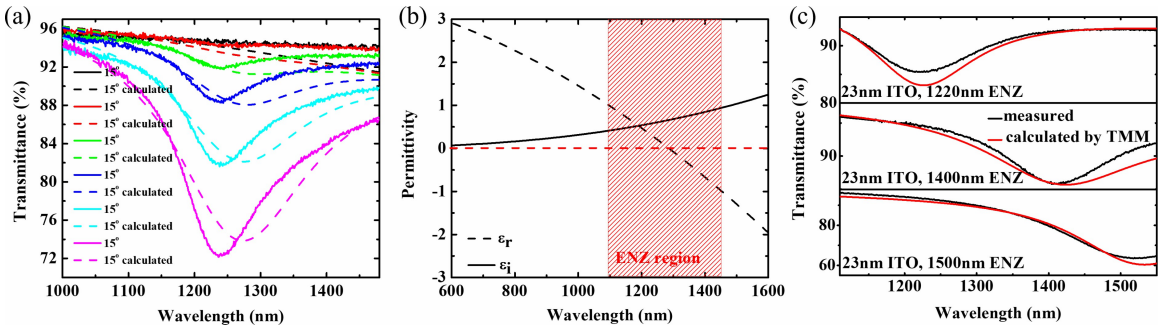

Figure 3.4: (a) Transmittance of the commercial ITO film measured under different incident angles. The dashed curve shows the fitted transmittance spectrum by using the transfer matrix method (TMM) and the Drude model. (b) Calculated permittivity of the commercial ITO film by using the fitted Drude parameters. (c) 60 degree transmittance of sputtered ITO films with different ENZ wavelengths. Black curves are from measurements and red curves are calculated using TMM.

matrix method is based on the continuity of fields on the boundaries. The sample is modelled as a two layer system which is put in the air environment: a glass layer of 1.1 mm with $n = 1.5, k = 0$ and the ITO layer. For each layer, the electric and magnetic field at the end of the layer can be derived from operating a 2×2 matrix on the field at the beginning of the layer, according to Maxwell's equations. Then a stack of layers can then be represented as a system matrix, which is the product of the individual layer matrices. The transmittance of the system can be obtained in terms of the system matrix. We coded TMM in Matlab and the dashed curves in Fig. 3.4(a) show the calculation result using $\omega_p = 1.9eV$ and $\gamma_p = 0.17eV$ which match well with the experiments. The calculated dispersion of ITO with the same Drude parameters is shown in Fig. 3.4(b). The real part of the permittivity switches sign at 1240 nm defining the ENZ region with $\epsilon_i < 1$ (shaded are in Fig. 3.4(b)). To fabricate ITO thin films with different ENZ wavelengths, we use RF sputtering deposition on a glass substrate, followed by an annealing process (see Section 3.4.1 for fabrication details).[130] The measured and fitted transmittance spectra of three samples at 60 degree excitation angle are shown in Fig. 3.4(c). All samples clearly show varying ENZ resonance peaks in the NIR spectral region.

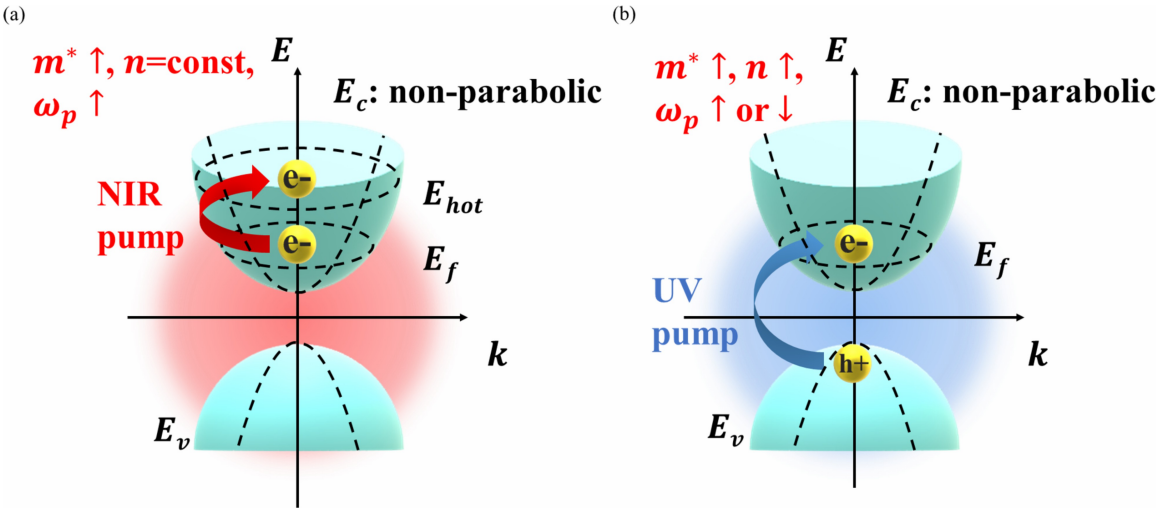

Figure 3.5: Schematic of the nonlinear optical responses in ITO thin films. (a) The intraband transition of conduction band electrons introduces a larger effective mass due to the non-parabolic band structure and decreases the plasma frequency. E_c: conduction band, E_f: Fermi level, E_v: valance band, E_{hot}: hot electron energy level, dashed curves give visual guides for the parabolic band strucutre and the increase of Fermi level. (b) The interband transition generates more free carriers, increases the plasma frequency and meanwhile introduces a larger effective mass . The ultimate nonlinearity depends on the competition between these two mechanisms and can be inverted by controlling the non-parabolicity and the Fermi level.

3.5.2 Nonlinear Characterization Results

Fig. 3.5 shows the schematic of transient optical processes.[172] When the pump photon energy is smaller than the bandgap, the electrons in the conduction band undergo an intraband transition through free carrier absorption, as shown in Fig. 3.5(a). Before the pulse arrives, the electrons are in equilibrium and described by a room temperature Fermi distribution. After absorbing the pump photon, the electrons are excited to higher energy states and forming a hot electron distribution. Due to the nonparabolicity of the conduction band, the effective mass of the electron sea is increased. Accordingly, this decreases the plasma frequency ω_p and therefore a red shifts the ENZ resonance. Since the band gap of ITO films is typically 3.5 eV-4.3 eV[176], this red shift normally happens when the pump wavelength is in the NIR region. On the other hand, as shown in Fig. 3.5(b), when the photon energy is greater

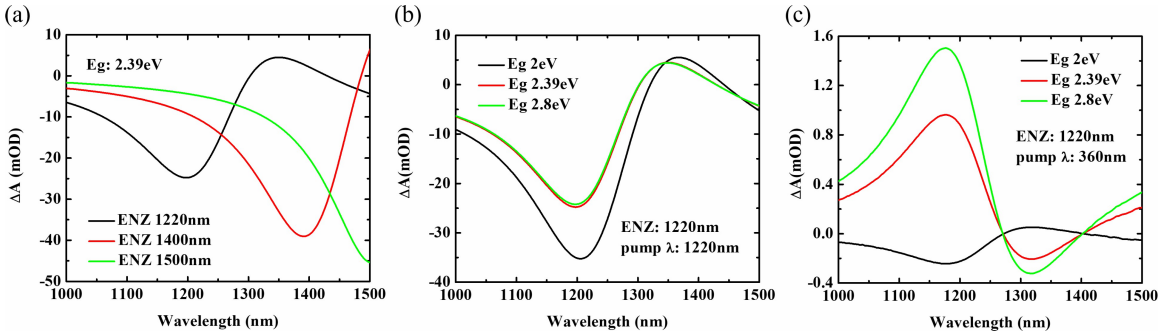

Figure 3.6: (a) Differential transmittance change ΔA with a broadband probe in NIR region calculated using the intraband transition model, where E_g is 2.39 eV. Different colors represent different ENZ wavelengths. (b) Calculated ΔA for different values of E_g. The ENZ wavelength is 1220 nm. (c) Calculated ΔA spectra for various E_g using the interband transition model. The ENZ wavelength is 1220 nm and the pump wavelength is 360 nm.

than the bandgap, interband transition will occur, in which electrons in the valence band are promoted into the conduction band and the free carrier concentration is increased. Consequently, ω_p increases and the ENZ resonance blue shifts accordingly. This normally happens for UV pump for which the photon energy is close or above the band gap. However, with the increase of the free carrier density in the conduction band, the Fermi level is inevitably raised and the effective mass would also increase because of the non-parabolicity. Thus, when the non-parabolicity of the material is large enough so that the effective mass increase is dominant over the free carrier density increase, interband transition can also result in overall red shift of ENZ, inverting the nonlinearity. The total change and the shift direction of the plasma frequency and the nonlinearity will highly depend on the competence between the free carrier density in the equilibrium state (Fermi level) and the non-parabolicity of the conduction band structure.

In Fig. 3.6(a) and Fig. 3.6(b), we theoretically explored the differential transmittance change ΔA near the ENZ region under the NIR pump, where intraband

transition dominates the nonlinearity. ΔA is defined as

$$\Delta A = -log(1 + \Delta T/T_0) \tag{3.13}$$

where T_0 denotes the reference transmittance and ΔT is the dynamic change in transmittance after the pump. In Fig. 3.6(a), the ENZ wavelength is varied from 1220 nm to 1500 nm while the non-parabolicity E_g and the effective mass is kept at 2.39 eV and $0.26m_0$, respectively, where m_0 is the electron mass at rest. Evidently, with a longer ENZ wavelength, which corresponds to a lower free carrier density and a lower Fermi level, the maximum absolute value of ΔA becomes larger. This is because the electrons at a lower Fermi level undergo a larger change of the effective mass when absorbing the same amount of energy resulting in a larger nonlinearity. On the other hand, as shown in Fig. 3.6(b), ΔA becomes smaller with E_g changing from 2 eV to 2.8 eV whereas the ENZ wavelength remains unchanged. Smaller E_g represents larger non-parabolicity as shown in Eq. 3.5, thus introducing a larger modification of the effective mass and a larger nonlinearity.

After individually studying the influence of the free carrier density and the non-parabolicity on the nonlinearity, we predict a novel phenomenon which involves both intraband and interband transitions under a UV pump. The calculated ΔA spectra under the UV pump is plotted in Fig. 3.6(c), where the ENZ wavelength is 1220 nm and E_g is varied from 2 eV to 2.8 eV. Interestingly, unlike in Fig. 3.6(a) and 3.6(b) where the NIR pump gives the same spectral shape of ΔA, the spectral shape under UV excitation in Fig. 3.6(c) highly depends on the relative strength between the free carrier density and the non-parabolicity. If E_g is relatively small (Fig. 3.6(c), black curve) the hot electron-induced Fermi level shift has a stronger contribution than the increase in carrier density due to band-to-band transition and induces an overall red shift of the plasma frequency ω_p. Conversely, an overall blue shift of ω_p occurs when

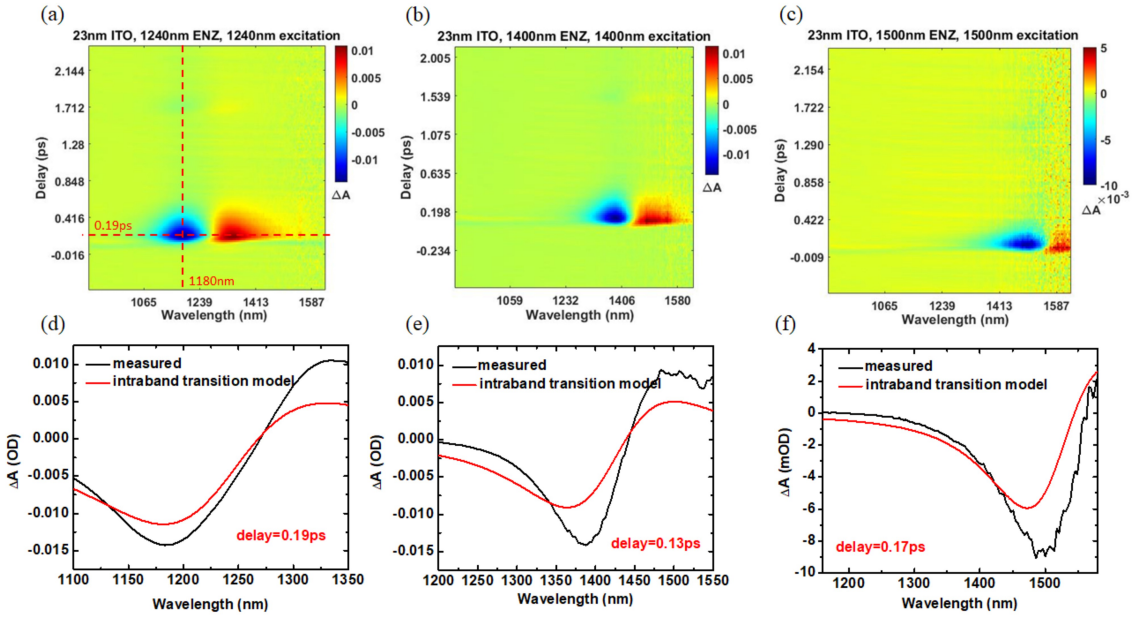

Figure 3.7: (a)(b)(c) Time-resolved transmittance spectra change of ITO films in pump-probe measurements. The pump wavelength coincides with the ENZ wavelength at (a) 1220 nm (b) 1400 nm and (c) 1500 nm. (d)(e)(f) ΔA spectra at the beginning of the recovery process for ENZ wavelength at (d) 1220 nm (e) 1400 nm and (f) 1500 nm. The black curves are extracted from the corresponding two-dimensional maps with the delay time at (d) 0.19 ps (e) 0.13 ps and (f) 0.17 ps. The red curves fit the plasma frequency $omega_p$ after pump. (f) kinetic decay process of the absorbed energy dU. The pump wavelengths are in the NIR region. The scatter curves show experimental data and line curves are exponential fits.

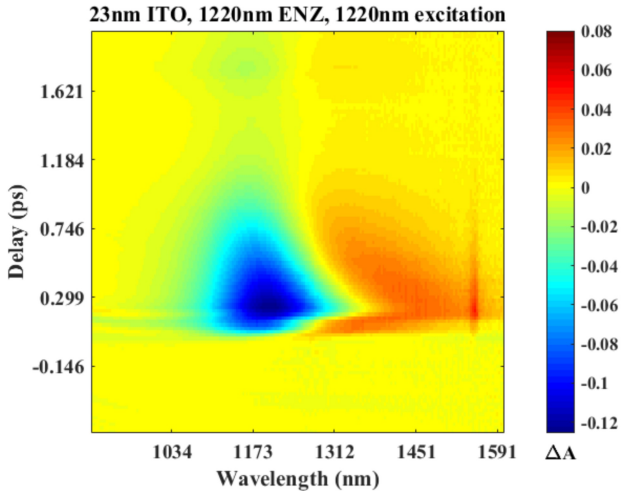

Figure 3.8: Time-resolved transmittance spectra change of the ITO thin film. The pump wavelength coincides with the ENZ wavelength at 1220nm. The maximum $|\Delta A| = 126mOD$ under the $1000\mu J/cm^2$ pump fluence corresponds to $\Delta T/T = 35\%$.

the hot electron contribution is relatively lower (Fig. 3.6(c), red and green curves). To the best of our knowledge, this is the first observation of spectral inversion of the nonlinearity based on the competition between the free carrier density and the non-parabolicity.

Next, we turn our attention to optical pump-probe measurements to elucidate the impact of the Fermi level and the non-parabolicity on the ITO nonlinearity. In a set of transient ultrafast measurements we use a narrowband fs pump laser pulse to induce excitations in ITO films and a broadband fs probe pulse at various delay times to measure the time-resolved transmittance spectra (see Section 3.4.2 for details). Fig. 3.7(a) shows the ΔA spectral map measured on a ITO film with a ENZ resonance at 1220 nm. Choosing a pump wavelength to coincide with the ENZ wavelength optimizes the absorption and enhances the nonlinear response. An ultrafast red-shift of the ENZ resonance is observed, indicating the increase in the electron effective mass induced by intraband transitions. A maximum of nonlinear responce of $\Delta A = 100mOD$ is obtained at a pump fluence of $1000\mu J/cm^2$, as shown in Fig. 3.8, corresponding to $\Delta T/T = 35\%$, which is comparable with values reported

Table 3.2: Drude and band structure parameters of ITO thin films

λ_{ENZ} (nm)	ϵ_∞ (eV)	ω_p (eV)	γ_p (eV)	$m*$ (m_0)	E_g (eV)
1220	3.75	1.95	0.2	0.13	1.77
1400	3.75	1.70	0.14	0.13	2.07
1500	3.75	1.58	0.11	0.43	2.64

in the literature.[125, 153, 161] Additional ΔA spectral maps measured on ITO films with different ENZ wavelengths and pumped at their respective resonance peaks are plotted in Fig. 3.7(b) and Fig. 3.7(c). In Fig. 3.7(d), the spectrum at 0.19 ps from Fig. 3.7(a) is extracted and fitted by the transfer matrix method to get the plasma frequency ω_p, pump immediately after the pump pulse is absorbed. Using the fitted $\omega_{p,pump}$ and unpumped $\omega_{p,unpump}$, the effective mass m and the non-parabolicity E_g can be determined from the intraband transition model. The theoretical spectrum (Fig. 3.7(d), red curve) is in a good agreement with the experimental data. The same calculation is conducted on other samples with ENZ wavelengths at 1400 nm and 1500 nm, as shown in Fig. 3.7(e) and Fig. 3.7(f). All of them match well with the measurements, confirming the validity of our model. The values for all Drude and band structure parameters are listed in Table 3.2. It is demonstrated that with the increase of the plasma frequency, the free carrier density will increase and gives rise to the higher Fermi level. This can be attributed to the sample annealing process where the grain size shrinks and more electrons are relaxed from the bound states.130 The non-parabolicity, generally also tends to increase with the plasma frequency. The reason could be the modification of the crystalline structure followed by the annealing process, however more theoretical and experimental studies are needed to further understand this.

After absorbing the pump photon energy and creating a hot electron distribution, the carriers cool down through the electron-phonon coupling and return to the equilibrium state on a sub-ps time scale.[123, 177] The dissipation of the excitation energy density dU as a function of time, which represents the dynamics of the relax-

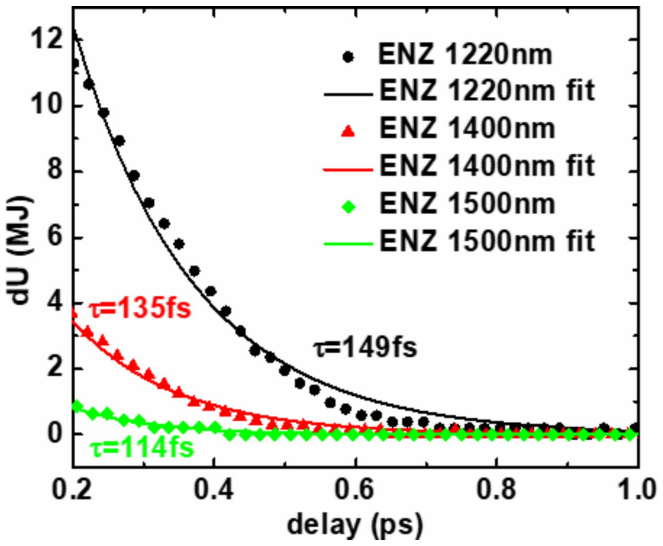

Figure 3.9: kinetic decay process of the absorbed energy dU. The pump wavelengths are in the NIR region. The scatter curves show experimental data and line curves are exponential fits.

ation process, is plotted in Fig. 3.9. The dashed lines are exponential fits to extracted the relaxation times. All of these values are typically around 100 fs scale and agree well with the ultrafast intraband transition dynamics. The increasing discrepancy between the fits and the measurements at shorter delay times can be attributed to the electron temperature dependent heat capacity of electron gas.[123]

Finally, a UV pulse centered at 360 nm is used as the pump source to introduce interband transitions in ITO films. The time-resolved transmittance maps measured on ITO films with various ENZ wavelengths are shown in Fig. 3.10(a)-(c). The photon energy at 360 nm corresponds to the band gap of these ITO films as shown in Fig. 3.11, which shows the pump-wavelength dependent maximum of ΔA. The Burstein-Moss bandgap shift has been shown to be negligible[178, 179], thus it is reasonable a assumption that the same amount of electrons in the valence band are excited to the conduction band in all samples. However, different nonlinear behaviors are clearly observed as the result of the competition between interband and intraband absorption. The ITO film with the ENZ wavelength at 1220 nm possesses the largest non-parabolicity (see Table 3.2), therefore the contribution of intraband transition to

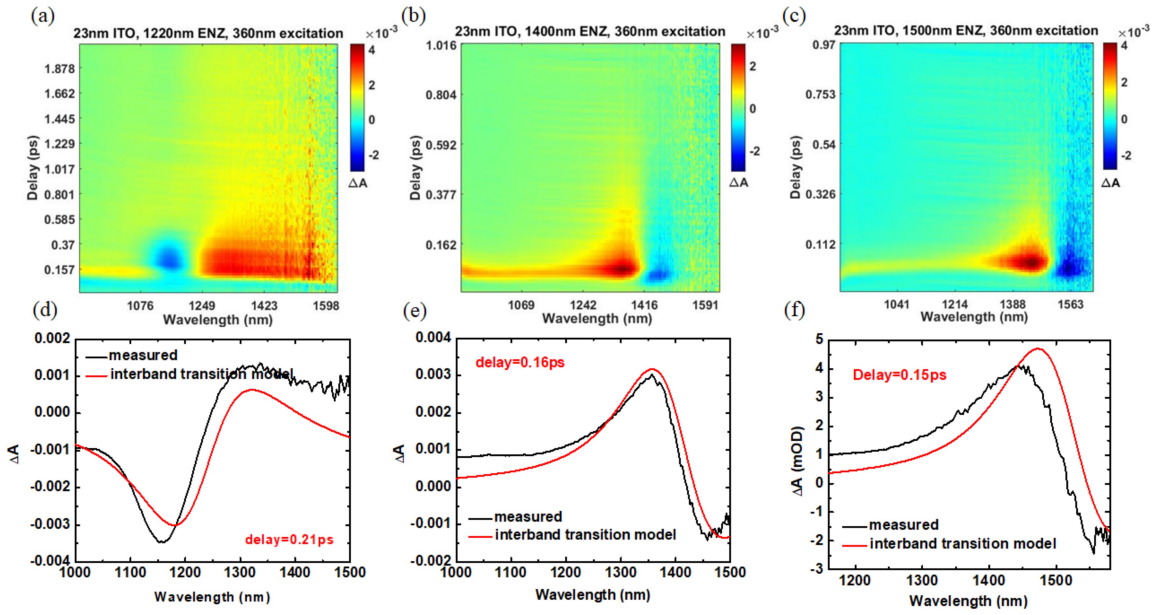

Figure 3.10: (a)(b)(c) Time-resolved transmittance spectra change of ITO films in pump-probe measurements. The pump wavelength is 360 nm. The ENZ wavelength is (a) 1220 nm (b) 1400 nm and (c) 1500 nm. (d)(e)(f) ΔA spectra at the beginning of the recovery process for ENZ wavelength at (d) 1220 nm (e) 1400 nm and (f) 1500 nm. The black curves are extracted from the corresponding two-dimensional maps with the delay time at (d) 0.21 ps (e) 0.16 ps and (f) 0.15ps. The red curves fit the plasma frequency ω_p after pump.

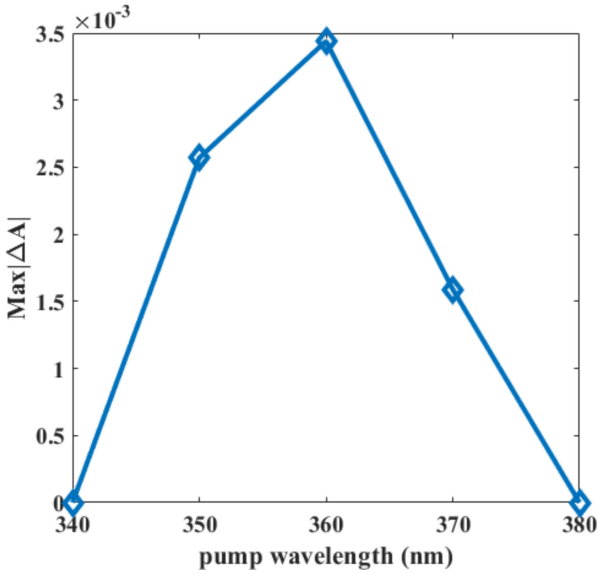

Figure 3.11: Pump wavelength dependent maximum $|\Delta A|$ in the UV region.

the plasma frequency is larger than the contribution of interband transition. Eventually, as shown in Fig. 3.10(a), the plasma frequency is red-shifted which is similar to the behavior under the NIR pump. On the contrary, films with longer ENZ wavelengths have smaller non-parabolicity, which is not able to balance the shift induced by the free carrier density increase induced by interband transitions. Therefore, the plasma frequency is blue-shifted as shown in Fig. 3.10(b) and Fig. 3.10(c). These results agree well with the theoretical calculations shown in Fig. 3.6(c). Moreover, in Fig. 3.10(d),(e) and (f), the experimental spectra corresponding to the peak of ΔA are plotted along with the calculation for $\omega_{p,pump}$. The same parameters in Table 3.2 are adopted to fit the spectra with the interband transition model (Fig. 3.10(d),(e) and (f), red curves). The calculation results agree well with the measurements, indicating the validity of our theoretical predictions.

Finally, the dynamics of the relaxation process is briefly investigated. This process involves thermal dissipation, where the electron temperature decreases through electron-phonon interactions and recombination, including the radiative and the trap-assisted recombination channels.[180] Generally the recombination is slower than the

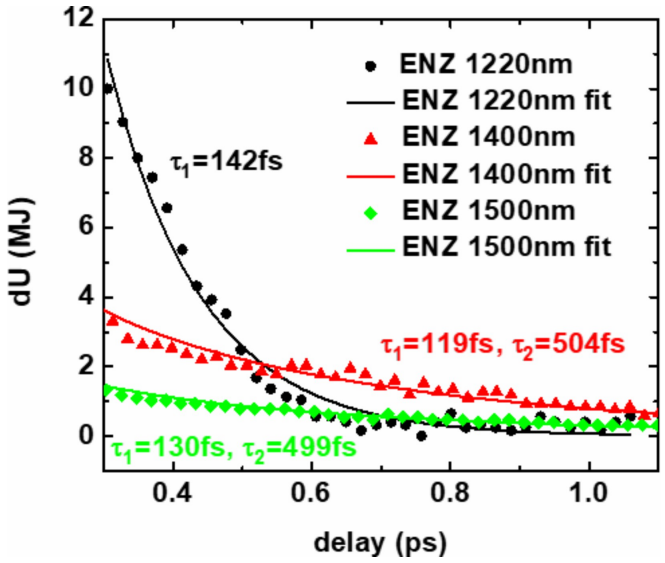

Figure 3.12: (f) kinetic decay process of the absorbed energy dU. The pump wavelength is 360 nm. The scatter curves show experimental data and line curves are exponential fits.

thermal dissipation process. As shown in Fig. 3.12 (black curve), the decay of dU in the ITO film with the ENZ wavelength at 1220 nm shows a characteristic recovery time of 142 fs. This agrees well with the typical thermal dissipation time revealed in Fig. 3.9, indicating the dominance of the intraband transition. On the contrary, red and green curves in Fig. 3.12 include a slower decay process with τ_2 located around 500 fs in addition to the faster decay τ_1 attributed to the thermal dissipation. This longer relaxation rated may correspond to the recombination, which again indicates that interband transitions plays a dominant role in ITO films with the ENZ at 1400 nm and 1500 nm.

3.5.3 More Discussion on Plasmon-ITO Coupling

The coupling between ENZ modes in ITO films and plasmonic modes in gold nanorods is briefly discussed.[153] The schematic of the gold metasurface fabricated on top of an ITO thin film is depicted in Fig. 3.13(a). The dimensions of gold nanorods are determined from the SEM image shown in Fig. 3.13(b). The transmittance spectra

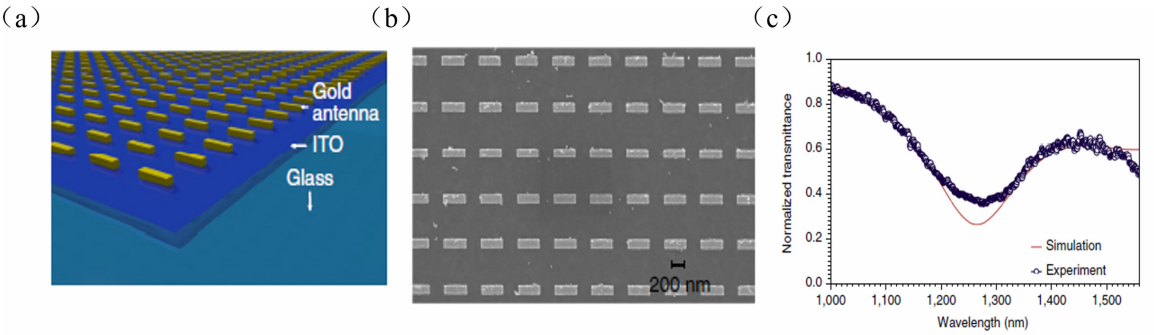

Figure 3.13: (a) the schematic of the sample structure, which consists of gold antenna arrays on top of a thin film of ITO. (b) A SEM image of the fabricated structure. (c) Measured and calculated transmittance spectra of the coupling system. The variation between the experimental result and the FDTD simulation can be attributed to inhomogeneous broadening of the linewidth of the antennas due to fabrication imperfections. Reprinted (adapted) with permission from Ref. 153. Copyright 2018 Springer Nature.

of the coupling system (Fig. 3.13(c)) shows two splitting resonance peaks, indicating the strong coupling between the plasmon and the ENZ mode.

We performed FDTD simulation on the same system and the calculated transmittance spectrum, as shown in Fig. 3.14(a), clearly reveals the splitting peaks. The ITO film is 23 nm and the ENZ region is centered at 1400 nm. Gold nanorods are 250 nm by 100 nm, with the plasmonic mode in resonance with the ENZ mode. Moreover, Fig. 3.13(b) and Fig. 3.13(c) show the field distribution maps at the resonance peaks, where a large enhancement of the electric field is found inside the ITO layer. This enhancement is attributed to both the gold nanorods that confine light at nanoscales, and the ITO film that further brings the amplification of the field according to Maxwell's boundary condition in Eq. 3.4.

The field enhancement can be further enlarged by utilizing the gold nanorods-ITO-gold (MIM) structure, in which the gap mode between top and bottom gold layers is coupled with the ENZ mode. Therefore, the electric field is confined within the volume that defined by the thickness of the ITO film and the dimensions of the gold nanorods. The sample is built by depositing a 30 nm layer of gold with the

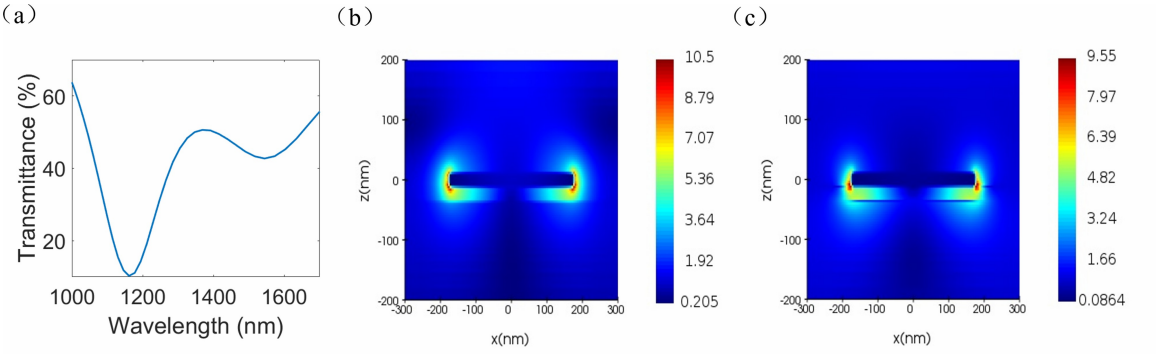

Figure 3.14: (a) The calculated transmittance spectrum of a gold nanorod-ITO strong coupling system. The ITO film is 23 nm and the ENZ region is centered at 1400 nm. Gold nanorods are 250 nm by 100 nm, with the plasmonic mode in resonance with the ENZ mode. (b)(c) Distribution of the electric fields at two resonant peaks at (b) 1159 nm and (c) 1516 nm.

thermal evaporation, followed by sputtering a 23 nm layer of ITO. The arrays of gold nanorods are fabricated by EBL and the thermal evaporation. The period of gold nanorods is 600 nm in the vertical direction and 800 nm in the horizontal direction. Fig. 3.15(a) shows the SEM image of the sample and the transmittance spectra of the MIM structure with various gold nanorods lengths are shown in Fig. 3.15(b). The measurements agree well with the FDTD simulations, as shown in Fig. 3.15(c).

To elucidate the nonlinear effects in these structures, pump-frequency-dependent THG spectra are measured, as shown in Fig. 3.15(d). Nevertheless, as the plasmonic mode frequency approaches the ENZ frequency, the THG intensity decreases. One possible reason of this interesting phenomenon is that near the ENZ frequency, hot spots of the gap mode inside the ITO only generate a singular field enhancement.[124] Due to the near-zero group velocity of the propagating wave in ENZ materials, most of the power of harmonic signals are lost internally without being emitted. The effective mode index tends to decrease despite of the larger singular field enhancement with the smaller detuning.[181] More theoretical works and nonlinear simulations are needed to understand this phenomenon.

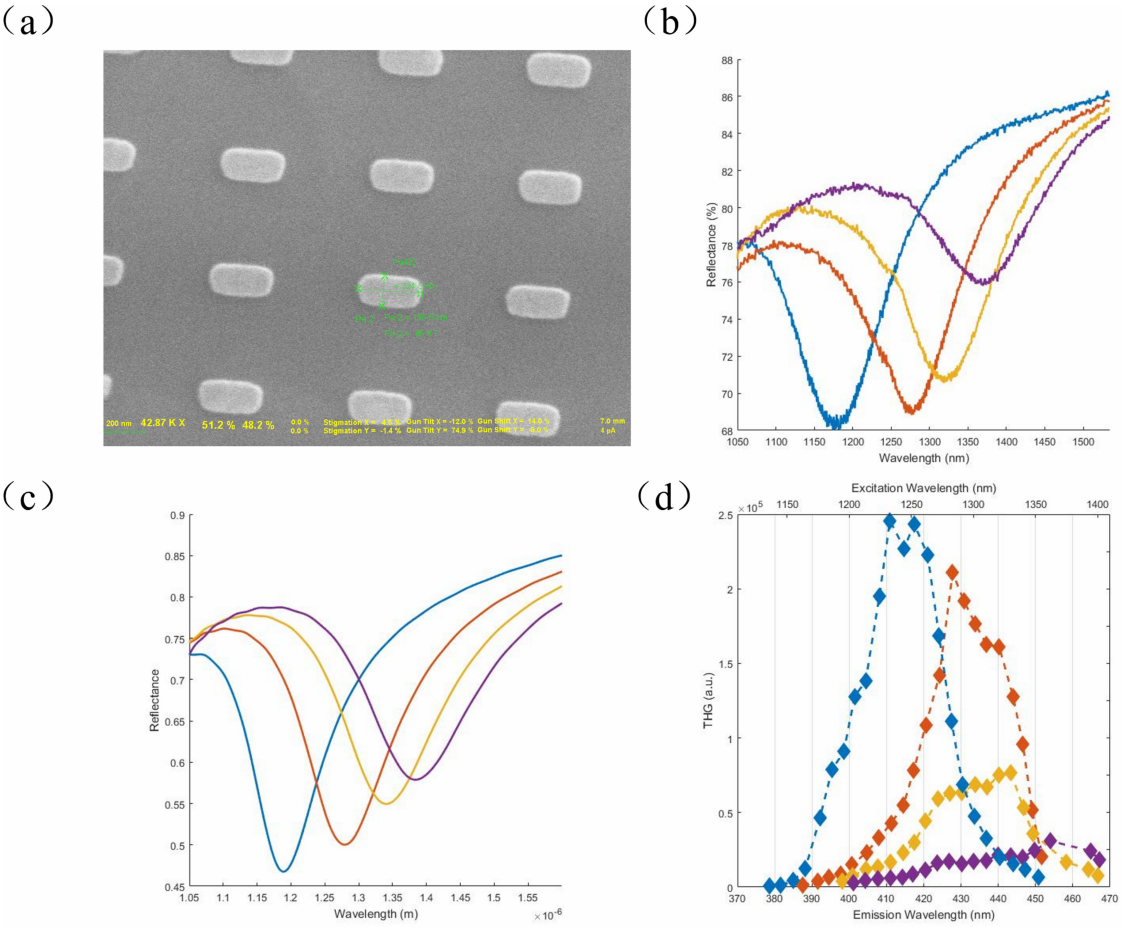

Figure 3.15: (a) A SEM image of the MIM structure. The size of the nanorods is around 350 nm by 150 nm. The period of gold nanorods is 600 nm in the vertical direction and 800 nm in the horizontal direction. (b) Measured transmittance spectra of the MIM structure with various gold nanorods lengths. blue: 250 nm; red: 350 nm; yellow: 450 nm; violet: 550 nm.(c) FDTD simulations of the transmittance spectra of the MIM structure. (d) Pump-wavelength-dependent THG spectra of the MIM structure.

3.6 Conclusions

In conclusion, we demonstrate a comprehensive study of various mechanisms responsible for the ultrafast nonlinear properties of ITO thin films near their ENZ wavelengths. We have explored the interplay between the intraband transition, which increases the electron effective mass due to the non-parabolic band structure, and the interband transition, which generates larger free carrier concentrations. Interestingly, a combination of these two process under the above-bandgap pump results in different nonlinear behaviors depending on the relative contributions between the non-parabolicity and the Fermi level shift. An interband transition model is used to describe this competing mechanism and predict the ultimate shift direction of the plasma frequency. Transient transmittance measurements agree well with the theoretical predictions, demonstrating spectrally invertible nonlinearity. Moreover, the Drude parameters and band structure parameters extracted from the fits show clear trends that are related to the material properties of ITO films. Our findings may guide design and fabrication of TCO photonic platforms based on the tunability of nonlinear optical interactions.

Appendix A

List of Publications

Published works with Emory affiliation:

1. Feng Wang, Manoj Manjare, Robert Lemasters, **Chentao Li**, and Hayk Harutyunyan. "Enhancing second-harmonic generation using dipolar-parity modes in non-planar plasmonic nanocavities." Optics Letters 44 (11), 2787-2790 (2019)

2. **Chentao Li**, Xin Lu, Ajit Srivastava, S. David Storm, Rachel Gelfand, Matthew Pelton, Maxim Sukharev, and Hayk Harutyunyan. "Second harmonic generation from a single plasmonic nanorod strongly coupled to a WSe_2 monolayer." Nano Letters 21.4: 1599-1605. (2020)

3. A. V. Agrawal, Robert Lemasters, **Chentao Li**, Ali Mojibpour, Palash Bharadwaj, Hayk Harutyunyan, and Mukesh Kumar. "Comparison of Enhanced Second Harmonic Generation in Pyramid-like in-plane MoS_2 flakes to Vertically Aligned MoS_2 Flakes" Journal of Applied Physics 129 (6), 063106 (2021)

4. Zhu, Muliang, Sajjad Abdollahramezani, **Chentao Li**, Tianren Fan, Hayk Harutyunyan, and Ali Adibi. "Broadband-Tunable Third-Harmonic Generation Using Phase-Change Chalcogenides." Advanced Photonics Research (under review)

5. Zhu, Muliang, Sajjad Abdollahramezani, **Chentao Li**, Tianren Fan, Hayk Harutyunyan, and Ali Adibi. "Dynamically Tunable Second-Harmonic Generation

Using Hybrid Nanostructures Incorporating Phase-Change Chalcogenides" Nanophotonics (under review)

6. Zhu, Muliang, **Chentao Li**, Tianren Fan, Sajjad Abdollahramezani, Xi Wu, Hayk Harutyunyan, and Ali Adibi. "Quasibound States in the Continuum for Bidirectional Symmetry-Breaking Nonlinear Metasurfaces." CLEO: QELS_Fundamental Science, pp. FTh1M-4 (2021)

7. **Chentao Li**, Xinyu Tian, Guoce Yang, Sukrith U. Dev, Monica S. Allen, Jeffery W. Allen, and Hayk Harutyunyan."Invertible Optical Nonlinearity in Epsilon-near-zero Materials" https://arxiv.org/abs/2203.09600

Bibliography

[1] Gerd Binnig, Heinrich Rohrer, Ch Gerber, and Eddie Weibel. Tunneling through a controllable vacuum gap. *Applied Physics Letters*, 40(2):178–180, 1982.

[2] Winifried Denk, James H Strickler, and Watt W Webb. Two-photon laser scanning fluorescence microscopy. *Science*, 248(4951):73–76, 1990.

[3] Y Barad, Henryk Eisenberg, M Horowitz, and Yaron Silberberg. Nonlinear scanning laser microscopy by third harmonic generation. *Applied Physics Letters*, 70(8):922–924, 1997.

[4] Yasushi Inouye and Satoshi Kawata. Near-field scanning optical microscope with a metallic probe tip. *Optics letters*, 19(3):159–161, 1994.

[5] Amanda J Haes and Richard P Van Duyne. A nanoscale optical biosensor: sensitivity and selectivity of an approach based on the localized surface plasmon resonance spectroscopy of triangular silver nanoparticles. *Journal of the American Chemical Society*, 124(35):10596–10604, 2002.

[6] T.L. Koch and U. Koren. Semiconductor photonic integrated circuits. *IEEE Journal of Quantum Electronics*, 27(3):641–653, 1991.

[7] Lukas Novotny and Bert Hecht. *Principles of nano-optics*. Cambridge university press, 2012.

[8] Motoichi Ohtsu, Kiyoshi Kobayashi, Tadashi Kawazoe, Takashi Yatsui, and Makoto Naruse. *Principles of nanophotonics*. CRC Press, 2008.

[9] Xavier Michalet, Fabien F Pinaud, Laurent A Bentolila, James M Tsay, SJJL Doose, Jack J Li, G Sundaresan, AM Wu, SS Gambhir, and S Weiss. Quantum dots for live cells, in vivo imaging, and diagnostics. *science*, 307(5709):538–544, 2005.

[10] DL Huffaker, G Park, Z Zou, OB Shchekin, and DG Deppe. 1.3 μm room-temperature gaas-based quantum-dot laser. *Applied Physics Letters*, 73(18):2564–2566, 1998.

[11] JJ Mock, M Barbic, DR Smith, DA Schultz, and Sh Schultz. Shape effects in plasmon resonance of individual colloidal silver nanoparticles. *The Journal of Chemical Physics*, 116(15):6755–6759, 2002.

[12] Hongya Geng, Simon Vilms Pedersen, Yun Ma, Tabasom Haghighi, Hongliang Dai, Philip D Howes, and Molly M Stevens. Noble metal nanoparticle biosensors: From fundamental studies toward point-of-care diagnostics. *Accounts of Chemical Research*, pages 467–474, 2022.

[13] Karolina Niska, Ewelina Zielinska, Marek Witold Radomski, and Iwona Inkielewicz-Stepniak. Metal nanoparticles in dermatology and cosmetology: Interactions with human skin cells. *Chemico-biological interactions*, 295:38–51, 2018.

[14] Jinu Mathew, Josny Joy, and Soney C George. Potential applications of nanotechnology in transportation: A review. *Journal of King Saud University-Science*, 31(4):586–594, 2019.

[15] Steven G Johnson. Photonic crystals: Periodic surprises in electromagnetism. *Lecture 3: Fabrication technologies for 3d photonic crystals*, 2005.

[16] Surendra B Anantharaman, Christopher E Stevens, Jason Lynch, Baokun Song, Jin Hou, Huiqin Zhang, Kiyoung Jo, Pawan Kumar, Jean-Christophe Blancon, Aditya D Mohite, et al. Self-hybridized polaritonic emission from layered perovskites. *Nano Letters*, 21(14):6245–6252, 2021.

[17] Yuanmu Yang, Wenyi Wang, Abdelaziz Boulesbaa, Ivan I Kravchenko, Dayrl P Briggs, Alexander Puretzky, David Geohegan, and Jason Valentine. Nonlinear fano-resonant dielectric metasurfaces. *Nano letters*, 15(11):7388–7393, 2015.

[18] Wisconsin Centers for Nanoscale Technology. Electron beam lithography, 2020.

[19] Bo Cui. Microfabrication and thin film technology, 2016.

[20] J.D. Plummer, M.D. Deal, and P.B. Griffin. *Silicon VLSI Technology: Fundamentals, Practice and Modeling*. Prentice Hall electronics and VLSI series. Prentice Hall, 2000.

[21] Wikipedia contributors. Etching (microfabrication), 2021.

[22] Rick Trebino. Nonlinear optics course, 2012.

[23] Robert W Boyd. *Nonlinear optics*. Academic press, 2020.

[24] PD Maker, RW Terhune, M Nisenoff, and CM Savage. Effects of dispersion and focusing on the production of optical harmonics. *Physical review letters*, 8(1):21, 1962.

[25] Jeremy Butet, Pierre-Francois Brevet, and Olivier JF Martin. Optical second harmonic generation in plasmonic nanostructures: from fundamental principles to advanced applications. *ACS nano*, 9(11):10545–10562, 2015.

[26] Nicolae C Panoiu, Wei EI Sha, DY Lei, and GC Li. Nonlinear optics in plasmonic nanostructures. *Journal of Optics*, 20(8):083001, 2018.

[27] John Kerr LL.D. Xl. a new relation between electricity and light: Dielectrified media birefringent. *The London, Edinburgh, and Dublin Philosophical Magazine and Journal of Science*, 50(332):337–348, 1875.

[28] P. L. Kelley. Self-focusing of optical beams. *Phys. Rev. Lett.*, 15:1005–1008, Dec 1965.

[29] Boris Ya Zel'Dovich, Nikolai F Pilipetsky, and Vladimir Vasilevich Shkunov. *Principles of phase conjugation*, volume 42. Springer, 2013.

[30] Yaron Silberberg and I Bar Joseph. Instabilities, self-oscillation, and chaos in a simple nonlinear optical interaction. *Physical Review Letters*, 48(22):1541, 1982.

[31] Nathaniel Kinsey, Clayton DeVault, Alexandra Boltasseva, and Vladimir M. Shalaev. Near-zero-index materials for photonics. *Nature Reviews Materials*, 4(12):742–760, 2019.

[32] Pierre Agostini and Louis F DiMauro. The physics of attosecond light pulses. *Reports on progress in physics*, 67(6):813, 2004.

[33] Donna Strickland and Gerard Mourou. Compression of amplified chirped optical pulses. *Optics communications*, 55(6):447–449, 1985.

[34] Rick Trebino. Ultrafast optics course, 2012.

[35] David E Spence, P Np Kean, and Wilson Sibbett. 60-fsec pulse generation from a self-mode-locked ti: sapphire laser. *Optics letters*, 16(1):42–44, 1991.

[36] Matthew Pelton. Modified spontaneous emission in nanophotonic structures. *Nature Photonics*, 9(7):427–435, 2015.

[37] Eugen Merzbacher. *Quantum mechanics*. Jones & Bartlett Publishers, 1961.

[38] Edward M Purcell, Henry Cutler Torrey, and Robert V Pound. Resonance absorption by nuclear magnetic moments in a solid. *Physical review*, 69(1-2):37, 1946.

[39] Martin Moskovits. Surface-enhanced spectroscopy. *Reviews of modern physics*, 57(3):783, 1985.

[40] Shinpei Ogawa, Masahiro Imada, Susumu Yoshimoto, Makoto Okano, and Susumu Noda. Control of light emission by 3d photonic crystals. *Science*, 305(5681):227–229, 2004.

[41] Pai Peng, Yong-Chun Liu, Da Xu, Qi-Tao Cao, Guowei Lu, Qihuang Gong, Yun-Feng Xiao, et al. Enhancing coherent light-matter interactions through microcavity-engineered plasmonic resonances. *Physical review letters*, 119(23):233901, 2017.

[42] Burak Gurlek, Vahid Sandoghdar, and Diego Martín-Cano. Manipulation of quenching in nanoantenna–emitter systems enabled by external detuned cavities: a path to enhance strong-coupling. *ACS Photonics*, 5(2):456–461, 2018.

[43] Maxim Sukharev and Abraham Nitzan. Optics of exciton-plasmon nanomaterials. *Journal of Physics: Condensed Matter*, 29(44):443003, 2017.

[44] JJ Sanchez-Mondragon, NB Narozhny, and JH Eberly. Theory of spontaneous-emission line shape in an ideal cavity. *Physical review letters*, 51(7):550, 1983.

[45] Galina Khitrova, HM Gibbs, M Kira, Stephan W Koch, and Axel Scherer. Vacuum rabi splitting in semiconductors. *Nature physics*, 2(2):81–90, 2006.

[46] Denis G Baranov, Martin Wersall, Jorge Cuadra, Tomasz J Antosiewicz, and Timur Shegai. Novel nanostructures and materials for strong light–matter interactions. *Acs Photonics*, 5(1):24–42, 2018.

[47] Edwin T Jaynes and Frederick W Cummings. Comparison of quantum and semiclassical radiation theories with application to the beam maser. *Proceedings of the IEEE*, 51(1):89–109, 1963.

[48] Marlan O Scully and M Suhail Zubairy. Quantum optics, 1999.

[49] Thomas Hümmer, FJ García-Vidal, Luis Martín-Moreno, and David Zueco. Weak and strong coupling regimes in plasmonic qed. *Physical Review B*, 87(11):115419, 2013.

[50] Salvatore Savasta, Rosalba Saija, Alessandro Ridolfo, Omar Di Stefano, Paolo Denti, and Ferdinando Borghese. Nanopolaritons: vacuum rabi splitting with a single quantum dot in the center of a dimer nanoantenna. *ACS nano*, 4(11):6369–6376, 2010.

[51] Päivi Törmä and William L Barnes. Strong coupling between surface plasmon polaritons and emitters: a review. *Reports on Progress in Physics*, 78(1):013901, 2014.

[52] Matthew Pelton, S David Storm, and Haixu Leng. Strong coupling of emitters to single plasmonic nanoparticles: exciton-induced transparency and rabi splitting. *Nanoscale*, 11(31):14540–14552, 2019.

[53] Michael Tavis and Frederick W. Cummings. Exact solution for an n-molecule—radiation-field hamiltonian. *Phys. Rev.*, 170:379–384, Jun 1968.

[54] P Vasa, W Wang, R Pomraenke, Margherita Maiuri, Cristian Manzoni, G Cerullo, and C Lienau. Optical stark effects in j-aggregate–metal hybrid nanostructures exhibiting a strong exciton–surface-plasmon-polariton interaction. *Physical review letters*, 114(3):036802, 2015.

[55] S Christopoulos, G Baldassarri Höger Von Högersthal, AJD Grundy, PG Lagoudakis, AV Kavokin, JJ Baumberg, G Christmann, R Butté, E Feltin, J-F Carlin, et al. Room-temperature polariton lasing in semiconductor microcavities. *Physical review letters*, 98(12):126405, 2007.

[56] Hui Deng, Gregor Weihs, Charles Santori, Jacqueline Bloch, and Yoshihisa Yamamoto. Condensation of semiconductor microcavity exciton polaritons. *Science*, 298(5591):199–202, 2002.

[57] Felipe Herrera and Frank C Spano. Cavity-controlled chemistry in molecular ensembles. *Physical Review Letters*, 116(23):238301, 2016.

[58] Anoop Thomas, Lucas Lethuillier-Karl, Kalaivanan Nagarajan, Robrecht MA Vergauwe, Jino George, Thibault Chervy, Atef Shalabney, Eloïse Devaux, Cyriaque Genet, Joseph Moran, et al. Tilting a ground-state reactivity landscape by vibrational strong coupling. *Science*, 363(6427):615–619, 2019.

[59] Juan De Torres, Mathieu Mivelle, Satish Babu Moparthi, Herve Rigneault, Niek F Van Hulst, Maria F Garcia-Parajo, Emmanuel Margeat, and Jerome Wenger. Plasmonic nanoantennas enable forbidden forster dipole–dipole energy transfer and enhance the fret efficiency. *Nano letters*, 16(10):6222–6230, 2016.

[60] Guillermo Muñoz-Matutano, Andrew Wood, Mattias Johnsson, Xavier Vidal, Ben Q Baragiola, Andreas Reinhard, Aristide Lemaitre, Jacqueline Bloch, Alberto Amo, Gilles Nogues, et al. Emergence of quantum correlations from interacting fibre-cavity polaritons. *Nature Materials*, 18(3):213–218, 2019.

[61] Li Bing Tan, Ovidiu Cotlet, Andrea Bergschneider, Richard Schmidt, Patrick Back, Yuya Shimazaki, Martin Kroner, and Ataç İmamoğlu. Interacting polaron-polaritons. *Physical Review X*, 10(2):021011, 2020.

[62] Anton Frisk Kockum, Adam Miranowicz, Simone De Liberato, Salvatore Savasta, and Franco Nori. Ultrastrong coupling between light and matter. *Nature Reviews Physics*, 1(1):19–40, 2019.

[63] Dirk Englund, Arka Majumdar, Michal Bajcsy, Andrei Faraon, Pierre Petroff, and Jelena Vučković. Ultrafast photon-photon interaction in a strongly coupled quantum dot-cavity system. *Physical review letters*, 108(9):093604, 2012.

[64] Thomas Volz, Andreas Reinhard, Martin Winger, Antonio Badolato, Kevin J Hennessy, Evelyn L Hu, and Ataç Imamoğlu. Ultrafast all-optical switching by single photons. *Nature Photonics*, 6(9):605–609, 2012.

[65] Peter Lodahl, Sahand Mahmoodian, and Søren Stobbe. Interfacing single photons and single quantum dots with photonic nanostructures. *Reviews of Modern Physics*, 87(2):347, 2015.

[66] Shuo Sun, Hyochul Kim, Glenn S Solomon, and Edo Waks. A quantum phase switch between a single solid-state spin and a photon. *Nature nanotechnology*, 11(6):539–544, 2016.

[67] Shuo Sun, Hyochul Kim, Zhouchen Luo, Glenn S Solomon, and Edo Waks. A single-photon switch and transistor enabled by a solid-state quantum memory. *Science*, 361(6397):57–60, 2018.

[68] Mario Miscuglio, Armin Mehrabian, Zibo Hu, Shaimaa I Azzam, Jonathan George, Alexander V Kildishev, Matthew Pelton, and Volker J Sorger. All-optical nonlinear activation function for photonic neural networks. *Optical Materials Express*, 8(12):3851–3863, 2018.

[69] RJ Thompson, Gerhard Rempe, and HJ Kimble. Observation of normal-mode splitting for an atom in an optical cavity. *Physical review letters*, 68(8):1132, 1992.

[70] Thibault Chervy, Jialiang Xu, Yulong Duan, Chunliang Wang, Loïc Mager, Maurice Frerejean, Joris AW Munninghoff, Paul Tinnemans, James A Hutchison, Cyriaque Genet, et al. High-efficiency second-harmonic generation from hybrid light-matter states. *Nano letters*, 16(12):7352–7356, 2016.

[71] Tomoyuki Yoshie, Axel Scherer, J Hendrickson, Galina Khitrova, HM Gibbs, G Rupper, C Ell, OB Shchekin, and DG Deppe. Vacuum rabi splitting with a single quantum dot in a photonic crystal nanocavity. *Nature*, 432(7014):200–203, 2004.

[72] Emmanuelle Peter, Pascale Senellart, David Martrou, Aristide Lemaître, J Hours, JM Gérard, and Jacqueline Bloch. Exciton-photon strong-coupling regime for a single quantum dot embedded in a microcavity. *Physical review letters*, 95(6):067401, 2005.

[73] J Pelal Reithmaier, G Sek, A Loffler, C Hofmann, S Kuhn, S Reitzenstein, LV Keldysh, VD Kulakovskii, TL Reinecke, and A Forchel. Strong coupling in a single quantum dot–semiconductor microcavity system. *Nature*, 432(7014):197–200, 2004.

[74] Marie-Elena Kleemann, Rohit Chikkaraddy, Evgeny M Alexeev, Dean Kos, Cloudy Carnegie, Will Deacon, Alex Casalis De Pury, Christoph Große, Bart De Nijs, Jan Mertens, et al. Strong-coupling of wse2 in ultra-compact plasmonic nanocavities at room temperature. *Nature communications*, 8(1):1–7, 2017.

[75] Johannes Kern, Andreas Trugler, Iris Niehues, Johannes Ewering, Robert Schmidt, Robert Schneider, Sina Najmaei, Antony George, Jing Zhang, Jun Lou, et al. Nanoantenna-enhanced light–matter interaction in atomically thin ws2. *Acs Photonics*, 2(9):1260–1265, 2015.

[76] Gülis Zengin, Martin Wersäll, Sara Nilsson, Tomasz J Antosiewicz, Mikael Käll,

and Timur Shegai. Realizing strong light-matter interactions between single-nanoparticle plasmons and molecular excitons at ambient conditions. *Physical review letters*, 114(15):157401, 2015.

[77] Martin Wersall, Jorge Cuadra, Tomasz J Antosiewicz, Sinan Balci, and Timur Shegai. Observation of mode splitting in photoluminescence of individual plasmonic nanoparticles strongly coupled to molecular excitons. *Nano letters*, 17(1):551–558, 2017.

[78] Gary P Wiederrecht, Gregory A Wurtz, and Jasmina Hranisavljevic. Coherent coupling of molecular excitons to electronic polarizations of noble metal nanoparticles. *Nano Letters*, 4(11):2121–2125, 2004.

[79] Andrea E Schlather, Nicolas Large, Alexander S Urban, Peter Nordlander, and Naomi J Halas. Near-field mediated plexcitonic coupling and giant rabi splitting in individual metallic dimers. *Nano letters*, 13(7):3281–3286, 2013.

[80] Eva-Maria Roller, Christos Argyropoulos, Alexander Hogele, Tim Liedl, and Mauricio Pilo-Pais. Plasmon–exciton coupling using dna templates. *Nano letters*, 16(9):5962–5966, 2016.

[81] Renming Liu, Zhang-Kai Zhou, Yi-Cong Yu, Tengwei Zhang, Hao Wang, Guanghui Liu, Yuming Wei, Huanjun Chen, and Xue-Hua Wang. Strong light-matter interactions in single open plasmonic nanocavities at the quantum optics limit. *Physical review letters*, 118(23):237401, 2017.

[82] Jinxiu Wen, Hao Wang, Weiliang Wang, Zexiang Deng, Chao Zhuang, Yu Zhang, Fei Liu, Juncong She, Jun Chen, Huanjun Chen, et al. Room-temperature strong light–matter interaction with active control in single plasmonic nanorod coupled with two-dimensional atomic crystals. *Nano letters*, 17(8):4689–4697, 2017.

[83] Bowen Li, Shuai Zu, Jiadong Zhou, Qiao Jiang, Bowen Du, Hangyong Shan, Yang Luo, Zheng Liu, Xing Zhu, and Zheyu Fang. Single-nanoparticle plasmonic electro-optic modulator based on mos2 monolayers. *ACS nano*, 11(10):9720–9727, 2017.

[84] Michael Stuhrenberg, Battulga Munkhbat, Denis G Baranov, Jorge Cuadra, Andrew B Yankovich, Tomasz J Antosiewicz, Eva Olsson, and Timur Shegai. Strong light–matter coupling between plasmons in individual gold bi-pyramids and excitons in mono-and multilayer wse2. *Nano letters*, 18(9):5938–5945, 2018.

[85] Jiawei Sun, Huatian Hu, Di Zheng, Daxiao Zhang, Qian Deng, Shunping Zhang, and Hongxing Xu. Light-emitting plexciton: exploiting plasmon–exciton interaction in the intermediate coupling regime. *ACS nano*, 12(10):10393–10402, 2018.

[86] Mingsong Wang, Alex Krasnok, Tianyi Zhang, Leonardo Scarabelli, He Liu, Zilong Wu, Luis M Liz-Marzán, Mauricio Terrones, Andrea Alù, and Yuebing Zheng. Tunable fano resonance and plasmon–exciton coupling in single au nanotriangles on monolayer ws2 at room temperature. *Advanced Materials*, 30(22):1705779, 2018.

[87] Di Zheng, Shunping Zhang, Qian Deng, Meng Kang, Peter Nordlander, and Hongxing Xu. Manipulating coherent plasmon–exciton interaction in a single silver nanorod on monolayer wse2. *Nano letters*, 17(6):3809–3814, 2017.

[88] Xiaoze Liu, Tal Galfsky, Zheng Sun, Fengnian Xia, Erh-chen Lin, Yi-Hsien Lee, Stéphane Kéna-Cohen, and Vinod M Menon. Strong light–matter coupling in two-dimensional atomic crystals. *Nature Photonics*, 9(1):30–34, 2015.

[89] Parinda Vasa, Robert Pomraenke, S Schwieger, Yu I Mazur, Vas Kunets, P Srinivasan, E Johnson, JE Kihm, DS Kim, E Runge, et al. Coherent

exciton–surface-plasmon-polariton interaction in hybrid metal-semiconductor nanostructures. *Physical review letters*, 101(11):116801, 2008.

[90] J Bellessa, C Bonnand, JC Plenet, and J Mugnier. Strong coupling between surface plasmons and excitons in an organic semiconductor. *Physical review letters*, 93(3):036404, 2004.

[91] TK Hakala, JJ Toppari, Anton Kuzyk, M Pettersson, H Tikkanen, H Kunttu, and Päivi Törmä. Vacuum rabi splitting and strong-coupling dynamics for surface-plasmon polaritons and rhodamine 6g molecules. *Physical Review Letters*, 103(5):053602, 2009.

[92] A González-Tudela, PA Huidobro, Luis Martín-Moreno, C Tejedor, and FJ García-Vidal. Theory of strong coupling between quantum emitters and propagating surface plasmons. *Physical review letters*, 110(12):126801, 2013.

[93] Chentao Li, Xin Lu, Ajit Srivastava, S David Storm, Rachel Gelfand, Matthew Pelton, Maxim Sukharev, and Hayk Harutyunyan. Second harmonic generation from a single plasmonic nanorod strongly coupled to a wse2 monolayer. *Nano Letters*, 21(4):1599–1605, 2020.

[94] Daiying Zhang, Liqiu Men, and Qiying Chen. Microfabrication and applications of opto-microfluidic sensors. *Sensors*, 11(5):5360–5382, 2011.

[95] Nourdine Zibouche, Agnieszka Kuc, Janice Musfeldt, and Thomas Heine. Transition-metal dichalcogenides for spintronic applications. *Annalen der Physik*, 526(9-10):395–401, 2014.

[96] Kin Fai Mak, Keliang He, Changgu Lee, Gwan Hyoung Lee, James Hone, Tony F Heinz, and Jie Shan. Tightly bound trions in monolayer mos2. *Nature materials*, 12(3):207–211, 2013.

[97] Jacob B Khurgin. Two-dimensional exciton–polariton—light guiding by transition metal dichalcogenide monolayers. *Optica*, 2(8):740–742, 2015.

[98] Johannes Schmutzler, Marc Aßmann, Thomas Czerniuk, Martin Kamp, Christian Schneider, Sven Höfling, and Manfred Bayer. Nonlinear spectroscopy of exciton-polaritons in a gaas-based microcavity. *Physical Review B*, 90(7):075103, 2014.

[99] ACS Pimenta, LC Faria, JC González, M de Giorgi, Daniele Sanvitto, and FM Matinaga. Nonlinear optical effects with polariton lasers in a gaas microcavity. *The Journal of Physical Chemistry C*, 122(30):17501–17506, 2018.

[100] Fábio Barachati, Janos Simon, Yulia A Getmanenko, Stephen Barlow, Seth R Marder, and Stéphane Kéna-Cohen. Tunable third-harmonic generation from polaritons in the ultrastrong coupling regime. *Acs Photonics*, 5(1):119–125, 2018.

[101] Xiaobo Han, Kai Wang, Patrick D Persaud, Xiangyuan Xing, Weiwei Liu, Hua Long, Fang Li, Bing Wang, Mahi R Singh, and Peixiang Lu. Harmonic resonance enhanced second-harmonic generation in the monolayer ws2–ag nanocavity. *Acs Photonics*, 7(3):562–568, 2020.

[102] S Rudin and TL Reinecke. Oscillator model for vacuum rabi splitting in microcavities. *Physical Review B*, 59(15):10227, 1999.

[103] Xiaohua Wu, Stephen K Gray, and Matthew Pelton. Quantum-dot-induced transparency in a nanoscale plasmonic resonator. *Optics express*, 18(23):23633–23645, 2010.

[104] Elena Drobnyh, Ruth Pachter, and Maxim Sukharev. Harmonic generation by metal nanostructures optically coupled to two-dimensional transition-metal dichalcogenide. *The Journal of Physical Chemistry C*, 123(11):6898–6904, 2019.

[105] Zhuo Wang, Zhaogang Dong, Hai Zhu, Lei Jin, Ming-Hui Chiu, Lain-Jong Li, Qing-Hua Xu, Goki Eda, Stefan A Maier, Andrew TS Wee, et al. Selectively plasmon-enhanced second-harmonic generation from monolayer tungsten diselenide on flexible substrates. *ACS nano*, 12(2):1859–1867, 2018.

[106] Jeremy Butet, Julien Duboisset, Guillaume Bachelier, Isabelle Russier-Antoine, Emmanuel Benichou, Christian Jonin, and Pierre-François Brevet. Optical second harmonic generation of single metallic nanoparticles embedded in a homogeneous medium. *Nano letters*, 10(5):1717–1721, 2010.

[107] A Slablab, L Le Xuan, M Zielinski, Y De Wilde, V Jacques, D Chauvat, and J-F Roch. Second-harmonic generation from coupled plasmon modes in a single dimer of gold nanospheres. *Optics express*, 20(1):220–227, 2012.

[108] Michael Scalora, Maria Antonietta Vincenti, Domenico de Ceglia, Vito Roppo, Marco Centini, Neset Akozbek, and MJ Bloemer. Second-and third-harmonic generation in metal-based structures. *Physical Review A*, 82(4):043828, 2010.

[109] Elena Drobnyh and Maxim Sukharev. Plasmon enhanced second harmonic generation by periodic arrays of triangular nanoholes coupled to quantum emitters. *The Journal of Chemical Physics*, 152(9):094706, 2020.

[110] J Ribeiro-Soares, C Janisch, Z Liu, AL Elías, MS Dresselhaus, M Terrones, LG Cançado, and A Jorio. Second harmonic generation in wse2. *2D Materials*, 2(4):045015, 2015.

[111] Charles Varin, Rhys Emms, Graeme Bart, Thomas Fennel, and Thomas Brabec. Explicit formulation of second and third order optical nonlinearity in the fdtd framework. *Computer physics communications*, 222:70–83, 2018.

[112] Andrea Splendiani, Liang Sun, Yuanbo Zhang, Tianshu Li, Jonghwan Kim,

Chi-Yung Chim, Giulia Galli, and Feng Wang. Emerging photoluminescence in monolayer mos2. *Nano letters*, 10(4):1271–1275, 2010.

[113] Kin Fai Mak, Changgu Lee, James Hone, Jie Shan, and Tony F Heinz. Atomically thin mos 2: a new direct-gap semiconductor. *Physical review letters*, 105(13):136805, 2010.

[114] Seong-Yeon Lee, Tae-Young Jeong, Ji-Hee Kim, Seokjoon Yun, and Ki-Ju Yee. Self-consistent dielectric constant determination for monolayer wse 2. *Optics express*, 26(18):23061–23068, 2018.

[115] Pierre Fauché, Christian Gebhardt, Maxim Sukharev, and Renaud AL Vallée. Plasmonic opals: observation of a collective molecular exciton mode beyond the strong coupling. *Scientific reports*, 7(1):1–9, 2017.

[116] Adi Salomon, Robert J Gordon, Yehiam Prior, Tamar Seideman, and Maxim Sukharev. Strong coupling between molecular excited states and surface plasmon modes of a slit array in a thin metal film. *Physical review letters*, 109(7):073002, 2012.

[117] Tomasz J Antosiewicz, S Peter Apell, and Timur Shegai. Plasmon–exciton interactions in a core–shell geometry: from enhanced absorption to strong coupling. *Acs Photonics*, 1(5):454–463, 2014.

[118] Jeremy Butet, Gabriel D Bernasconi, Marlene Petit, Alexandre Bouhelier, Chen Yan, Olivier JF Martin, Benoit Cluzel, and Olivier Demichel. Revealing a mode interplay that controls second-harmonic radiation in gold nanoantennas. *Acs Photonics*, 4(11):2923–2929, 2017.

[119] Inigo Liberal and Nader Engheta. Near-zero refractive index photonics. *Nature Photonics*, 11(3):149–158, 2017.

[120] Yang Li, Shota Kita, Philip Muñoz, Orad Reshef, Daryl I Vulis, Mei Yin, Marko Lončar, and Eric Mazur. On-chip zero-index metamaterials. *Nature Photonics*, 9(11):738–742, 2015.

[121] Ernst Jan R Vesseur, Toon Coenen, Humeyra Caglayan, Nader Engheta, and Albert Polman. Experimental verification of n= 0 structures for visible light. *Physical review letters*, 110(1):013902, 2013.

[122] Orad Reshef, Philip Camayd-Muñoz, Daryl I Vulis, Yang Li, Marko Loncar, and Eric Mazur. Direct observation of phase-free propagation in a silicon waveguide. *ACS Photonics*, 4(10):2385–2389, 2017.

[123] M. Zahirul Alam, Israel De Leon, and Robert W. Boyd. Large optical nonlinearity of indium tin oxide in its epsilon-near-zero region. *Science*, 352(6287):795–797, 2016.

[124] M. H. Javani and M. I. Stockman. Real and imaginary properties of epsilon-near-zero materials. *Phys Rev Lett*, 117(10):107404, 2016.

[125] M. Clerici, N. Kinsey, C. DeVault, J. Kim, E. G. Carnemolla, L. Caspani, A. Shaltout, D. Faccio, V. Shalaev, A. Boltasseva, and M. Ferrera. Controlling hybrid nonlinearities in transparent conducting oxides via two-colour excitation. *Nat Commun*, 8:15829, 2017.

[126] DC Adams, Sandeep Inampudi, T Ribaudo, D Slocum, S Vangala, NA Kuhta, WD Goodhue, Viktor A Podolskiy, and D Wasserman. Funneling light through a subwavelength aperture with epsilon-near-zero materials. *Physical review letters*, 107(13):133901, 2011.

[127] Salvatore Campione, Joel R. Wendt, Gordon A. Keeler, and Ting S. Luk. Near-infrared strong coupling between metamaterials and epsilon-near-zero modes in

degenerately doped semiconductor nanolayers. *ACS Photonics*, 3(2):293–297, 2016.

[128] Richard W Ziolkowski and Ehud Heyman. Wave propagation in media having negative permittivity and permeability. *Physical review E*, 64(5):056625, 2001.

[129] Orad Reshef, Israel De Leon, M. Zahirul Alam, and Robert W. Boyd. Nonlinear optical effects in epsilon-near-zero media. *Nature Reviews Materials*, 4(8):535–551, 2019.

[130] Yu Wang, Antonio Capretti, and Luca Dal Negro. Wide tuning of the optical and structural properties of alternative plasmonic materials. *Optical Materials Express*, 5(11), 2015.

[131] Gururaj V Naik, Vladimir M Shalaev, and Alexandra Boltasseva. Alternative plasmonic materials: beyond gold and silver. *Advanced Materials*, 25(24):3264–3294, 2013.

[132] N. Kinsey, C. DeVault, J. Kim, M. Ferrera, V. M. Shalaev, and A. Boltasseva. Epsilon-near-zero al-doped zno for ultrafast switching at telecom wavelengths. *Optica*, 2(7), 2015.

[133] Joshua D Caldwell, Orest J Glembocki, Yan Francescato, Nicholas Sharac, Vincenzo Giannini, Francisco J Bezares, James P Long, Jeffrey C Owrutsky, Igor Vurgaftman, Joseph G Tischler, et al. Low-loss, extreme subdiffraction photon confinement via silicon carbide localized surface phonon polariton resonators. *Nano letters*, 13(8):3690–3697, 2013.

[134] W Streyer, K Feng, Y Zhong, AJ Hoffman, and D Wasserman. Engineering the reststrahlen band with hybrid plasmon/phonon excitations. *MRS Communications*, 6(1):1–8, 2016.

[135] Ruben Maas, James Parsons, Nader Engheta, and Albert Polman. Experimental realization of an epsilon-near-zero metamaterial at visible wavelengths. *Nature Photonics*, 7(11):907–912, 2013.

[136] Maxim R Shcherbakov, Polina P Vabishchevich, Alexander S Shorokhov, Katie E Chong, Duk-Yong Choi, Isabelle Staude, Andrey E Miroshnichenko, Dragomir N Neshev, Andrey A Fedyanin, and Yuri S Kivshar. Ultrafast all-optical switching with magnetic resonances in nonlinear dielectric nanostructures. *Nano letters*, 15(10):6985–6990, 2015.

[137] Xueqin Huang, Yun Lai, Zhi Hong Hang, Huihuo Zheng, and CT Chan. Dirac cones induced by accidental degeneracy in photonic crystals and zero-refractive-index materials. *Nature materials*, 10(8):582–586, 2011.

[138] Ting S Luk, Domenico De Ceglia, Sheng Liu, Gordon A Keeler, Rohit P Prasankumar, Maria A Vincenti, Michael Scalora, Michael B Sinclair, and Salvatore Campione. Enhanced third harmonic generation from the epsilon-near-zero modes of ultrathin films. *Applied Physics Letters*, 106(15):151103, 2015.

[139] Antonio Capretti, Yu Wang, Nader Engheta, and Luca Dal Negro. Enhanced third-harmonic generation in si-compatible epsilon-near-zero indium tin oxide nanolayers. *Optics letters*, 40(7):1500–1503, 2015.

[140] L. Caspani, R. P. Kaipurath, M. Clerici, M. Ferrera, T. Roger, J. Kim, N. Kinsey, M. Pietrzyk, A. Di Falco, V. M. Shalaev, A. Boltasseva, and D. Faccio. Enhanced nonlinear refractive index in epsilon-near-zero materials. *Phys Rev Lett*, 116(23):233901, 2016.

[141] Ward D Newman, Cristian L Cortes, Jon Atkinson, Sandipan Pramanik, Ray-

mond G DeCorby, and Zubin Jacob. Ferrell–berreman modes in plasmonic epsilon-near-zero media. *Acs Photonics*, 2(1):2–7, 2015.

[142] Igor I Smolyaninov, Vera N Smolyaninova, Alexander V Kildishev, and Vladimir M Shalaev. Anisotropic metamaterials emulated by tapered waveguides: application to optical cloaking. *Physical review letters*, 102(21):213901, 2009.

[143] Vera N Smolyaninova, Igor I Smolyaninov, Alexander V Kildishev, and Vladimir M Shalaev. Experimental observation of the trapped rainbow. *Applied Physics Letters*, 96(21):211121, 2010.

[144] Ting S Luk, Salvatore Campione, Iltai Kim, Simin Feng, Young Chul Jun, Sheng Liu, Jeremy B Wright, Igal Brener, Peter B Catrysse, Shanhui Fan, et al. Directional perfect absorption using deep subwavelength low-permittivity films. *Physical Review B*, 90(8):085411, 2014.

[145] Alexander I Lvovsky, Barry C Sanders, and Wolfgang Tittel. Optical quantum memory. *Nature photonics*, 3(12):706–714, 2009.

[146] Nadia Mattiucci, Mark J Bloemer, and Giuseppe D'Aguanno. Phase-matched second harmonic generation at the dirac point of a 2-d photonic crystal. *Optics Express*, 22(6):6381–6390, 2014.

[147] Jongbum Kim, Aveek Dutta, Gururaj V. Naik, Alexander J. Giles, Francisco J. Bezares, Chase T. Ellis, Joseph G. Tischler, Ahmed M. Mahmoud, Humeyra Caglayan, Orest J. Glembocki, Alexander V. Kildishev, Joshua D. Caldwell, Alexandra Boltasseva, and Nader Engheta. Role of epsilon-near-zero substrates in the optical response of plasmonic antennas. *Optica*, 3(3), 2016.

[148] Prasad P Iyer, Mihir Pendharkar, Chris J Palmstrøm, and Jon A Schuller.

Ultrawide thermal free-carrier tuning of dielectric antennas coupled to epsilon-near-zero substrates. *Nature communications*, 8(1):1–7, 2017.

[149] Isak C Reines, Michael G Wood, Ting S Luk, Darwin K Serkland, and Salvatore Campione. Compact epsilon-near-zero silicon photonic phase modulators. *Optics Express*, 26(17):21594–21605, 2018.

[150] S. Vezzoli, V. Bruno, C. DeVault, T. Roger, V. M. Shalaev, A. Boltasseva, M. Ferrera, M. Clerici, A. Dubietis, and D. Faccio. Optical time reversal from time-dependent epsilon-near-zero media. *Phys Rev Lett*, 120(4):043902, 2018.

[151] Soham Saha, Benjamin T. Diroll, Joshua Shank, Zhaxylyk Kudyshev, Aveek Dutta, Sarah Nahar Chowdhury, Ting Shan Luk, Salvatore Campione, Richard D. Schaller, Vladimir M. Shalaev, Alexandra Boltasseva, and Michael G. Wood. Broadband, high-speed, and large-amplitude dynamic optical switching with yttrium-doped cadmium oxide. *Advanced Functional Materials*, 30(7), 2019.

[152] Yuanmu Yang, Kyle Kelley, Edward Sachet, Salvatore Campione, Ting S. Luk, Jon-Paul Maria, Michael B. Sinclair, and Igal Brener. Femtosecond optical polarization switching using a cadmium oxide-based perfect absorber. *Nature Photonics*, 11(6):390–395, 2017.

[153] M. Zahirul Alam, Sebastian A. Schulz, Jeremy Upham, Israel De Leon, and Robert W. Boyd. Large optical nonlinearity of nanoantennas coupled to an epsilon-near-zero material. *Nature Photonics*, 12(2):79–83, 2018.

[154] V. Bruno, C. DeVault, S. Vezzoli, Z. Kudyshev, T. Huq, S. Mignuzzi, A. Jacassi, S. Saha, Y. D. Shah, S. A. Maier, D. R. S. Cumming, A. Boltasseva, M. Ferrera, M. Clerici, D. Faccio, R. Sapienza, and V. M. Shalaev. Negative refraction

in time-varying strongly coupled plasmonic-antenna-epsilon-near-zero systems. *Phys Rev Lett*, 124(4):043902, 2020.

[155] Viktoriia E Babicheva, Nathaniel Kinsey, Gururaj V Naik, Marcello Ferrera, Andrei V Lavrinenko, Vladimir M Shalaev, and Alexandra Boltasseva. Towards cmos-compatible nanophotonics: Ultra-compact modulators using alternative plasmonic materials. *Optics express*, 21(22):27326–27337, 2013.

[156] Viktoriia E Babicheva, Alexandra Boltasseva, and Andrei V Lavrinenko. Transparent conducting oxides for electro-optical plasmonic modulators. *Nanophotonics*, 4(2):165–185, 2015.

[157] Inigo Liberal and Nader Engheta. The rise of near-zero-index technologies. *Science*, 358(6370):1540–1541, 2017.

[158] PB Johnson and RW Christy. Optical constants of transition metals: Ti, v, cr, mn, fe, co, ni, and pd. *Physical review B*, 9(12):5056, 1974.

[159] T. Tyborski, S. Kalusniak, S. Sadofev, F. Henneberger, M. Woerner, and T. Elsaesser. Ultrafast nonlinear response of bulk plasmons in highly doped zno layers. *Phys Rev Lett*, 115(14):147401, 2015.

[160] P. Guo, R. D. Schaller, L. E. Ocola, B. T. Diroll, J. B. Ketterson, and R. P. Chang. Large optical nonlinearity of ito nanorods for sub-picosecond all-optical modulation of the full-visible spectrum. *Nat Commun*, 7:12892, 2016.

[161] Peijun Guo, Richard D. Schaller, John B. Ketterson, and Robert P. H. Chang. Ultrafast switching of tunable infrared plasmons in indium tin oxide nanorod arrays with large absolute amplitude. *Nature Photonics*, 10(4):267–273, 2016.

[162] Joshua R. Hendrickson, Shivashankar Vangala, Chandriker Dass, Ricky Gibson, John Goldsmith, Kevin Leedy, Dennis E. Walker, Justin W. Cleary, Wonkyu

Kim, and Junpeng Guo. Coupling of epsilon-near-zero mode to gap plasmon mode for flat-top wideband perfect light absorption. *ACS Photonics*, 5(3):776–781, 2018.

[163] Chandriker Kavir Dass, Hoyeong Kwon, Shivashankar Vangala, Evan M. Smith, Justin W. Cleary, Junpeng Guo, Andrea Alù, and Joshua R. Hendrickson. Gap-plasmon-enhanced second-harmonic generation in epsilon-near-zero nanolayers. *ACS Photonics*, 7(1):174–179, 2019.

[164] Bilge Can Yildiz and Humeyra Caglayan. Epsilon-near-zero media coupled with localized surface plasmon modes. *Physical Review B*, 102(16), 2020.

[165] Simon Vassant, Jean-Paul Hugonin, Francois Marquier, and Jean-Jacques Greffet. Berreman mode and epsilon near zero mode. *Optics express*, 20(21):23971–23977, 2012.

[166] Antonio Capretti, Yu Wang, Nader Engheta, and Luca Dal Negro. Comparative study of second-harmonic generation from epsilon-near-zero indium tin oxide and titanium nitride nanolayers excited in the near-infrared spectral range. *Acs Photonics*, 2(11):1584–1591, 2015.

[167] Y. Zhou, M. Z. Alam, M. Karimi, J. Upham, O. Reshef, C. Liu, A. E. Willner, and R. W. Boyd. Broadband frequency translation through time refraction in an epsilon-near-zero material. *Nat Commun*, 11(1):2180, 2020.

[168] E. Feigenbaum, K. Diest, and H. A. Atwater. Unity-order index change in transparent conducting oxides at visible frequencies. *Nano Lett*, 10(6):2111–6, 2010.

[169] J. Bohn, T. S. Luk, C. Tollerton, S. W. Hutchings, I. Brener, S. Horsley, W. L. Barnes, and E. Hendry. All-optical switching of an epsilon-near-zero plasmon resonance in indium tin oxide. *Nat Commun*, 12(1):1017, 2021.

[170] Ray Secondo, Jacob Khurgin, and Nathaniel Kinsey. Absorptive loss and band non-parabolicity as a physical origin of large nonlinearity in epsilon-near-zero materials. *Optical Materials Express*, 10(7), 2020.

[171] Xiaoge Liu, Junghyun Park, Ju-Hyung Kang, Hongtao Yuan, Yi Cui, Harold Y. Hwang, and Mark L. Brongersma. Quantification and impact of nonparabolicity of the conduction band of indium tin oxide on its plasmonic properties. *Applied Physics Letters*, 105(18), 2014.

[172] Chentao Li, Xinyu Tian, Guoce Yang, Sukrith U. Dev, Monica S. Allen, Jeffery W. Allen, and Hayk Harutyunyan. Invertible optical nonlinearity in epsilon-near-zero materials. *https://arxiv.org/abs/2203.09600*, 2022.

[173] Evan O Kane. Band structure of indium antimonide. *Journal of Physics and Chemistry of Solids*, 1(4):249–261, 1957.

[174] Morrel H Cohen. Energy bands in the bismuth structure. i. a nonellipsoidal model for electrons in bi. *Physical Review*, 121(2):387, 1961.

[175] Yu Wang, Adam C Overvig, Sajan Shrestha, Ran Zhang, Ren Wang, Nanfang Yu, and Luca Dal Negro. Tunability of indium tin oxide materials for mid-infrared plasmonics applications. *Optical Materials Express*, 7(8):2727–2739, 2017.

[176] Ze Yu, Ishanie R Perera, Torben Daeneke, Satoshi Makuta, Yasuhiro Tachibana, Jacek J Jasieniak, Amaresh Mishra, Peter Bäuerle, Leone Spiccia, and Udo Bach. Indium tin oxide as a semiconductor material in efficient p-type dye-sensitized solar cells. *NPG Asia Materials*, 8(9):e305–e305, 2016.

[177] N Del Fatti, C Voisin, M Achermann, S Tzortzakis, D Christofilos, and F Vallée. Nonequilibrium electron dynamics in noble metals. *Physical Review B*, 61(24):16956, 2000.

[178] Elias Burstein. Anomalous optical absorption limit in insb. *Physical review*, 93(3):632, 1954.

[179] Li-jian Meng and MP Dos Santos. Properties of indium tin oxide films prepared by rf reactive magnetron sputtering at different substrate temperature. *Thin solid films*, 322(1-2):56–62, 1998.

[180] Simon M Sze, Yiming Li, and Kwok K Ng. *Physics of semiconductor devices*. John wiley & sons, 2021.

[181] Clayton T. DeVault, Vladimir A. Zenin, Anders Pors, Krishnakali Chaudhuri, Jongbum Kim, Alexandra Boltasseva, Vladimir M. Shalaev, and Sergey I. Bozhevolnyi. Suppression of near-field coupling in plasmonic antennas on epsilon-near-zero substrates. *Optica*, 5(12), 2018.